GEOSTROPHIC OCEAN CURRENTS,
FRESHWATER FLUXES,
HYDROGRAPHY, AND SALINITY FIELD
IN NARES STRAIT
BETWEEN THE CANADIAN ARCTIC ARCHIPELAGO
AND NW GREENLAND
DATE: 06/10/2010

by

Berit Rabe

A dissertation submitted to the Faculty of the University of Delaware in partial fulfillment of the requirements for the degree of Doctor of Philosophy in Marine Studies

Summer 2010

GEOSTROPHIC OCEAN CURRENTS,

FRESHWATER FLUXES,

HYDROGRAPHY, AND SALINITY FIELD

IN NARES STRAIT

BETWEEN THE CANADIAN ARCTIC ARCHIPELAGO

AND NW GREENLAND

DATE: 06/10/2010

by

Berit Rabe

Approved: _____
Charles E. Epifanio, Ph.D.
Director of the School of Marine Science and Policy

Approved: _____
Nancy Targett, Ph.D.
Dean of the College of Earth, Ocean, and Environment

Approved: _____
Debra Hess Norris, M.S.
Vice Provost for Graduate and Professional Education

I certify that I have read this dissertation and that in my opinion it meets the academic and professional standard required by the University as a dissertation for the degree of Doctor of Philosophy.

Signed: _____

Andreas Münchow, Ph.D.
Professor in charge of dissertation

I certify that I have read this dissertation and that in my opinion it meets the academic and professional standard required by the University as a dissertation for the degree of Doctor of Philosophy.

Signed: _____

Pablo Huq, Ph.D.
Member of dissertation committee

I certify that I have read this dissertation and that in my opinion it meets the academic and professional standard required by the University as a dissertation for the degree of Doctor of Philosophy.

Signed: _____

Kelly Falkner, Ph.D.
Member of dissertation committee

I certify that I have read this dissertation and that in my opinion it meets the academic and professional standard required by the University as a dissertation for the degree of Doctor of Philosophy.

Signed: _____

Roger Samelson, Ph.D.
Member of dissertation committee

ACKNOWLEDGEMENTS

This work would not have been possible without the help and support of all the following people.

I wish to thank my Ph.D. advisor Dr. Andreas Münchow for his guidance, enthusiasm, and leading my research in the right direction. I also thank my whole committee including Dr. Kelly Falkner, Dr. Roger Samelson and Dr. Pablo Huq for helpful input, suggestions, and sharing their knowledge and time. Richard Garvine also added comments early on during my studies and was dearly missed after his passing.

A big thanks goes to Helen Johnson for creative input, being there as a friend, listener, and mentor. Humfrey Melling added detailed knowledge, good spirits, and lots of comments, that were always appreciated.

Thanks to all my friends in Robinson Hall and Weniger Hall who are still here or have moved on over the years (Ana, Felipe, Lauren, Phil, Joseph, Pat, Entin, Neil, Chris, Zack, James, Gaurav, Rob, Melissa, Brian, JT, Jen, Hua).

Thanks also goes to all the supporting staff in Robinson Hall on all floors, in Lewes, and in Corvallis who made the logistics of my studies possible.

Technicians at sea, the crew of USCGC Healy and CCGS Larsen made this whole project possible and I am grateful for that. The good times during working hours, Luaus, or Iron Man competitions on the Larsen will always be remembered.

My mentoring network of supportive women has been invaluable during the last years and their encouragement and understanding were essential in my development as a scientist.

Of course I also thank all my friends in Newark for all their support, friendship, distractions, and encouragements. Especially Gina and Solveig were more than support and friends as we were at the same stages in our dissertations.

Thanks also to my friends at home in and around Hamburg, in Oregon, or anywhere else in the world for being there for me.

My parents, family, and host family were always supportive of my endeavors and without them I wouldn't be here.

A big thank you goes to Robin for being there for me all this time, believing in me, listening to me, and sharing life with me during grad school and beyond.

This work is dedicated to family and friends who are always there for me.

TABLE OF CONTENTS

LIST OF FIGURES

xvi

LIST OF TABLES

ABSTRACT

This dissertation focuses on ocean currents, geostrophic volume and freshwater fluxes, hydrography, and salinity fields in Nares Strait, one of the major straits in the Canadian Arctic Archipelago (CAA) to the NW of Greenland. Nares Strait connects the Arctic to the North Atlantic Ocean, facilitating an exchange of freshwater between both oceans. The freshwater budget of the Arctic Ocean plays an important role in the global climate system. Observations of freshwater flux through the CAA have been sparse, seasonally biased, and on short time scales in the past. Between 2003 and 2006 oceanographic instruments deployed near 80.5°N measured conductivity, temperature, pressure, and velocity at high temporal and spatial resolution across the 38 km wide and 400 m deep Nares Strait.

The focus of my research is on the analysis of the novel CT data set in combination with local wind, along-channel pressure gradients, and ADCP data. Two different methodologies were developed to evaluate data from the innovative CT moorings that avoid ice and continuously sample the water column due to the mooring motion at tidal time scales. Nares Strait is ice-covered throughout the year with ice drifting in late summer, fall, and early winter, and ice being land-fast the remainder of the year.

Geostrophic volume and freshwater fluxes vary between the two ice states showing more variability during mobile ice conditions. Geostrophic freshwater flux (three-year mean of 20 ± 3 mSv, Sv $= 10^6$ m^3 s^{-1}, no trend observed) is modulated by the ice cover and reveals 30% higher fluxes during mobile ice conditions than during land-fast ice conditions. A 25% increase occurs when extrapolating to the

surface to account for freshwater in the unsampled surface layer. Enhanced freshwater fluxes during mobile ice conditions can have implications in the future when ice conditions change towards a more ice-free state due to no ice bridge forming in Smith Sound. The geostrophic volume flux (three-year mean of 0.47 ± 0.05 Sv) increases over the three-year period by $15 \pm 4\%$. The limited domain for fluxes is 58% of the total area above 200 m, including a level of known motion at 200 m.

Forcing of the geostrophic freshwater flux through Nares Strait is a combination between local wind and along-channel pressure gradient forcing during mobile ice conditions. During land-fast ice conditions only the along-channel pressure gradient is forcing the geostrophic freshwater flux due to the decoupling from the atmosphere through the ice cover.

The three-year mean geostrophic velocity has a surface-intensified southward flow against the western side of the strait and a secondary core flowing southward in the middle of the strait. Distinguishing between the two different ice states, I find the surface-intensified core of up to 0.28 m s^{-1} in the middle of the strait during mobile ice conditions. A sub-surface core of about 0.25 m s^{-1} exists on the western side of the strait during land-fast ice conditions, intensifying over the three-year study period.

When comparing geostrophic velocity to ADCP velocity a large discrepancy exists during all seasons within five km of the western coast. This discrepancy I associate with the lateral boundary layer; the CT measurements are close enough to the coast to be within the horizontal boundary layer. Geostrophic velocity resembles free-slip conditions; ADCP velocity resembles no-slip conditions. In the eastern part of the strait velocities compare well.

Different water masses occupy the strait with fresh, cold water in the top layers on the western side and warm, salty water of Atlantic origin at depth on the eastern side of the strait. Salinity variations of about two psu in time and space

reflect a variable freshwater outflow from the Arctic Ocean. One particularly strong pulse occurred at the end of July 2005. For several days, steeply sloping isohalines indicated strong geostrophic flow down the middle of the strait coinciding with an amplified ice export from the Arctic due to strong southward winds.

Chapter 1

INTRODUCTION

1.1 Motivation and Background

The Arctic Ocean freshwater budget influences the global climate system. Important parts of the freshwater budget are the Pacific Water inflow through Bering Strait, Atlantic Water inflow through the Barents Sea and Fram Strait, continental river runoff, precipitation−evaporation (P−E), and outflow of liquid water and ice through deep Fram Strait and the shallow straits of the CAA towards the North Atlantic (Aagaard and Carmack, 1989). Geographic locations of the different components can be seen in Fig. 1.1. A simple ocean-sea-ice model suggests that the ocean transport of freshwater through Fram Strait is about 60% of that through the CAA (Steele et al., 1996) but contributions from ice are small in the CAA due to the presence of land-fast ice (Prinsenberg and Bennett, 1989; Melling et al., 2008). Freshwater storage especially in the Beaufort Gyre means that the budget does not have to balance at any given time, rather pulses of freshwater release can occur during specific climate regimes (Proshutinsky et al., 2009). When freshwater is released from the Arctic Ocean towards the North Atlantic it can influence deepwater formation in the Labrador and Greenland Seas and therefore the Meridional Overturning Circulation (Lazier, 1980; Hakkinen, 1993; Hakkinen, 1999; Rennermalm et al., 2006; Stouffer et al., 2006; Wu et al., 2008).

Significant changes have recently been observed in the Arctic region including changes in sea ice drift pattern and upper ocean circulation (Polyakov and Johnson,

2000; Rigor et al., 2002), changes in Arctic sea ice cover (Fig. 1.2, Lindsay and Zhang, 2005; Stroeve et al., 2005; Lindsay et al., 2009), a strengthening and warming of the Atlantic inflow through Fram Strait (Holliday et al., 2008), an increased run-off into the Eurasian sector (Peterson et al., 2002), and increased sea-ice outflow through Nares Strait (Kwok et al., 2010). All these changes can have an influence on the freshwater budget and its consequences; most changes appear to correlate with atmospheric forcing (Serreze and Francis, 2006). Salinity also shows temporal and spatial variability over a wide range of scales in the CAA and adjacent oceans.

Obtaining reliable volume and freshwater flux estimates and describing the hydrography in Nares Strait as part of the CAA is particularly important; longer-term measurements did not exist in Nares Strait—one of the main channels in the CAA. Flux estimates may be used to monitor change, and to constrain the models used to make climate predictions. Note, however, that few of the current generation of climate models allow any flow of water through the channels of the CAA, with unknown consequences for projections. The CAA poses several challenges such as an ice-cover during up to nine months out of the year, closeness to the magnetic North Pole, and remote location (Melling, 2000). Unpredictable ice conditions in the short summer season have resulted in only limited expeditions to this area in the past.

This study focuses on Nares Strait, the north-eastern most strait in the CAA to the NW of Greenland. Sadler (1976) deployed current meters for 40 days, Bourke et al. (1989) investigated temperature and salinity during one summer season, and Münchow et al. (2006) evaluated data from two-day ADCP surveys in Nares Strait. Nares Strait facilitates a total southward volume flux estimated to be 0.57 ± 0.09 Sv (Münchow and Melling, 2008), 0.7 Sv (Sadler, 1976), and 0.8 ± 0.3 Sv (Münchow et al., 2006). This compares to a net yearly southward volume transport in Fram Strait of 2 ± 2 to 4 ± 2 Sv (Schauer et al., 2004). Both straits are comparable for

freshwater flux with Fram Strait exporting more freshwater in solid form and Nares Strait exporting more freshwater in liquid form.

Between 2003 and 2006 moorings were deployed in Nares Strait to investigate variability from tidal to interannual time scales for the first time. Münchow and Melling (2008) published first results of vertically averaged current variability while Samelson and Barbour (2008) discussed results from the atmospheric modeling component.

Ice conditions in Nares Strait change between two states. Between June/August and November/March multi-year ice is drifting through the strait while during the remainder of the year ice is land-fast. An ice bridge forms in Smith Sound anytime between November and March blocking ice advection (Dunbar, 1973; Barber et al., 2001; Kwok, 2005; Dumont et al., 2009; Kwok et al., 2010). Ice bridges are anchored to the coasts of both Greenland and Canada and tidal currents as well as local winds impact their formation (Samelson et al., 2006; Dumont et al., 2009). An ice index, defined by Münchow and Melling (2008), distinguishes between the two ice states in Nares Strait.

The conductivity, temperature, and pressure data set collected during the project is evaluated here with regard to hydrography and salinity variability. It is also essential to obtain reliable flux estimates and to describe the time dependence of flows through Nares Strait, which is addressed in this dissertation as well. Fluxes through Nares Strait also reflect impacts of diminishing sea ice in the Arctic (Parkinson and Cavalieri, 2008), disintegrating ice shelves in northern Canada (Copland et al., 2007), and potentially surging glaciers and ice loss from the ice sheet in northern Greenland (Rignot and Steffen, 2008; Khan et al., 2010), especially influencing freshwater content. We need to know conditions in the different pathways, what the forcing mechanisms of the flow through the straits are in order to establish a baseline first. This work is part of the Canadian Archipelago Throughflow (CAT)

Study as part of the larger Arctic Sub-Arctic Ocean Fluxes (ASOF) program.

1.2 Research Questions

Research questions for Nares Strait arise with respect to oceanographic conditions on different spatial and temporal scales, forcing mechanisms, and future implications of findings. This dissertation investigates the following questions for the 2003–06 time period:

- How successful was the novel mooring design for CT instruments with less buoyancy in the top layers? What is the best way to analyze this data set and which methodology proofs successful? Is this a reliable design to measure properties closer to the surface (within 30 m) and within an area of large iceberg threat?

- What are the hydrographic conditions in Nares Strait and how do they change over time?

- What are the characteristics of the geostrophic flow and how is the geostrophic flow changing over the three years?

- How are the geostrophic volume and freshwater fluxes through Nares Strait characterized? What is their mean, their variability, how do they change over time (with ice seasons, years, etc.)?

- What are the forcing mechanisms of the geostrophic fluxes through the strait?

- Is the flow through Nares Strait in geostrophic balance? What is the result of a direct comparison between geostrophic and ADCP velocity?

Time series analysis and statistical methods were used in this dissertation to answer the above questions. Note that this list of questions is not inclusive. The

three-year data set includes other instrumentation that is not covered here that lead to more research questions to be answered in the future. More research questions resulting from the answers found in this dissertation are placed at the end of the dissertation in the future work section 5.2.

1.3   Dissertation Overview

This dissertation focuses on an innovative three-year mooring data set of temperature, conductivity, and pressure records in Nares Strait. Two different methodologies were used to evaluate the novel CT data set that avoids iceberg encounter and bends under the influence of tides, strong currents, and icebergs. The year-round presence of ice and icebergs poses a constant threat to all moored equipment deployed in these waters. These challenges require both unique mooring design and data processing. Therefore, we discuss our mooring design, non-standard methods, and calibration in detail in the data and appendices sections of chapters 2 and 3 before describing oceanographic research results.

First, I describe the three-year mean hydrography, the variability seen in the salinity field, and water masses from these moored records and compare them with snapshots of more traditional survey data. Salinity variability in space and time, and a large Arctic freshwater incursion event in July 2005 are described. A dependence on the ice cover is revealed using statistical analysis.

Next, an analysis of geostrophic currents and fluxes along with a more time-dependent analysis follows. Variability in salinity and geostrophic velocity on different time scales are quantified. Geostrophic volume and freshwater fluxes are presented. Different forcing mechanisms—local wind and along-channel pressure gradient forcing—are discussed next.

Chapter 4 demonstrates a comparison between geostrophic and ADCP velocities. The comparison during different ice states reveals a discrepancy during all ice conditions close to the Ellesmere Island side, which is analyzed in detail.

5

The dissertation then concludes and gives a future outlook. This includes science questions and possibilities related to the extended data set from 2007–09 and 2009–11, described in more detail.

Chapter 2 is in press at the Journal of Geophysical Research–Oceans, (**Rabe, B.**, A. Münchow, H. Johnson and H. Melling, 2010: Nares Strait Hydrography and Salinity Field From a Three-Year Moored Array. *J. Geophys. Res.*, doi:10.1029 /2009JC005966, in press). Chapter 3 is a journal article forthcoming (**Rabe, B.**, H. Johnson, A. Münchow and H. Melling, 2010: Geostrophic Ocean Currents and Freshwater Fluxes Across the Canadian Polar Shelf via Nares Strait). The word "we" in both chapters refers of all authors.
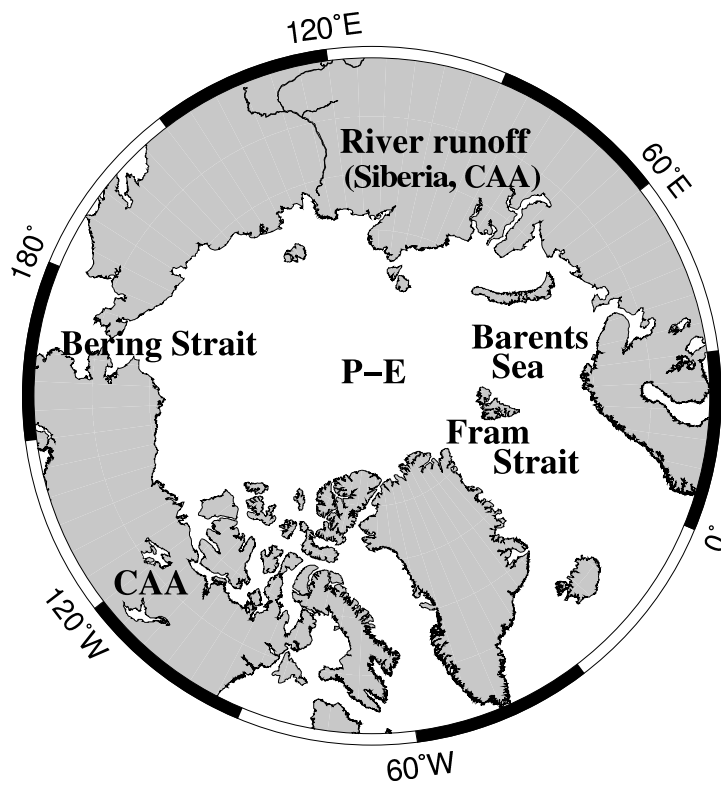
Figure 1.1: Map of the Arctic Ocean including locations of components of freshwater budget: Pacific Water inflow through Bering Strait, Atlantic Water inflow through Barents Sea and Fram Strait, continental river runoff off Siberia and CAA, precipitation−evaporations (P−E) throughout the Arctic, and outflow of liquid water and ice through Fram Strait and straits in the CAA.
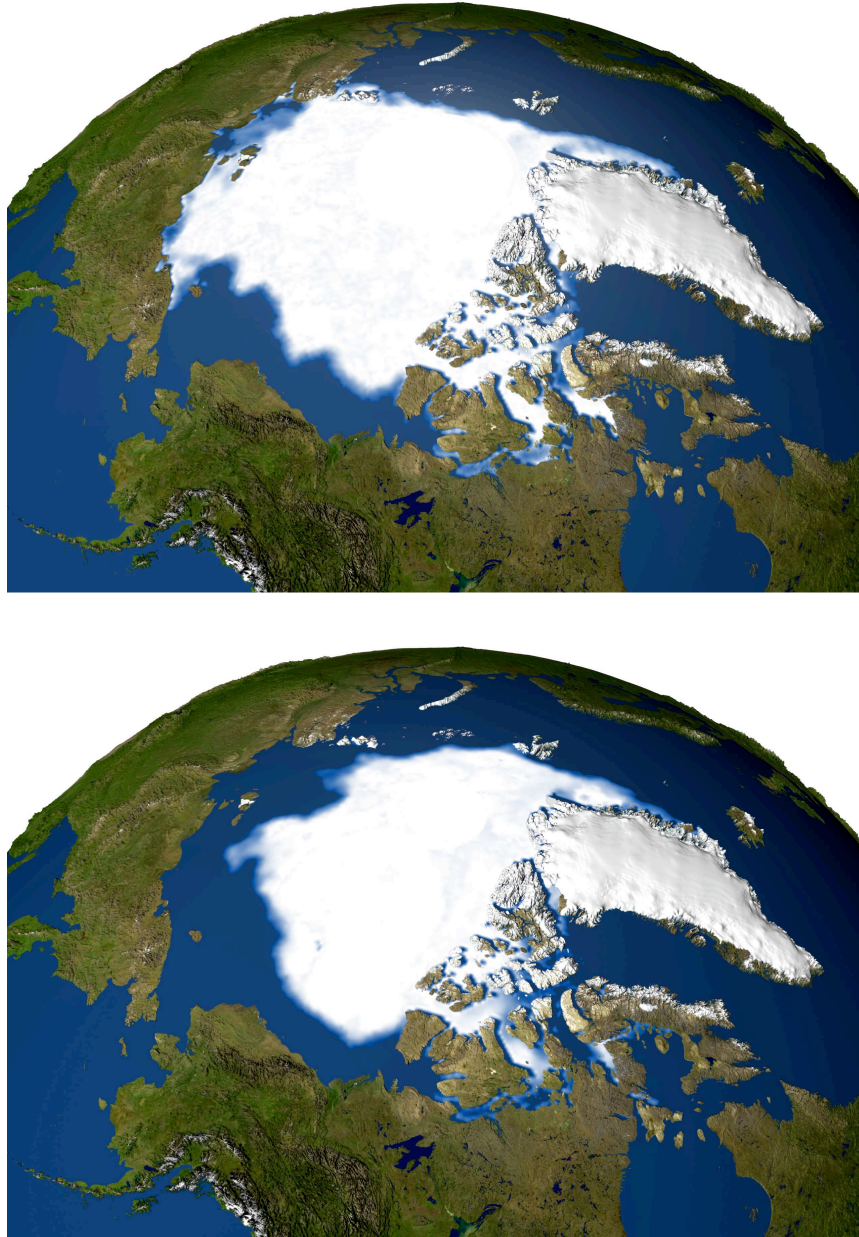
Figure 1.2: Arctic sea ice extend minimum in 1979 (top) and 2005 (bottom) showing the large decline in sea ice extent observed from satellites. This is just one example of the recent changing conditions in the Arctic region (http://www.nasa.gov /centers /goddard /news /topstory /2005 /arcticice_decline_prt.htm)

Chapter 2

NARES STRAIT HYDROGRAPHY AND SALINITY
FIELD FROM A THREE-YEAR MOORED ARRAY

2.1 Abstract

Nares Strait to the west of Greenland facilitates the exchange of heat and freshwater between the Arctic and Atlantic Oceans. This study focuses on salinity, temperature, and density measurements from Nares Strait from a mooring array deployed from 2003–2006. Innovative moorings requiring novel analysis methods measured seawater properties near 80.5°N, at spacing sufficient to resolve the internal Rossby deformation radius. The three-year mean geostrophic velocity has a surface-intensified southward flow of 0.20 m s^{-1} against the western side of the strait and a secondary core flowing southward at 0.14 m s^{-1} in the middle of the strait. Data shows warm salty water on the Greenland side and cold fresher water on the Ellesmere Island side, especially in the top layers. There was a clear difference in hydrographic structure between times when sea ice was drifting and when it was land-fast. Ice was drifting in late summer, fall, and early winter with a strong surface-intensified geostrophic flow in the middle of the strait. Ice was land-fast in late winter, spring, and early summer, when there was a sub-surface core of strong geostrophic flow adjacent to the western side of the strait. Salinity variations of about two psu in time and space reflect a variable freshwater outflow from the Arctic Ocean. One particularly strong pulse occurred at the end of July 2005. For several days, steeply sloping isohalines indicated strong geostrophic flow down the

middle of the strait coinciding with an amplified ice export from the Arctic due to strong southward winds.

2.2 Introduction

The heat and freshwater budgets of the Arctic Ocean play an important role in the global climate system. Freshwater fluxes towards the North Atlantic occur through the shallow straits of the Canadian Arctic Archipelago (hereafter CAA) and deep Fram Strait (Aagaard and Carmack, 1989). A simple ocean-sea-ice model suggests that the ocean transport of freshwater through Fram Strait is about 60% of that through the CAA (Steele et al., 1996) but contributions from ice are small in the CAA due to the presence of land-fast ice (Prinsenberg and Bennett, 1989; Melling et al., 2008). These freshwater fluxes into the Labrador and Greenland Seas are a source of buoyancy that stratifies the water column and, if it reaches deep convection regions, reduces deep convection.

Atlantic water flows into the Arctic Ocean through Fram Strait and Barents Sea (Fahrbach et al., 2001; Schauer et al., 2002) while Pacific Water enters through Bering Strait (Coachman and Aagaard, 1966; Woodgate and Aagaard, 2005). Assemblies of these water masses are augmented by run-off from the Eurasian and American continents and return to the Atlantic via Fram Strait and the CAA. Waters are modified in transit, but their origins remain clear.

Salinity shows temporal and spatial variability over a wide range of scales in the CAA and adjacent oceans. For example, the "Great Salinity Anomaly" was a freshwater anomaly that traveled throughout the North Atlantic between 1968 and 1982. It originated from Fram Strait, traveled southward in the East Greenland Current and freshened the central Labrador Sea (Dickson et al., 1988). Numerical models such as Goosse et al. (1997), Tang et al. (1999), and Wadley and Bigg (2002) simulate the connection between changes in freshwater fluxes (for example caused

by the "Great Salinity Anomaly") and convection, but these spatially coarse resolution models do not represent the coastal and rim-current systems in the Greenland and Labrador Seas (Sutherland and Pickart, 2008). Koenigk et al. (2007) use 20th century and Intergovernmental Panel on Climate Change scenario runs for an investigation of the changing freshwater export out of the Arctic Ocean using a model with grid spacing of about 15 km around Greenland. They suggest an increase in the liquid freshwater outflow through the whole CAA from about 60 mSv (Sv = 10^6 m^3 s^{-1}) to more than 100 mSv by 2100 without distinguishing between different straits in the CAA. Obtaining reliable volume and freshwater flux estimates and describing the hydrography in Nares Strait as part of the CAA is particularly important; longer-term measurements did not exist in Nares Strait—one of the main channels in the CAA—as they do for example in Lancaster Sound (Prinsenberg and Hamilton, 2005). Flux estimates may be used to monitor change, and to constrain the models used to make climate predictions. Note, however, that few of the current generation of climate models allow any flow of water through the channels of the CAA, with unknown consequences for projections.

Nares Strait to the west of Greenland facilitates a total southward volume flux estimated to be 0.57 ± 0.09 Sv (Münchow and Melling, 2008), 0.7 Sv (Sadler, 1976), and 0.8 ± 0.3 Sv (Münchow et al., 2006). This compares to a net yearly southward transport in Fram Strait of 2 ± 2 to 4 ± 2 Sv (Schauer et al., 2004). The net southward Atlantic Water flux in Nares Strait is about 0.59 ± 0.13 Sv and the net southward Pacific Water flux is about 0.32 ± 0.04 Sv (Münchow et al., 2007). Ice flux through Nares Strait is small as ice is land-fast during most of the year. Unpredictable ice conditions in the short summer season have resulted in only limited expeditions to this area in the past.

First studies in Nares Strait include Sadler (1976) who interpreted data from a 40-day long data set of current measurements, and Bourke et al. (1989) who

evaluated temperature and salinity during one summer season. Münchow et al. (2006) used data from a synoptic two-day ADCP survey to evaluate fluxes. The first longer-term measurements were conducted as part of the Canadian Archipelago Throughflow Study from 2003 to 2006. This project resulted in three-year data sets from ADCP moorings with first results regarding interannual to tidal variability and forcing published by Münchow and Melling (2008). The conductivity, temperature, and pressure data set collected during the project is evaluated here with regard to hydrography and salinity variability. Also included in the project was an atmospheric modeling component (Samelson and Barbour, 2008).

The width of a baroclinic flow in geostrophic balance scales with the internal Rossby deformation radius:

$$L_D = \frac{(g'D_0)^{1/2}}{f} \qquad (2.1)$$

with $g' = \frac{\Delta \rho g}{\rho_0}$ the reduced gravity, ρ_0 the mean density, $\Delta \rho$ the density difference, g the gravitational constant, f the Coriolis parameter, and D_0 the vertical scale of motion. This is the fundamental spatial scale of motion in the CAA (Leblond, 1980), and is about 10 km for Nares Strait Münchow et al., 2006), significantly less than the width of the strait.

This study introduces the novel three-year data set of temperature, conductivity, and pressure records (section 2.3) from the moored array in Nares Strait, that resolves the density and thus geostrophic velocity field at the scale of the internal Rossby deformation radius. The year-round presence of ice and icebergs poses a constant threat to all moored equipment deployed in these waters. These challenges require both unique mooring design and data processing. Therefore, we discuss our non-standard methods in detail in section 2.4 and Appendix A (2.10.1). Section 2.5 then describes the three-year mean hydrography and water masses from these moored records and compares them with snapshots of more traditional survey data.

Salinity variability in space and time, and a large Arctic freshwater incursion event, are described in sections 2.6 and 2.7, respectively. The results from this study are discussed in section 2.8, and section 2.9 contains concluding remarks. This paper focuses on characterizing the three-year mean and the variability seen in the salinity field; a second paper in preparation ("Geostrophic ocean currents and freshwater fluxes through Nares Strait, West of Greenland" by Rabe et al.) will explore in more detail the physics governing variability in the flow.

2.3   Study Area and Data Sources

The Canadian Archipelago lies on the Canadian polar shelf, amid a network of straits and basins that provide pathways for flow between the Arctic Ocean and the North Atlantic. This study focuses on Nares Strait in the northeast CAA between Ellesmere Island and Greenland. The channel is less than 400 m deep and 38 km wide and comprises, from north to south, Robeson Channel, Hall Basin, Kennedy Channel, Kane Basin and Smith Sound (Fig. 2.1a). Conductivity-temperature (CT) mooring strings were deployed across the strait in Kennedy Channel at about 80.5°N, about 50 km north of the 230 m deep sill. The CT moorings were about 5 km apart. All instruments were deployed in August 2003 from USCGC *Healy* and recovered in 2006 from CCGS *Henry Larsen*. Specifically, we recovered 24 SeaBird SBE37SM Microcats (hereafter CT instruments) from 6 moorings; 2 moorings were lost (see Table 2.1 and Fig. 2.1b for mooring locations in the strait). Additional recovered ADCP moorings are discussed by Münchow and Melling (2008), and included a further 4 CT instruments.

The CT recorders were supported on taut-line moorings at four depths, nominally 30 m, 80 m, 130 m, and 200 m (Fig. 2.2). Actual depths when drawdown was zero are listed in Table 2.1. One acoustic transponder-release was attached above the anchor. The buoyancy above 200-m depth on each mooring was small, so

that the top of the mooring pulled down appreciably in strong current. The mooring relied on strings of small plastic floats for buoyancy at upper levels, instead of conventional large spherical floats. The sensitivity to current was deliberate: since icebergs sweep larger volumes per unit time in strong current, pull-down in such conditions reduces the likelihood of strikes. This design proved essential for the survival of the moorings during their three-year deployment (only two moorings were lost, both in shallow locations). For example, during its first year of deployment one instrument was pulled down from its nominal 30 m location to below 200-m depth by a passing iceberg. The slender mooring design ensured that no damage occurred during this iceberg encounter and that data collection continued for another two years. The "normal" drawdown of the top-most instrument by tidal current was about 50 m. Twice a day near slack tide, when the mooring straightened up, observations were acquired within 30 m of the surface. This novel mooring design, which encouraged large vertical movement of the CT instruments, introduces new challenges to the processing of time series data.

To facilitate the processing and analysis of data, about half of the CT instruments were equipped with pressure sensors to measure depth. Fig. 2.3 illustrates the record-mean position of each instrument within the cross-section and shows the naming convention of moorings. Individual CTD sensors were placed near the top (nominal 30-m depth) and bottom (nominal 200-m depth) of the array of sensors, bracketing two CT instruments without pressure sensors placed at nominal 80-m and 130-m depths (Fig. 2.2).

The instruments were factory calibrated prior to deployment and checked for calibration issues after recovery. Biological fouling was minimal on all instruments. The sampling interval was 15 minutes. All instruments returned a gap-free three-year conductivity and temperature record, but the pressure record at one instrument terminated after 500 days. We adjusted the records of each instrument for

(a) a generally small clock drift (<three minutes per year), (b) a small number of spikes (<0.01%), and (c) a recorded pressure drift. The latter was accomplished by comparing in-air pressure readings at the beginning and the end of the record. Measured pressures were not corrected for variations in tide and sea-level atmospheric pressure, which in combination spanned a full range of values of 5 dbar with a standard deviation of 0.9 dbar during the period of recording estimated from pressure measured three meters above the seabed at ADCP mooring KS10.

2.4   Methods

Currents associated with the barotropic tide in Nares Strait cause most of the observed drawdown of instruments on moorings. These currents are both deterministic and predictable (Padman and Erofeeva, 2004; Münchow et al., 2006; Münchow and Melling, 2008). Münchow and Melling (2008) find from a three-year time series of vertically averaged along-channel currents that 66.4% and 26.3% of the total variance reside within the semidiurnal and diurnal bands, respectively. For the dominant M_2 tidal currents the flow along the major axis—along-channel—reaches 21.2 ± 0.1 cm s^{-1}, and K_1 reaches 13.0 ± 0.7 cm s^{-1}. The tides therefore lend support to the use of linear system analysis in de-convolving the effect of drawdown on time series data.

First, pressure is interpolated between CT instruments at nominal 30 and 200-m depth to the location of the two instruments without pressure sensors at nominal 80 and 130-m depth. A linear variation of pressure along the mooring line is assumed. Details about the pressure interpolation can be found in Appendix 2.10.1.1.

Next the effect of mooring motion and tides need to be minimized. We used a linear system analysis which is described in detail in Appendix 2.10.1.2. The analysis acts as a pre-processing step before applying filters also described in the Appendix (2.10.1.3). The final time series are low-pass filtered time series of temperature

15

and salinity that are incoherent with cyclical vertical movement of CT sensors in response to varying tidal current.

We define the along- and across-channel directions as x- and y-coordinates, respectively, therefore u is the along-channel velocity (positive southward) and v the across-channel velocity (positive eastward). For thermal wind we use the depth $z_0 = 200$ m as a level of known motion to estimate the mean geostrophic velocity for our mooring section. We use the mean of available ADCP data from moorings KS02, KS10 and KS12 at 200 m (discussed in Münchow and Melling (2008)) i.e., $u_0(y, z_0) = 0.04$ m s^{-1}. The three-year mean velocity is uniform across the strait at this depth.

For the analysis of salinity variability we will use Empirical Orthogonal Functions (EOF) to decompose observations into mutually uncorrelated (orthogonal) modes of variability. An extensive description of EOFs can be found in Appendix B (2.10.2).

2.5   Mean Hydrography and Water Masses

In order to evaluate different water masses in Nares Strait, we present temperature-salinity correlations in Fig. 2.4 using the three-year mean of the time series from each instrument at each mooring (black triangles) and compare them to CTD data from a section across Kennedy Channel during 2007 for the same depth range. Note that CTD data were obtained in summer only and that ice conditions prevented us from taking measurements within five km of Ellesmere Island. For salinities larger than 33 psu, the mean water mass properties match the instantaneous CTD observations well since water masses at depth (warm and salty conditions) show less variability (see sections of standard deviation of salinity and temperature in Fig. 2.5). These warm and salty subsurface waters below about 80-m depth contain waters of Atlantic origin (Münchow et al., 2006). Considerable scatter exists for the cooler and fresher waters of the upper layer that contains local

16

ice melt and lies closer to the freezing point. The local ice melt—leading to salinity variations in the top layers—only occurs during the drift ice season. The three-year mean from CT instruments captures both drift and fast-ice conditions and we would therefore not expect it to agree closely with a summer snapshot measured by CTD. The three-year mean is representative of the lower layers throughout the year due to low variability, but not representative of upper layer conditions in any particular season.

Fig. 2.5 shows the same, three-year average hydrographic conditions plotted as sections across southern Kennedy Channel. Again, we distinguish a surface layer of cold and fresh water that becomes warmer and saltier both with depth and towards Greenland. Temperatures drop almost to the freezing point at a salinity of 32 psu. Below 100-m depth we find warm and salty waters of Atlantic origin that are most pronounced on the Greenland side with temperatures of up to almost 0°C and salinities as high as 34.5 psu in the three-year mean. Temperature has little influence on density at these low temperatures. The across-channel density gradient in Nares Strait is caused by fresher waters in the west and saltier waters at depth in the east. Isopycnals thus slope upwards towards Greenland which implies an across-channel baroclinic pressure gradient which, if geostrophically balanced, corresponds to a southward flow of up to 0.14 m s^{-1} near the center of the channel at the surface.

Standard deviations about these mean properties demonstrate temporal variability that varies substantially across the strait (Fig. 2.5). Small standard deviations for salinity occur at depth and near the channel center where they are generally less that 0.2 psu. Water properties below 150 m are similar across the section and, it will become clear in the next section, are largely independent of seasonal changes such as the presence of ice. We find the highest standard deviation of almost 0.5 psu in the surface layer off Ellesmere Island where we find the freshest water, while off

Greenland the standard deviation reaches 0.3 psu. A minimum of salinity variability occurs near the channel center where the slopes of isopycnal surfaces are large. This suggests a steady geostrophic flow and we will argue below that this is the location of strong southward flow. For temperature the largest standard deviations are about 0.2°C both near Greenland and Ellesmere Island. The pattern of variability for density mimics salinity since density follows salinity at low temperatures.

2.6   Salinity Variability

We performed an EOF analysis of the salinity data from our 24 time series across Kennedy Channel to investigate dominant in-phase patterns of co-variability in salinity. We find that the first two modes explain almost 3/4 of the total variance contained in the 24 time series. Specifically, mode one explains 54% and mode two explains 19% of the total variance. The principal component time series $a_1(t_k)$ and $a_2(t_k)$ (Fig. 2.6) are normalized so that they always have a zero mean and a variance of one. This treatment aids the interpretation of the spatial patterns $\phi_1(\vec{x_i})$ and $\phi_2(\vec{x_i})$ (Figs. 2.7 and 2.8), because these now are in practical salinity units. It is important to recall that EOFs only describe statistical variances about a mean that is not part of the analysis. Therefore, each mode n modifies the mean $\bar{S}(\vec{x_i})$ by either adding or subtracting its pattern $S_n(\vec{x_i})$ to the mean pattern (Harms and Winant, 1998; Münchow and Chant, 2000; Pickart, 2004).

Figs. 2.6a and b show the time series $a_1(t_k)$ and $a_2(t_k)$ representing an amplification factor in time of the time invariant patterns shown in Figs. 2.7 and 2.8 as the positive $(\bar{S}(\vec{x_i}) + S_n(\vec{x_i}))$ and negative $(\bar{S}(\vec{x_i}) - S_n(\vec{x_i}))$ deviations from the mean $\bar{S}(\vec{x_i})$. Also shown in Fig. 2.6a in gray is the ice index following Münchow and Melling (2008) to distinguish drift ice from fast-ice conditions. The intervals with a negative index correspond to mobile ice in late summer, autumn, and early winter and those with a positive index correspond to fast-ice conditions in late winter, spring, and early summer. During fast-ice conditions, there is a no-slip constraint

18

on flow at the surface (retarding surface stress). In Fig. 2.6b the gray line represents an annual cycle with minima at the end of August and maxima at the beginning of January.

Mode one (Fig. 2.7a) shows highest salinity variability in the top 150 m within 20 km of Ellesmere Island with anomalies of up to 0.4 psu from the mean. Strongest gradients occur in the middle of the strait. A zero-line lies along the bottom of the observed section. A second zero line reaches the surface at approximately 10 km from the Greenland coast, so that the top layers on the Greenland side show negative values. This means that change occurs in the same direction across the strait except in the top layers on the eastern side.

The mean plus mode one $(\bar{S}(\vec{x_i}) + S_1(\vec{x_i}))$ (Fig. 2.7b) shows a fresh top layer with salinities of about 32.5 psu across the whole strait. Isohalines shoal slightly upwards to the east within 10 km of Ellesmere Island suggesting an increased geostrophic flow. The positive values in the time series (Fig. 2.6a) coincide with fast-ice conditions, shown by the positive ice index. Variability of short period is much reduced during this time because fluctuations in wind stress cannot influence the strength and direction of current when ice is fast.

The mean minus mode one $(\bar{S}(\vec{x_i}) - S_1(\vec{x_i}))$ (Fig. 2.7c) reveals the freshest water with 31.8 psu in the top layer on the Ellesmere Island side. The 32.5 psu isohaline reaches down to 80 m on the Ellesmere Island side and shoals towards Greenland to about 35 m. Isohalines shoal towards the Greenland side with strongest gradients between 15 and 20 km off Ellesmere Island. The stronger gradient there suggests an increased southward geostrophic flow in the middle of the strait. In the time series (Fig. 2.6a) the negative values coincide with drift ice conditions, as demonstrated by the negative ice index. Such conditions are typically characterized by mobile pack ice on the western side of the strait, with lower ice concentrations or open water to the east. Variability is high during this time because fluctuations

in wind stress directly influence the strength and direction of current. This means that during the ice drifting season the implied geostrophic flow is strongest in the top layers in the middle of the strait.

Mode two (Fig. 2.8a) describes a negative region of up to -0.1 psu between 80 and 150 m on the Ellesmere Island side and a positive region with up to 0.3 psu on the Greenland side in a thin top layer. Lateral gradients in the top 80 m are concentrated within 15 km of the Greenland shore. The deepest layer has the same value across the whole strait, close to zero, meaning there is less variability below about 180 m. The opposing signs suggest a seesaw behavior between the top layer and the 80 to 150 m layer closest to Ellesmere Island: if the top layer is saltier than usual, the mid-layer on the Ellesmere Island side will be fresher and vice versa.

The mean plus mode two $(\bar{S}(\vec{x_i}) + S_2(\vec{x_i}))$ (Fig. 2.8b) shows a pattern with reduced stratification and isohalines shoaling towards the Greenland side. Freshest water of about 32.4 psu occurs again on the Ellesmere Island side in the top layers and saltiest water in the lowest layers on the Greenland side with almost 34.5 psu. In the time series (Fig. 2.6b) the positive values in mode two occur between end October/beginning of November and mid-March.

The mean minus mode two salinity pattern $(\bar{S}(\vec{x_i}) - S_2(\vec{x_i}))$ (Fig. 2.8c) shows a fresh surface layer with salinities of about 32 psu and isohalines sloping upwards to the east in the western half of the strait at depth. The stratification is considerably stronger between about 50 m and 150 m. These times characterized by a negative mode two salinity amplitude occur between mid-March and the end of October/beginning of November.

The amplitude of salinity EOF mode one (Fig. 2.6a) clearly changes between fast and drift ice conditions. The amplitude of mode two (Fig. 2.6b) changes on an annual cycle with minima, maxima, and changes in sign occurring at the same time each year. This means mode two is more highly correlated with date than

with ice conditions. Since it reflects largely surface changes, we can speculate that it is associated with changes in the amount of surface Arctic meltwater advected through the strait or remotely forced sea-surface height gradients. Based on the analysis above we propose that mode one represents lateral variation across the strait during drift ice conditions and mode two represents a tendency for surface-intensified northward flow, strongest on the Greenland side, to accompany strong southward flow near 100 m depth on the Ellesmere side, and vice versa. The modal analysis suggests that ice conditions influence the salinity structure within Nares Strait.

The arrow in Fig. 2.6a denotes a mode-one event more than three standard deviations from the mean, corresponding to a drop of around 1.6 psu in salinity within two days. We describe this large freshwater incursion next.

2.7 Freshwater Incursion

The data reveal large temporal variability in salinity, especially during drift ice conditions and especially in the upper ocean on the Ellesmere side. One extreme event occurred around year day 942, at the end of July 2005 (also seen in Fig. 2.6a). We here present salinity sections for two-day means starting at days 938–940 (26–28 July 2005) and continuing throughout the event until days 946–948 (3–5 August 2005) (Fig. 2.9). Prior to the event (Fig. 2.9a) we find salinities of around 32 psu in the top layer on the Ellesmere Island side, saltier water at depth and further offshore, and small isohaline slopes. During days 942–944 (Fig. 2.9c) a strong freshwater incursion occurs in the top layer within 15 km of Ellesmere Island. The salinity drops to almost 30 psu (also see Fig. 2.10) and the isohalines move from almost parallel to the sea surface before the event to a steeper slope during this event, especially in the middle of the strait. The 34 psu isohaline, for example, slopes from almost 200 m off Ellesmere Island up to roughly 150 m off Greenland. Using thermal wind, the implied geostrophic velocity for this event, shown in Fig. 2.11,

indicates a southward flow in the top layers in the middle of the strait of up to 0.30 m s^{-1}; a reference level velocity of 0.02 m s^{-1} from ADCP data at 200 m depth during this event was used. Geostrophic velocities of up to 0.20 m s^{-1} exist in the middle of the strait down to about 80 m. Stronger flow also exists in the top layers on the Ellesmere Island side but is less pronounced (0.17 m s^{-1}). At days 944–946 (Fig. 2.9d) this low salinity signal only occurs within 10 km of Ellesmere Island and at days 946–948 (Fig. 2.9e) the signal is only present in a very shallow top layer. Isohalines move back to the original position after the intrusion has passed.

Fig. 2.10a shows the filtered salinity time series for a two-week period for all instruments on the mooring closest to Ellesmere Island (KS01, instrument mean depths indicated). The top instrument here shows the sharpest drop in salinity of the whole three-year and 24-instrument record. The other top instruments across the strait exhibit similar but less prominent salinity variations (not shown). The strong signal around day 942 in the top instrument represents a drop from 31.7 psu to 30.1 psu (ΔS). The drop occurs in less than two days (Δt) and gives a $\frac{\Delta S}{\Delta t} = 0.82$ psu day^{-1}. With depth the signal diminishes, and there is no evidence of the freshening in the lower two instruments. Therefore, the signal is most pronounced close to Ellesmere Island and in the surface layer. If this is a purely advective feature, e.g.,

$$\frac{\partial S}{\partial t} \sim u\frac{\partial S}{\partial x} \tag{2.2}$$

then we can calculate Δx, the along-channel length scale. With $u \sim 0.30$ m s^{-1} and $\Delta S^x \sim 1.6$ psu we find $\Delta x \sim 50$ km. This is the distance that a water parcel would get advected during this strong event if the salinity anomaly observed was a purely advective feature. Downwelling favorable winds from the north and associated southward advection of ice along Ellesmere Island contributed to this extreme event. Fig. 2.10b shows the predicted along-channel wind during the freshwater incursion from a mesoscale atmospheric circulation model by Samelson

and Barbour (2008); no direct observations exist. Wind speeds reach 12 m s^{-1} to the south on day 942 (30 July 2005), before the wind slows down and eventually changes direction. Satellite images reveal that the western half of the strait was covered by heavy ice at this time (Fig. 2.12). Southward ice drift measured by Doppler sonar at site KS02 ranged between 0.5 and 1.5 m s^{-1} during days 937–943 (25–31 July 2005). Rapid ice drift and the wind data confirm that this event was indeed forced by strong wind from the north.

2.8 Discussion

Using thermal wind, we calculate the three-year mean geostrophic velocity for depths between 35 and 200 m, estimated from measured hydrographic properties that are averaged over the observational period (Fig. 2.4) with a level of known motion from ADCP data. This calculation captures the baroclinic component of the geostrophic flow from the CT data plus the component introduced by the reference ADCP velocity and is shown in Fig. 2.13. Positive velocities indicate a flow to the south. Shear in geostrophic velocity occurs mainly in the upper 150 m. The section shows a surface-intensified southward flow on the Ellesmere Island side of up to 0.20 m s^{-1} and high mean velocities of up to 0.14 m s^{-1} in the middle of the strait.

Münchow and Melling (2008) show a time-mean and depth-averaged northward flowing current of 0.04 $\pm$ 0.01 m s^{-1} close to Greenland from the three-year ADCP data set which is not apparent in the geostrophic flow field (Fig. 2.13) because the CT section does not reach the Greenland shore. CT measurements closest to the Greenland side show warm and salty water of Atlantic origin at depth. One possible origin of Atlantic water with warm and salty characteristics in Nares Strait is from the south via an extension of the West Greenland Current in the northward flowing current on the Greenland shelf. Most of the West Greenland Current turns cyclonically west across Baffin Bay while following the 500-m isobath but a fraction continues north along the Greenland coast (Bourke et al., 1989; Melling et al., 2001;

23

Bacle et al., 2002). Another possibility is that Atlantic water is advected from the north through the Arctic Ocean. The Atlantic source water flowing through Nares Strait is coming mainly from the Barents Sea branch lower halocline (Rudels et al., 2004). Below 100-m depth in Nares Strait up to 80% of the water is traceable to the North Atlantic Ocean (Jones and Eert, 2006); Münchow et al. (2007) also found water of Atlantic origin in the deeper layers in Nares Strait. Jones et al. (2003) conclude, based on nutrient data, that the most likely origin of Atlantic water in Smith Sound is the Arctic Ocean.

Channel flows in a rotating frame of reference are often controlled by friction and geostrophy (Gill, 1982). Stratified flows scale with the internal Rossby radius of deformation. In Nares Strait this radius is about 10 km (Münchow et al., 2006) and sets the width of baroclinic flow in geostrophic balance (Leblond, 1980; Gill, 1982). With the ~ 5 km spatial resolution of our moorings in Nares Strait the internal Rossby radius of deformation is resolved and we thus are confident to interpret the spatial structure of the flow. This spatial scale is evident during a particularly strong salinity event when the fresh outflow from the Arctic Ocean is concentrated within 10 km of Ellesmere Island. The spatial structure of anomalies apparent in the EOFs of salinity also indicates that spatial variation is largely confined within an internal deformation radius of the western and eastern shorelines.

2.9   Conclusions

We have had success with an innovative mooring designed to support CT sensors at shallow depth while minimizing risk from icebergs in Nares Strait. The moorings small components and low net buoyancy within the domain of greatest risk above 200-m depth allow it to be drawn down out of harms way when current (and iceberg drift) is fast.

Nares Strait is "wide" in the sense that its width exceeds the internal deformation radius by a factor of about four. It is clear that the high spatial resolution

of our moored array in Nares Strait is essential to elucidate ocean features in this strait.

A frequency domain linear system analysis was used to minimize the "noise" arising from the drawdown of sensors. While not without limitations, this method improves signal to noise ratios and thus statistical confidence from our three-year observational study of Nares Strait.

The three-year mean geostrophic current flows southward on the western side of the channel. Direct measurements by ADCP near the coast of Greenland during the same time period (Münchow and Melling, 2008) indicate that current flows northward there. As a three-year average, the geostrophic flow through the section in Kennedy Channel is southward and surface-intensified with a maximum of 0.20 m s^{-1} on the Ellesmere Island side and a secondary maximum of 0.14 m s^{-1} at the shallowest depth of measurement (35 m) near the middle of the section, including a reference level velocity from ADCP data (discussed in Münchow and Melling, 2008). This long-term average flow structure is qualitatively consistent with synoptic snapshots in summer using vessel-mounted ADCP (Münchow et al., 2006; Münchow et al., 2007) and with measured enhanced drawdown of the CT moorings positioned near the center of the strait (Münchow and Melling, 2008).

The waters found on opposite sides of Nares Strait have different characteristics. Those on the western (Ellesmere) side are colder and less saline than those on the Greenland side. Isopycnals generally have their maximum slope near the middle of the strait consistent with the enhanced geostrophic velocity here. The freshest, coldest water is found near the sea surface on the Ellesmere Island side, flowing southward from the Arctic Ocean as a buoyant outflow similar to a coastal current (Yankovsky et al., 2000; Bacon et al., 2002; Chapman, 2003; Pickart et al., 2005). Over the three-year survey the greatest temporal variability in salinity was observed within this cold outflow. In contrast, the greatest temporal variability

in temperature was observed on the Greenland side. Variability is small at depth where waters are isolated from surface salt and heat fluxes by ice cover and by a statically stable water column.

An EOF analysis of salinity variations across the section has revealed two modes that together explain 3/4 of the total variance. Mode one is surface-intensified and has maximum amplitude at the coast of Ellesmere Island; with negative eigenvalue it represents a south-flowing buoyant boundary current. Mode two represents a tendency for surface-intensified northward flow, strongest on the Greenland side, to accompany strong southward flow near 100 m depth on the Ellesmere side, and vice versa. Interplay of these modes can create a seesaw behavior between the Ellesmere and Greenland sides of the strait and between the top and the middle depths close to Ellesmere Island. When the top layer is saltier, the mid-layer on the Ellesmere Island side is fresher and vice versa, resulting in times of small and large vertical stratification.

The sea ice of Nares Strait alternates between drifting and fast conditions on an irregular annual cycle. Ice is most commonly drifting during late summer, autumn, and early winter, and most commonly fast during late winter, spring, and early summer. The ice index switches between the two phases and was defined by Münchow and Melling (2008). The first EOF mode of salinity variations appears to be correlated with the state of the ice cover, so that the cross-strait variation in surface salinity is strongest during drifting ice conditions. The annual modulation of the second EOF model of salinity variations appears better correlated with date than with ice condition; the variation is large and positive at the beginning of January (high surface salinity) and large and negative at the end of August (low surface salinity). In combination, these modes create strong geostrophic current near the ocean surface mid-strait in late summer, and a sub-surface jet of geostrophic current adjacent to Ellesmere in mid-winter.

The most intense anomaly in salinity occurred in July 2005. Salinity at 35-m depth decreased by close to two psu over two days and isohalines shoaled sharply near the middle of the strait. This event can also be seen in the principal component time series of the first EOF mode of salinity with a large, negative amplitude indicating a location near the surface on the Ellesmere side. The associated geostrophic flow was southward at 0.30 m s^{-1} in the top layers in the middle of the strait. At the same time a rapid ice export within the Rossby radius of deformation close to Ellesmere Island existed, associated with strong southward winds.

Clearly anomalies in flow and in salt deficit are correlated during fluctuations with period as short as a few days in Nares Strait. For this reason a quick calculation of freshwater flux by multiplication of the mean field of current times that of salinity deficit will be biased low by an amount not known at this time. Moreover, there are two other sources of appreciable negative bias that we do not yet have a handle on. The first arises from our lack of observations of salinity and current in the upper 35 m of the ocean, where momentum and freshwater are very strongly concentrated. The second arises from our lack of observations within the 20% of the 38-km cross-section within one Rossby scale of the coastlines of Greenland and Ellesmere Island. The poorly understood interaction of geostrophic and frictional effects in these lateral boundary layers is a disincentive to casual interpolation of data across them at his time. We therefore postpone a careful presentation of our best knowledge of volume and freshwater fluxes through Nares Strait to a future publication.

2.10   Appendices

2.10.1   Appendix A: Signal Processing

2.10.1.1   Pressure Interpolation

We have interpolated values of pressure between CT instruments at nominal 30 and 200-m depths to the locations of the two instruments at intermediate nominal 80 and 130-m depths assuming a linear variation of pressure along our mooring line

(a straight line when the mooring is tipped over). Linear interpolation has been justified via simulations of mooring performance in current by a static mooring model (Bell, 1979), which predicts a linear behavior for our mooring design.

Testing this assumption, we use the KS03 pressure record at 80-m nominal depth (Fig. 2.3) for an intercomparison of the interpolated pressure with actually measured pressure. A linear regression between the modeled pressure p_{mod} and the measured pressure p gives

$$p_{mod} = 0.9867p + 2.0364 \qquad (2.3)$$

and explains 99% of the variance. The unexplained variance suggests an interpolation error of about $\pm$ 3 dbar at 95% confidence. The histogram (Fig. 2.14) reveals that the distribution of modeled minus measured pressure is Gaussian. Therefore the modeled pressure represents the actual pressure of that instrument well. The non-zero intercept for the regression could be caused by the slightly shallower actual mooring depth (instrument two was located at 79 m at zero drawdown), or uncertainties in the model calculations or input velocities. We will exploit accurate pressure estimates at all instruments at all times in the subsequent linear system analysis to minimize the impact of mooring motion. We then calculate salinity from conductivity, in-situ temperature, and pressure using the standard algorithm (UNESCO, 1983), as well as the density anomaly σ_t.

2.10.1.2 Linear System Analysis

Mooring motions lead to large variations in pressure and corresponding salinity and temperature variations in the raw time series data. These variations occur mostly at tidal periods because tidal currents constitute almost 93% of total current variance in Nares Strait (Münchow and Melling, 2008). In order to analyze time

series data from CT sensors we need to minimize the effects of both mooring motion and tides.

Fig. 2.15a shows the raw pressure data for a 50-day segment of the three-year time series from the instrument near the surface and closest to Ellesmere Island (KS01). It reveals the dominant tidal influence on the instruments depth as the drawdown varies from 0 to 50 m. Vertical motion of instruments is smaller lower down on the mooring; for example it is only about 10 m at 200 m depth (not shown).

To reduce this signal caused by mooring motion we use the pressure data to remove the part of the salinity (temperature) signal that is coherent with the drawdown through a frequency domain linear system analysis. Münchow et al. (1992) and Münchow (1998) have previously used this method to reduce noise due to sea-level changes (local winds and freshwater discharge) in current data. We assume a single input—single output linear system. The single input—single output model looks like:

$$p(t) \rightarrow \boxed{\text{H(f)}} \rightarrow y(t) = y_c(t) + y_{ic}(t) \tag{2.4}$$

where $p(t)$ is pressure (measured input), $H(f)$ is the linear transfer function as a function of frequency f (the frequency response function of a constant-parameter linear system between $p(t)$ and $y(t)$) with $y(t)$ as the salinity and temperature measurements (measured output), $y_c(t)$ is the component that is coherent (subscript c) with pressure fluctuations and $y_{ic}(t)$ is the component that is incoherent (subscript ic) with pressure fluctuations. We assume that the salinity and temperature signals consist of two components (coherent plus incoherent).

In order to find the signal $y_{ic}(t)$, we estimate H as a function of frequency f between $p(t)$ and $y(t)$ as

$$Y(f) = H(f)P(f) + Y_{ic}(f) \tag{2.5}$$

where $Y(f)$ and $P(f)$ are the Fourier transforms of $y(t)$ and $p(t)$, respectively, while $Y_{ic}(f)$ is the signal that is incoherent with the pressure fluctuations. We find the time series of interest for subsequent analyses $y_{ic}(t)$ from the inverse Fourier transform, i.e.,

$$y_{ic}(t) = F^{-1}[Y(f) - H(f)P(f)] \tag{2.6}$$

The method is applied separately to data from individual instruments, using a times series of pressure (i.e. depth) and either salinity or temperature. Since it is an analysis of variations the average value of each time series is subtracted before the method is applied, and will be added back in to the incoherent part of the variability to give the final time series.

Fig. 2.15b shows the raw salinity data (before the mean is removed) that includes both coherent and incoherent parts with pressure. Figs. 2.15c and d show the coherent and incoherent parts of the salinity signal, respectively, with the mean added back in, for the sample 50-day time series. The resultant time series are assumed to represent a variable at the record-mean depth for each instrument where their locations are shown as symbols in Fig. 2.3.

The linear system analysis relies on several assumptions. First, it assumes that a change in the depth of the instrument via drawdown in the tidal flow generates a proportional change in salinity (or temperature). However, the change in salinity (or temperature) with drawdown is equally influenced by the vertical derivative in that characteristic, which is not part of the linear system. In the extreme case where the vertical derivative approaches zero, salinity (or temperature) does not change in response to drawdown; this is visible, for example, during days 275–313 in Fig. 2.15.

Second, the linear system analysis treats the time series as statistically stationary and ergodic; that is, it assumes that the data have statistical properties that are invariant with translations in time (Bendat and Piersol, 1993). As a consequence

30

the linear transfer function $H(f)$ represents an average over intervals wherein fluctuations are large (days 270–275), and intervals wherein they are small (days 275–313). Since we use $H(f)$ to de-convolve drawdown effects from the whole time series, the corrections are insufficient during certain intervals (like days 270–275) and introduce spurious "incoherent" signal during other intervals (e.g. days 275–313). With salinity, for which drawdown always increases the value, the "incoherent" value is too high where the deconvolution falls short, and too low where the deconvolution is too enthusiastic. These imperfections of the linear systems analysis have, as we demonstrate, little impact on the discussion of subtidal variability because most of the mooring motion is caused by tidal currents. Hence we interpret the linear system analysis as a pre-processing step that increases signal to noise ratios by reducing substantial noise prior to the application of low-pass filters.

2.10.1.3   Filters

Removing signals with frequencies higher than tidal, we filter the pressure-coherent $y_c(t)$ and pressure-incoherent $y_{ic}(t)$ parts of each salinity and temperature time series with a Lanczos raised-cosine low-pass filter that has a cut-off period near 40 hours and a window width of 50 hours. Figs. 2.15c and d show the low-pass filtered time series of pressure-coherent and pressure-incoherent salinity, respectively, for the example 50-day window, in black. The incoherent part $y_{ic}(t)$ has a similar signature as the raw salinity signal. Notice that some tidal signals are still present in the incoherent part $y_{ic}(t)$ prior to filtering. These may arise from either tidal advection of horizontal property gradients or imperfections of the linear systems analysis. Low-pass filtering removes these tidal signals. Our analyses will use these low-pass filtered data that are incoherent with pressure fluctuations.

2.10.2 Appendix B: Empirical Orthogonal Functions

EOFs were first introduced to atmospheric science by Lorenz (1956) and later to oceanography by Davis (1976) and Kundu and Allen (1976). We here apply them to the pressure data to demonstrate that our entire sensor array moves in a largely correlated fashion in response to tidal currents. Furthermore, in section 2.6 we discuss spatial and temporal salinity variations as seen in the EOFs.

EOFs decompose observations $S(\vec{x_i}, t_k)$ at $\vec{x_i} = (x, z)_i$ with $i = 1, 2, ...I = 24$ discrete locations in the strait and t_k with $k = 1, 2, ...K = 105654$ samples in time into mutually uncorrelated (orthogonal) modes of variability. Each mode has a temporal amplitude $a_n(t_k)$ and a spatial pattern $\phi_n(\vec{x_i})$ for the $n = 1, 2, ...N = 24$ modes, that is

$$S(\vec{x_i}, t_k) = \sum_{n=1}^{N} (a_n(t_k) * \phi_n(\vec{x_i})). \tag{2.7}$$

$a_n(t_k)$ are eigenfunctions and $\phi_n(\vec{x_i})$ are eigenvectors to an eigenvalue problem

$$R_{i,n} * \phi_n(\vec{x_i}) = \lambda_n * \phi_n(\vec{x_i}) \tag{2.8}$$

with $R_{i,n}$ being the zero-lag cross-covariance matrix of size 24*24 of the observations at locations $(\vec{x_i})$. λ_n is the eigenvalue for the n-th mode and is interpreted as the variance associated with the n-th mode. The functions $a_n(t_k)$ and $\phi_n(\vec{x_i})$ are subject to an orthogonality condition

$$\sum_{i=1}^{I} \phi_n(\vec{x_i}) * \phi_m(\vec{x_i}) = \delta_{nm} \tag{2.9}$$

with δ_{nm} being the Kronecker delta with $\delta = 0$ for $n \neq m$ and $\delta = 1$ for $n = m$.

We performed an EOF analysis on the raw pressure data; a 50-day sample period is shown in Fig. 2.15a. Fig. 2.15e shows the temporal evolution of the first mode $a_1(t_k)$ that represents 71% of the variance. The time series is non-dimensional, has

32

a zero mean, and a normalized variance of one. Fig. 2.16 depicts the corresponding spatial pattern of mode one, that is, $\phi_1(\vec{x_i})$ in dbar. This fixed pattern in space is modulated in time by values shown in Fig. 2.15e. In the spatial pattern we find the same sign across the strait with highest variability of about 17 dbar in the surface layer in the middle of the strait and values close to zero at around 200 m. The maximum vertical excursion in the deeper center of the channel is expected, as both tidal and subtidal currents are largest near this location (Münchow and Melling, 2008). Our results indicate that the mooring motion is strongly correlated at all instrument locations (Figs. 2.15e and 2.16).

2.11 Acknowledgments

Table 2.1: CT instruments: Mooring name, location (Latitude, Longitude), record length [days], depths with zero drawdown, and type of CT instruments

Mooring	Latitude	Longitude	record length [days]	depths and type of instruments [m]
KS01	80 33.4702 N	68 54.4556 W	1108	30* 80 130 200*
KS03	80 32.6972 N	68 47.3071 W	1104	29* 79* 129 199*[1]
KS05	80 31.1389 N	68 34.8083 W	1104	27* 77 127 197*
KS07	80 29.3721 N	68 19.4548 W	1105	32* 82 132 202*
KS09	80 27.3490 N	68 03.8391 W	1104	38* 88 138 208*
KS11	80 25.6500 N	67 47.8325 W	Not recovered	17* 67 117 187*
KS13	80 23.8010 N	67 34.5747 W	1106	32* 82 132 202*
KS15	80 22.5009 N	67 25.8209 W	Not recovered	47* 97 106*

*: pressure sensor
1: pressure sensor malfunction after 500 days
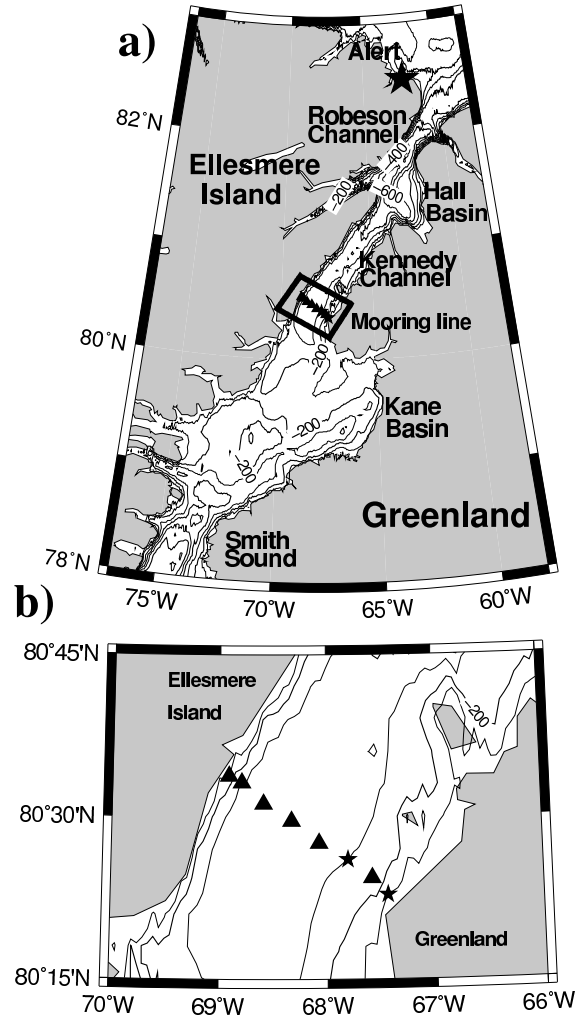
Figure 2.1: Study Area: a) Nares Strait bottom topography with thick black line of triangles denoting CT mooring locations. Greenland lies to the east of Nares Strait. Robeson Channel is in the northern part of the strait, Hall Basin connects to Kennedy Channel at roughly 81°N and Kane Basin connects to Smith Sound to the south with a sill depth of 230 m. The big star shows Alert in northeastern Ellesmere Island. The black box is the area zoomed in for b) with more detail on exact mooring locations. b) Mooring line across Nares Strait with triangles denoting recovered CT mooring strings and stars denoting lost CT mooring strings.
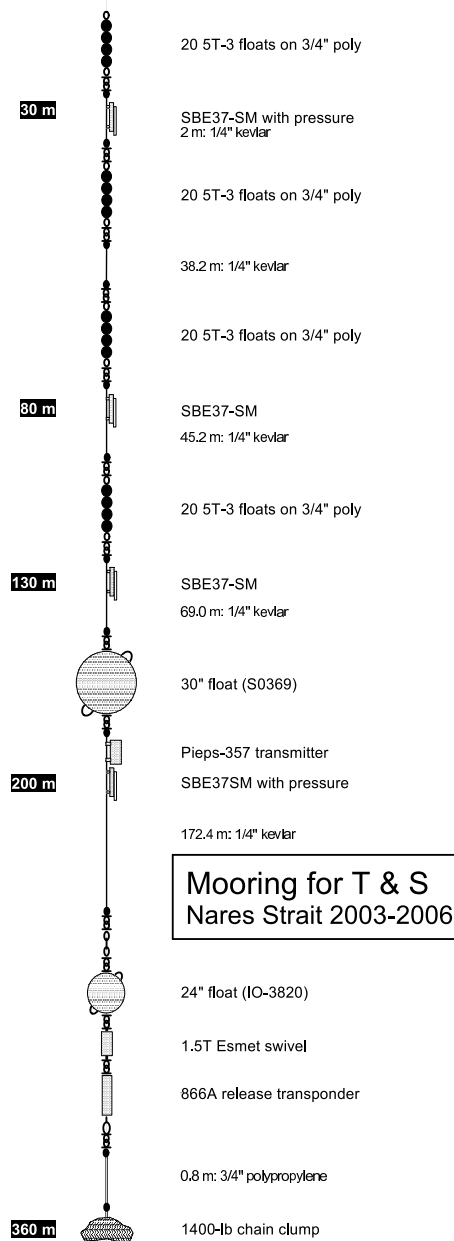
Figure 2.2: Sketch of CT mooring design: anchor at the bottom, acoustic release and most of the buoyancy below 200 m, four CT instruments per string at nominal 30, 80, 130 and 200 m with flexible Kevlar cable between instruments. This novel mooring design with low buoyancy in the upper water column allows the mooring to bend under the influence of ice, and profile through the water column at tidal frequencies.
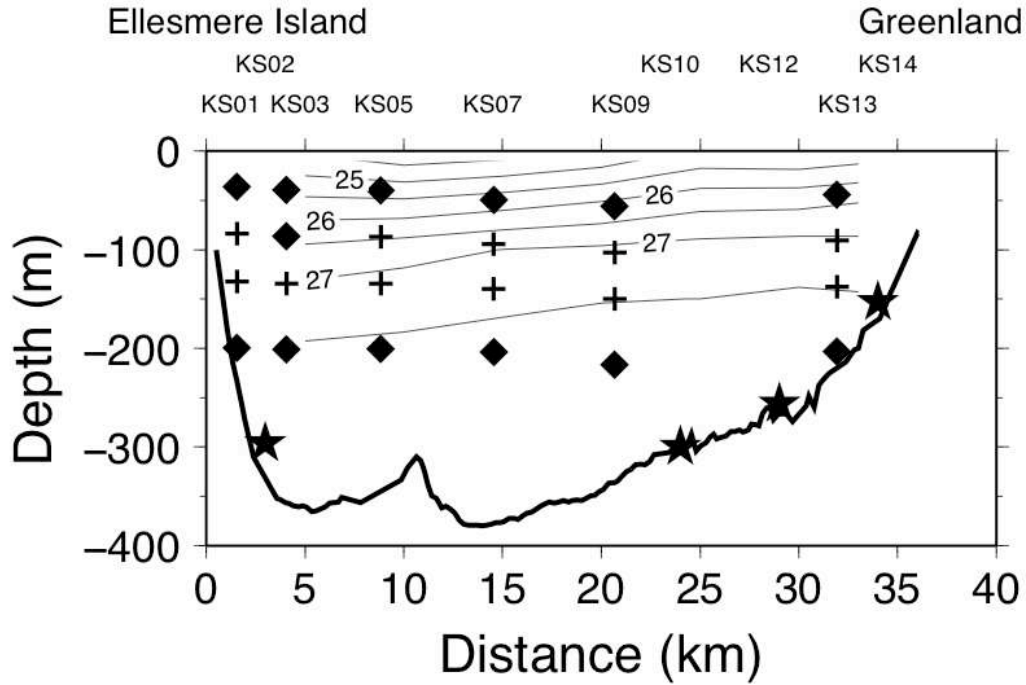
Figure 2.3: Position of recovered CT moorings and ADCPs in the strait, with Ellesmere Island on the left (west) and Greenland on the right (east). CT moorings consist of four instruments at nominal 30, 80, 130 and 200 m, crosses and diamonds denote the record-mean depth for each instrument; diamonds show instruments with pressure sensor, crosses without. Bottom-mounted ADCPs are shown as stars. Mooring numbering is in sequence starting on the Ellesmere Island side with CT moorings as odd numbers and ADCPs as even numbers. Contour lines represent density anomaly from CTD measurements in 2007.
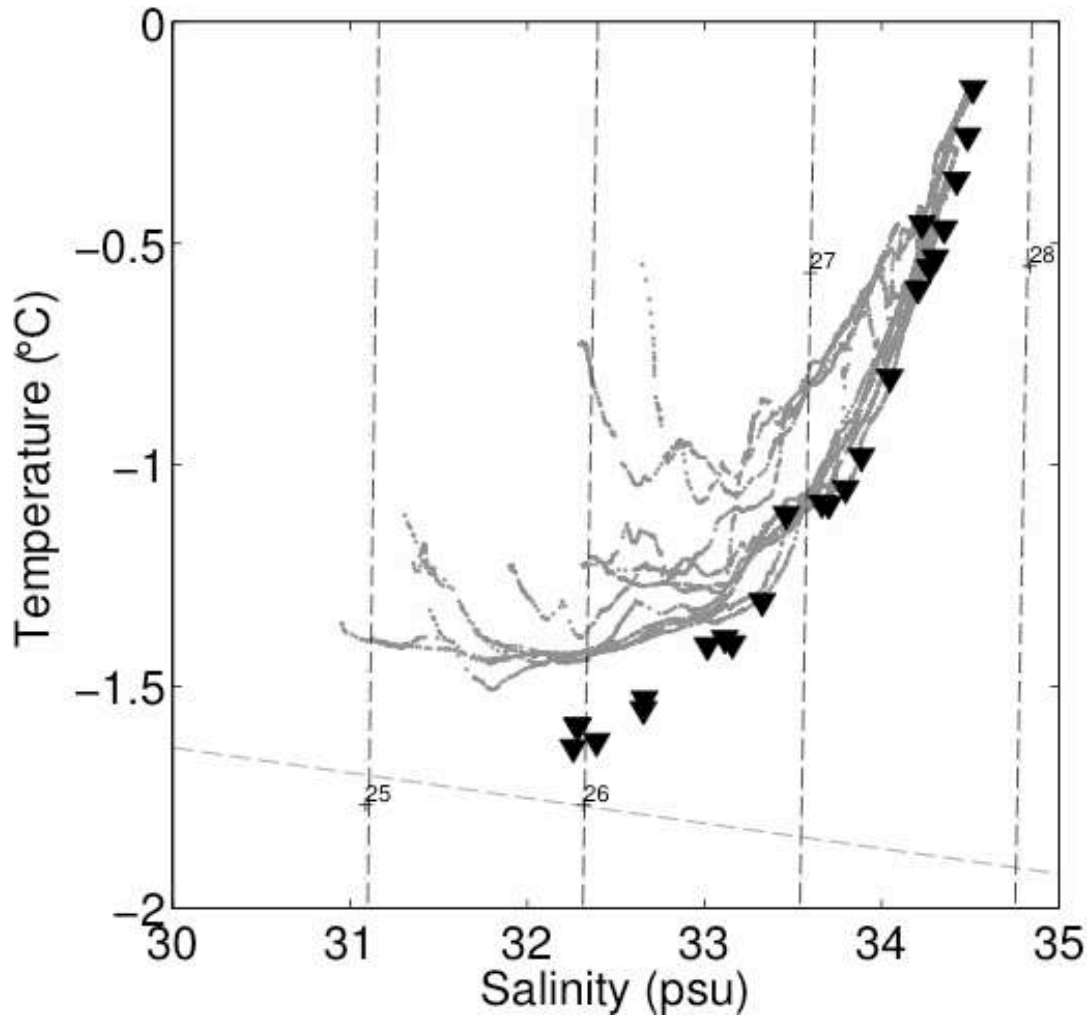
Figure 2.4: Three year mean TS-diagram from CT mooring data (black triangles), and CTD data across Kennedy Channel during 2007 from the same depth range of 35 to 200 m (gray dots). Also included are the freezing line (light gray dashed) and σ_t lines (dark gray dashed). Note that the westernmost five km of the strait could not be measured by CTD because of heavy ice. All CTD measurements were taken in summer. For salty warm water masses the two different data sets compare well; for fresh cold water masses they diverge.
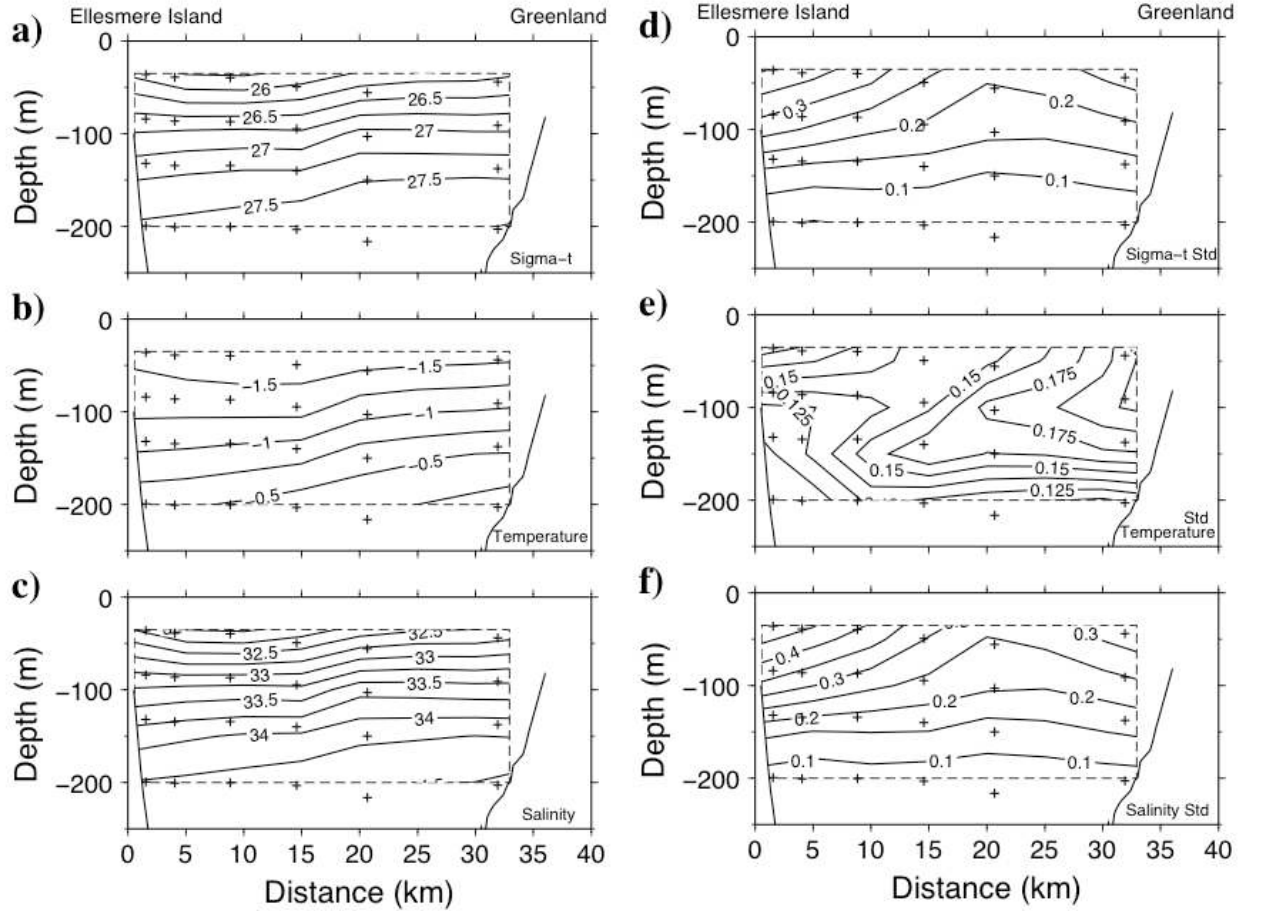
Figure 2.5: Three-year mean of a) density anomaly σ_t, b) temperature, and c) salinity across the mooring section, and standard deviations for d) density anomaly σ_t, e) temperature, and f) salinity. Black crosses denote the instrument record-mean positions. Cold fresh water masses exist on the Ellesmere Island side, getting warmer and saltier with depth and towards Greenland.
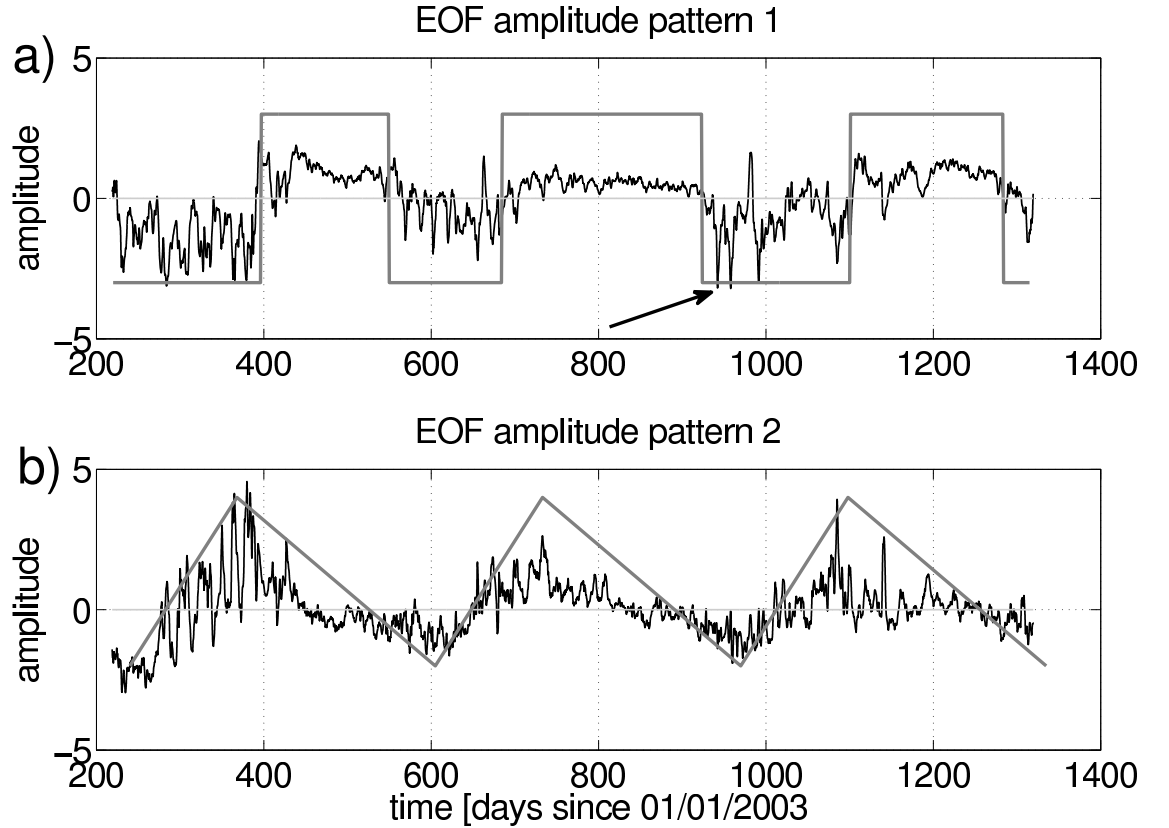
Figure 2.6: Temporal evolution of eigenfunctions of salinity variability of a) mode one (54% of the variance) (the arrow marks the strong event in salinity, more than three standard deviations from the mean, described in the freshwater incursion section), b) mode two (19% of the variance). The time series are non-dimensional and have a variance of one. The dark gray line in (a) represents the ice index which is positive for land-fast ice (mid-October–mid-June) and negative for drift ice (mid-June–mid-October) conditions. The dark gray line in (b) represents an idealized annual cycle. The light gray line is the zero line to better distinguish between positive and negative values. Mode-one salinity structure appears linked to the state of the ice cover while mode-two structure relates best to the time of year.
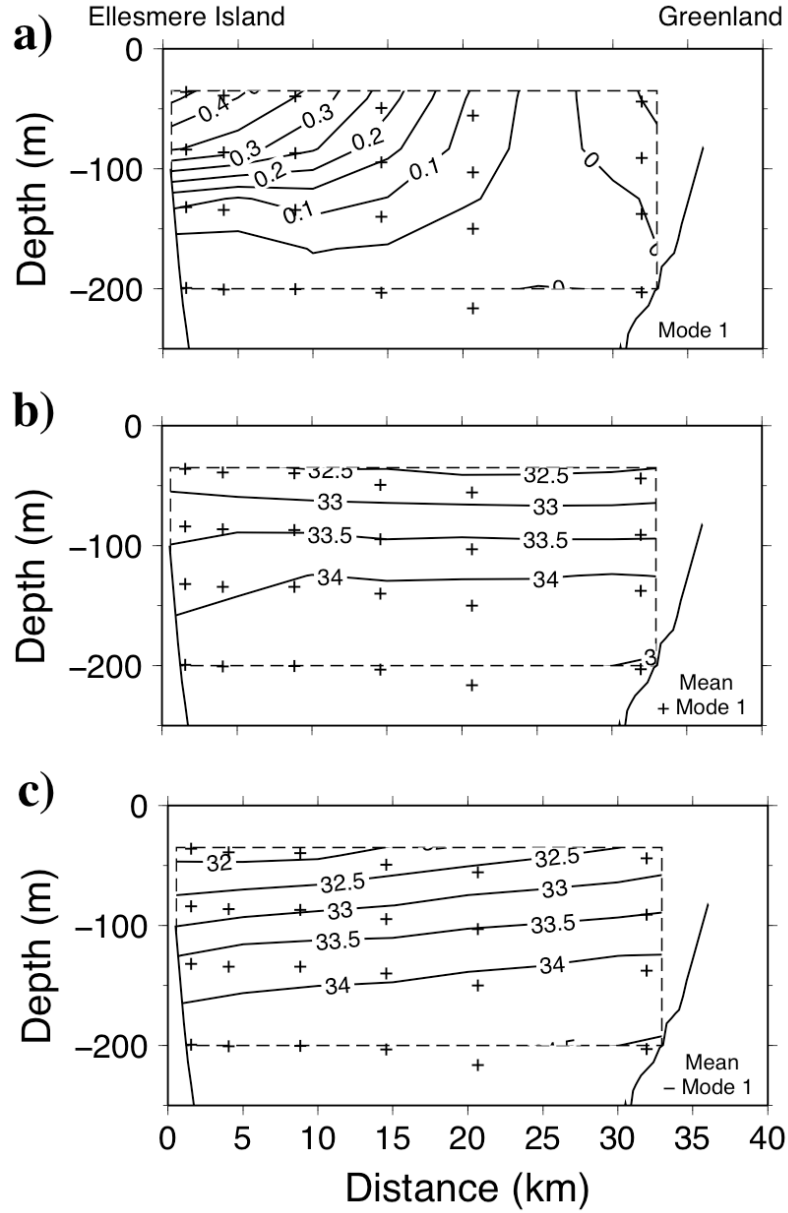
Figure 2.7: EOF spatial structure of salinity variations shown in combination with the mean salinity field: a) mode one (54% of the variance), b) mean plus mode one, c) mean minus mode one. The contour lines are the same for b) and c) for ease of comparison. Black crosses denote the instrument record-mean positions. Mode one explains horizontal variations in salinity especially on the Ellesmere Island side.

41
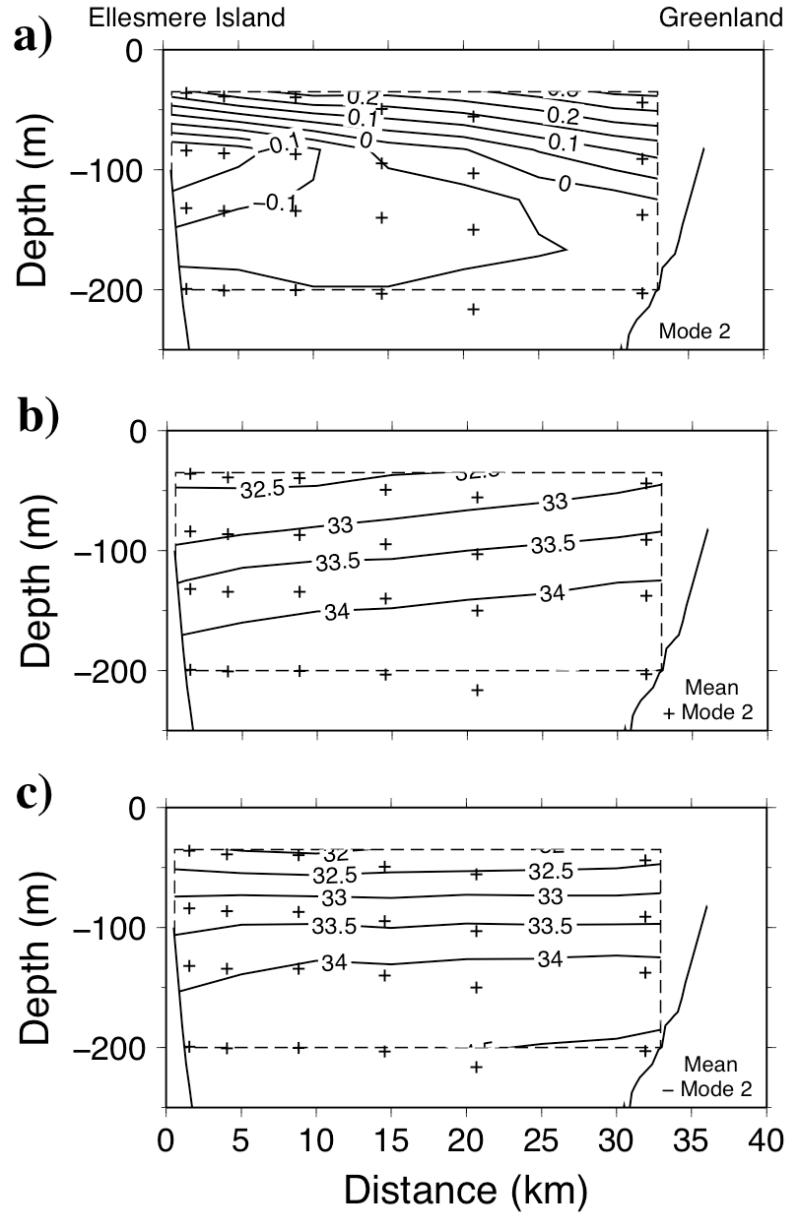
Figure 2.8: EOF spatial structure of salinity variations shown in combination with the mean salinity field: a) mode two (19% of the variance), b) mean plus mode two, c) mean minus mode two. The contour lines are the same for b) and c) for ease of comparison. Black crosses denote the instrument record-mean positions. Mode two shows a tendency for surface-intensified northward flow, strongest on the Greenland side, to accompany strong southward flow near 100 m depth on the Ellesmere side, and vice versa.
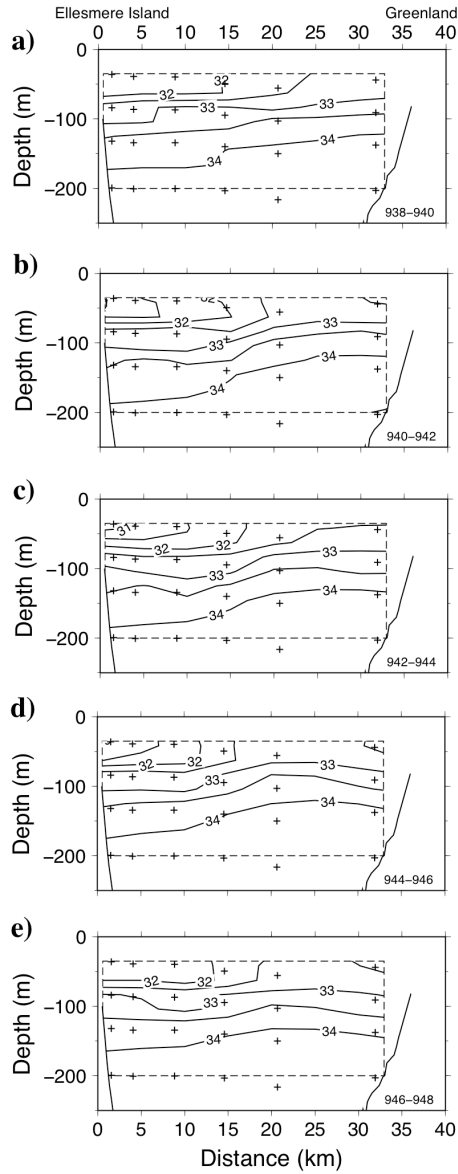
Figure 2.9: Sections of two-day mean salinity at year days: a) 938–940 (26–28 July 2005), b) 940–942 (28–30 July 2005), c) 942–944 (30 July–1 August 2005), d) 944–946 (1–3 August 2005, e) 946–948 (3–5 August 2005), showing the freshwater incursion in the top layers on the Ellesmere Island side and the sloping of the isohalines, especially in c). The contour interval is 0.5 psu in all panels. Black crosses denote the instrument record-mean positions.
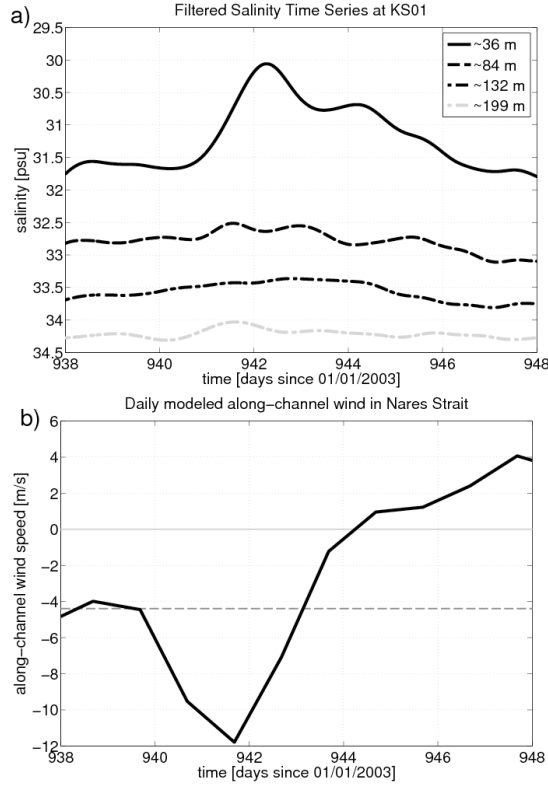
Figure 2.10: a) Filtered salinity time series for a 10-day period for all four instruments on the Ellesmere Island side. The strong salinity event during year day 940–942 (28–30 July 2005) shows a surface salinity (record-mean depth of 36 m) on the Ellesmere Island side reduced by almost two psu. The black line represent the top instrument on the Ellesmere Island side, the dashed line the second instrument from the top at a record-mean depth of 84 m, the dot-dashed line the third instrument from the top at a record-mean depth of 132 m and the gray dashed line represents the lowest instrument at a record-mean depth of 199 m on the Ellesmere Island side. b) Daily modeled along-channel wind in Nares Strait for the same 10-day period (black) with negative values representing wind speeds to the south. The dotted dark gray line shows the three-year mean wind speed. The light gray line is zero wind speed to emphasize a switch in wind direction. A strong southward wind exists between 940–942 (28–30 July 2005) during the same time as the salinity dropped.

44
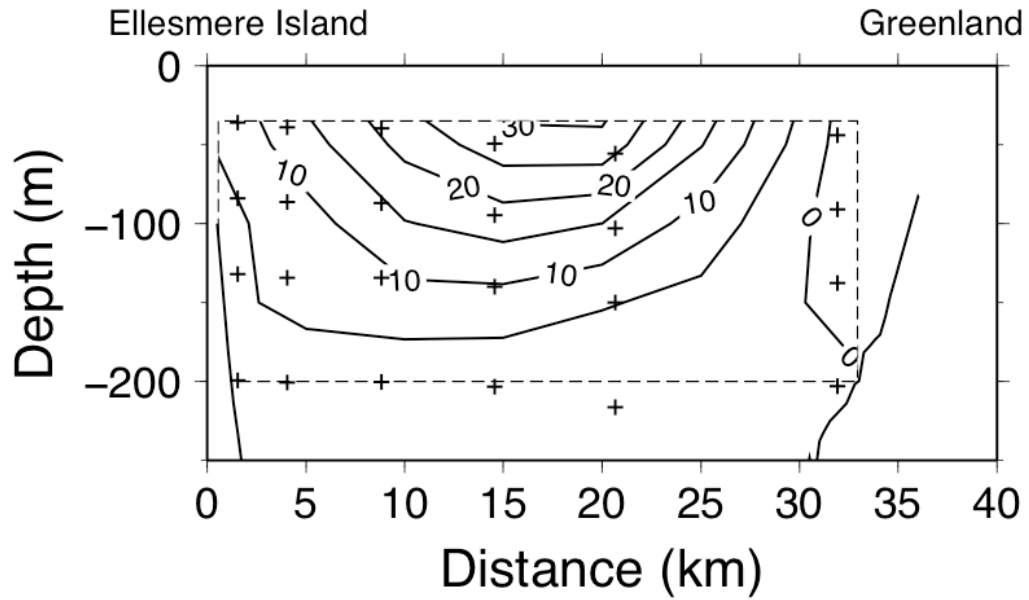
Figure 2.11: The geostrophic velocity section during the strong salinity event in cm s^{-1}. Black crosses denote the instrument record-mean positions. Positive values denote flow to the south. A reference velocity of 0.02 m s^{-1} from ADCP mooring data during this event is used as a level of known motion at 200 m. The surface-intensified flow is most pronounced in the middle of the strait with values of up to 0.30 m s^{-1}. A stronger flow also exists on the Ellesmere Island side.
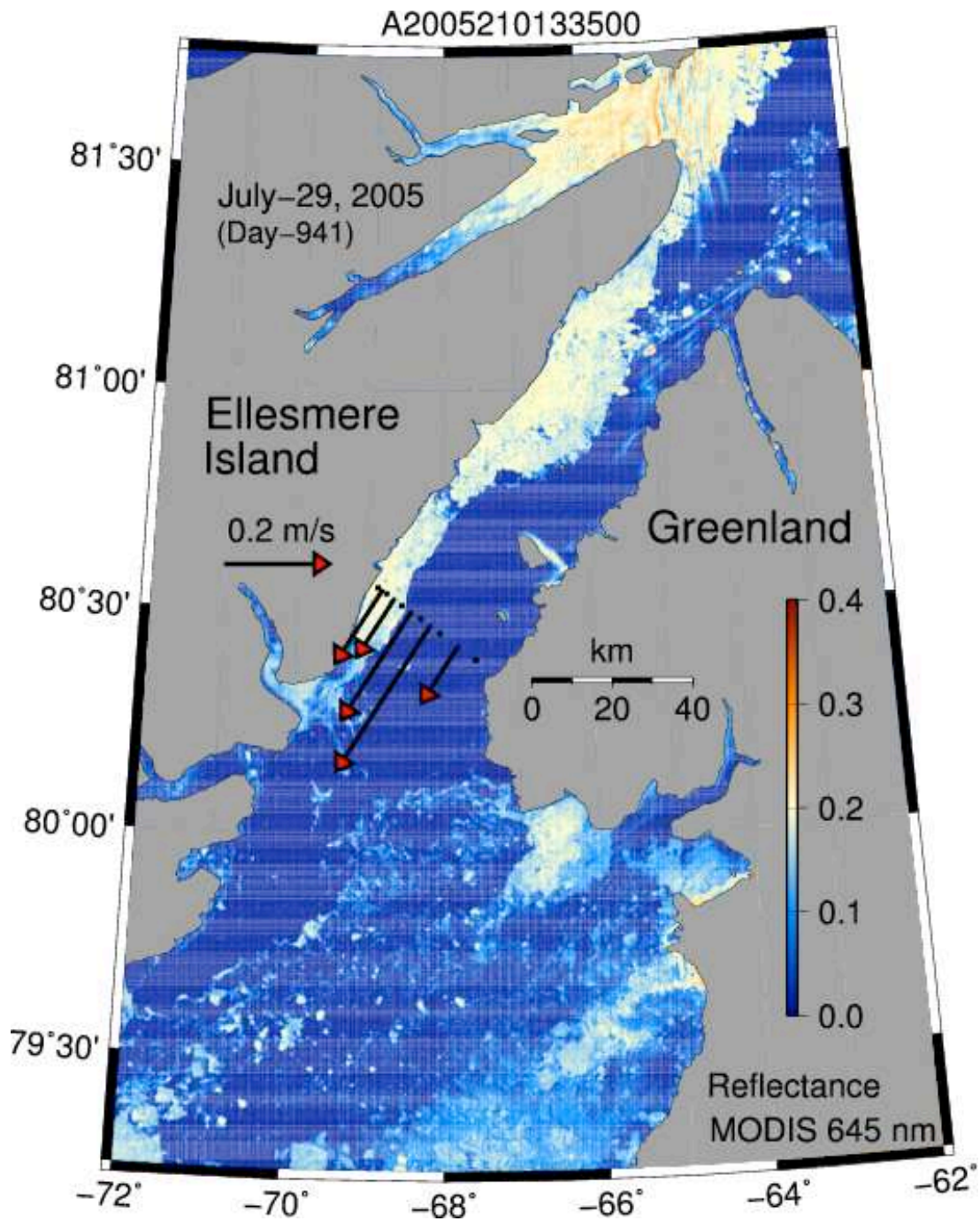
Figure 2.12: Modis image, 654 nm band, reflectance represents ice (yellow) and water (blue) for 29 July 2005 during strong event. Overlaid are vectors of geostrophic velocity in top layers during the strong event.
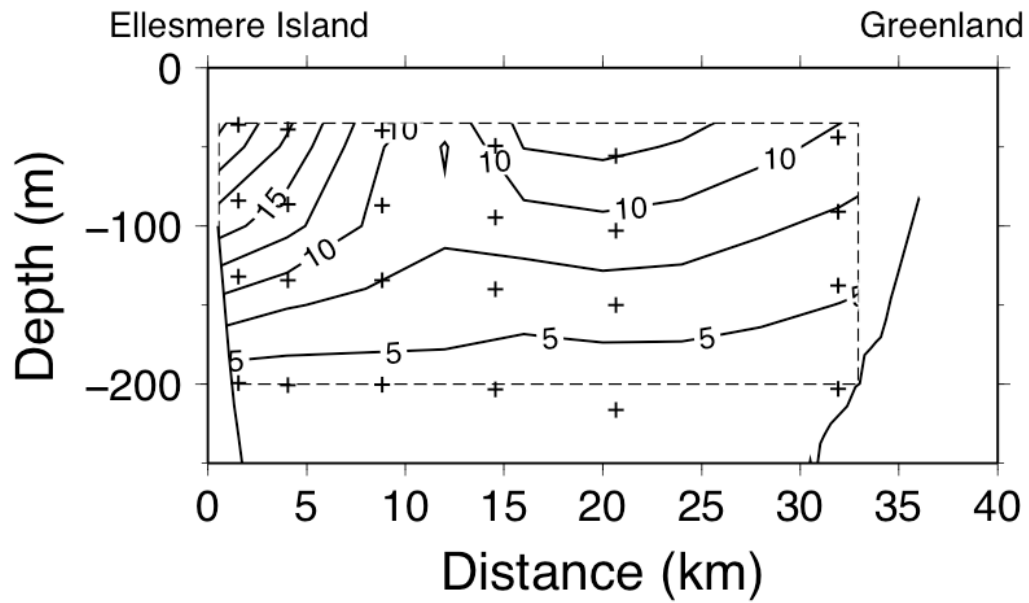
Figure 2.13: The three-year mean geostrophic velocity section in cm s^{-1}. Black crosses denote the instrument record-mean positions. Positive values denote flow to the south. A reference velocity of 0.04 m s^{-1} from the lateral and time-mean ADCP data is used as a level of known motion at 200 m. The surface-intensified flows on the Ellesmere Island side and in the middle of the strait are most pronounced with values of up to 0.20 and 0.14 m s^{-1} respectively.
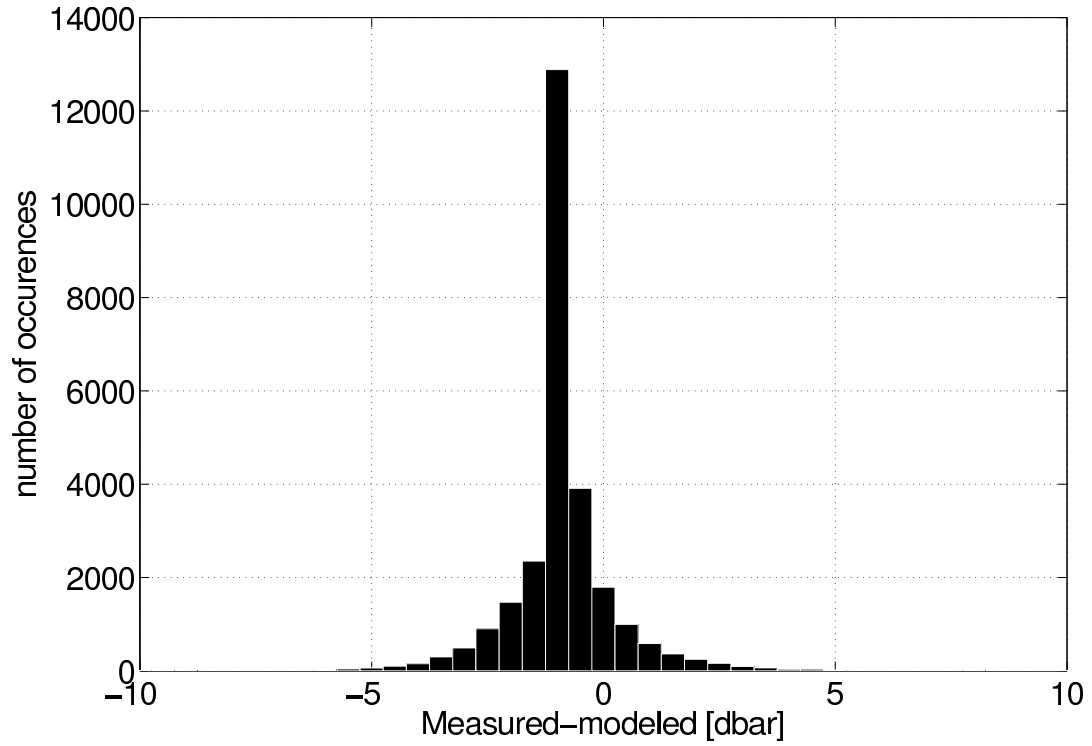
Figure 2.14: Pressure intercomparison between measured pressure at 80 m at KS03 and modeled pressure assuming linear behavior after mooring model results (Bell, 1979): histogram of measured minus modeled pressure shows a Gaussian distribution, that is, a linear interpolation explains the mooring behavior well.
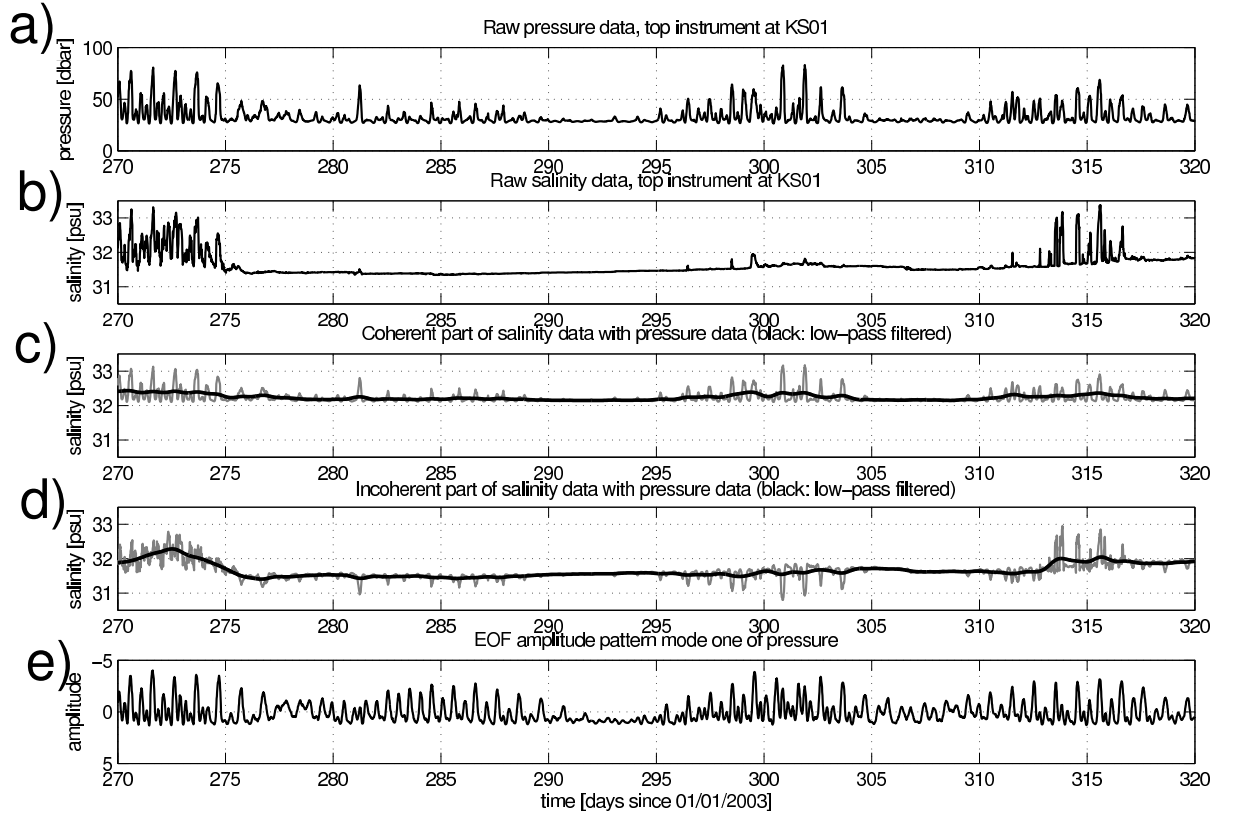
Figure 2.15: Evolution from raw pressure and salinity data to low-pass filtered pressure-incoherent salinity data that will be used for further analysis, as well as mode one amplitude of the pressure EOF analysis. All plots are shown for a sample 50-day time series: a) raw pressure data at top instrument at KS01 on Ellesmere Island side showing tidal variations, b) raw salinity data at top instrument at KS01 on Ellesmere Island side, including the mean, c) part of the salinity that is coherent with pressure in gray, d) part of the salinity that is incoherent with pressure in gray, e) amplitude of the first mode of the pressure EOF analysis, explaining 71% of the variance in the three-year pressure time series (the time series is non-dimensional and has a total variance of one). The black lines in plots c) and d) show the low-pass filtered salinity signal. The low-pass filtered incoherent part of the salinity (and temperature) will be used in the subsequent analysis.

49
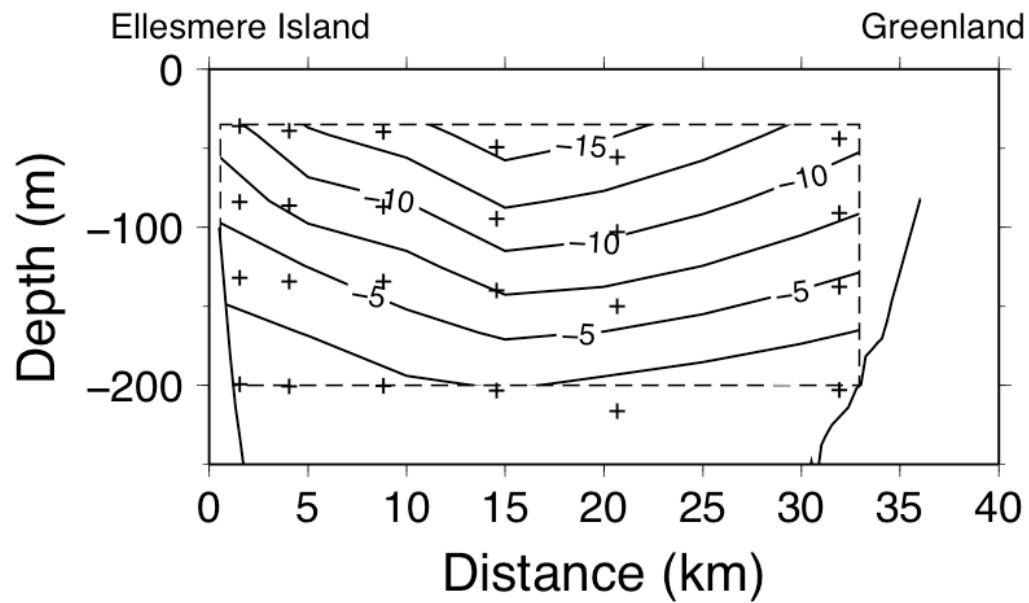
Figure 2.16: Spatial pattern of pressure EOF analysis, mode one, explaining 72% of the variance, in dbar, scaled by the factor that was used to achieve a variance of one in the time series. Black crosses denote the instrument record-mean positions. Highest variability of up to 17 dbar is observed at instruments in the top layers in the middle of the strait. Mooring motions are strongly correlated at all locations.

Chapter 3

GEOSTROPHIC OCEAN CURRENTS AND FRESHWATER FLUXES ACROSS THE CANADIAN POLAR SHELF VIA NARES STRAIT

3.1 Abstract

This study discusses geostrophic ocean currents and fluxes through Nares Strait, one of the major straits and connecting the Arctic to the North Atlantic across the Canadian polar shelf. Between 2003 and 2006 instruments were installed on sub-sea moorings to measure conductivity, temperature, pressure, and velocity at high temporal and spatial resolution across the 400 m deep strait. Here we present estimates of the variable volume and freshwater fluxes, derived by geostrophic calculation, through the fraction of the cross-section measured by the array. The array of conductivity-temperature recorders spanned 30 km of a 38 km wide section between 30 and 200 m depth, revealing geostrophic flow for a 23 km domain between these depths. This domain is 38% of the total cross-section and 58% of the cross-section above 200 m depth. We demonstrate the importance of the seasonal alternation between land-fast and mobile ice conditions, which has a strong influence on the structure of the geostrophic flow and the fluxes carried by it. The three-year mean geostrophic freshwater flux through the measured domain was 20 ± 3 mSv (relative to 34.8 psu) and no less than 26 mSv if extrapolated to the surface (excluding freshwater in moving ice). No trend over three years was detected, but the flux of freshwater through the measured domain was 30% larger when ice was moving than

51

when it was fast. Geostrophic volume flux through the measured domain was less strongly influenced by the state of the ice; its three-year mean was 0.47 ± 0.05 Sv, with a statistically significant increase by $15 \pm 4\%$ over this time. Geostrophic freshwater flux in Nares Strait was forced by both wind and along-channel pressure difference with mobile ice and by along-channel pressure difference only under land-fast ice. Geostrophic velocity is highly variable in space and time. An annual cycle in flow structure was observed, between a pattern with a surface jet in the center of the channel to another with a sub-surface maximum in velocity adjacent to Ellesmere Island. Strong freshwater incursions synchronous with wind forcing were observed during mobile ice seasons in the western half of the strait.

3.2 Introduction

The Arctic Ocean freshwater budget influences the global climate system. Studies of different components of the budget originated in the sixties by Timofeev (1960) and Mosby (1962) and continue until today (Aagaard and Carmack, 1989; Serreze et al., 2006; White et al., 2007). Important parts of the freshwater budget are the Pacific Water inflow through Bering Strait, Atlantic Water inflow through the Barents Sea and Fram Strait, continental river runoff, precipitation−evaporation, and outflow of liquid water and ice through Fram Strait and the Canadian Arctic Archipelago (CAA). Freshwater storage especially in the Beaufort Gyre means that the budget does not have to balance at any given time, rather pulses of freshwater release can occur during specific climate regimes (Proshutinsky et al., 2009). When freshwater is released from the Arctic Ocean towards the North Atlantic it can influence deepwater formation and therefore the Meridional Overturning Circulation (Lazier, 1980; Hakkinen, 1993; Hakkinen, 1999; Rennermalm et al., 2006; Stouffer et al., 2006; Wu et al., 2008).

Significant changes have recently been observed in the Arctic region including changes in sea ice drift pattern and upper ocean circulation (Polyakov and Johnson,

2000; Rigor et al., 2002), changes in Arctic sea ice cover (Lindsay and Zhang, 2005; Stroeve et al., 2005; Lindsay et al., 2009), a strengthening and warming of the Atlantic inflow through Fram Strait (Holliday et al., 2008), an increased run-off into the Eurasian sector (Peterson et al., 2002), and increased sea-ice outflow through Nares Strait (Kwok et al., 2010). All these changes can have an influence on the freshwater budget and its consequences; most changes appear to correlate with atmospheric forcing (Serreze and Francis, 2006).

To improve budget calculations and to investigate change, long-term measurements along all pathways are necessary. The CAA poses several challenges such as an ice-cover during up to eight months out of the year, closeness to the magnetic North Pole, and remote location (Melling, 2000). Analysis of observations in the CAA include data from Lancaster Sound, Barrow Strait, Cardigan Strait, Hells Gate, Wellington Channel, Hudson Strait, Nares Strait, and Davis Strait (Prinsenberg and Hamilton, 2005; Melling, 2004; Straneo and Saucier, 2008; Münchow et al., 2006; Münchow et al., 2007; Münchow and Melling, 2008; Cuny et al., 2005). This study focuses on Nares Strait, the north-eastern most strait in the CAA to the northwest of Greenland (Fig. 3.1) where Sadler (1976) deployed current meters for 40 days, Bourke et al. (1989) investigated temperature and salinity during one summer season, and Münchow et al. (2006) evaluated data from two-day ADCP surveys. Between 2003 and 2006 moorings were deployed in Nares Strait to investigate variability from tidal to interannual time scales for the first time. Münchow and Melling (2008) published first results of vertically averaged current variability while Samelson and Barbour (2008) discussed results from the atmospheric modeling component. Rabe et al. (2010) investigated hydrography and the salinity field for those three years (see chapter 2).

While measurements of currents, winds, and hydrography are crucial to the understanding of the importance of the region, it is also essential to obtain reliable

53

flux estimates and to describe the time dependence of flows through Nares Strait. Flux estimates may be used to monitor change, and to constrain climate prediction models. Most currently used climate models do not allow any flow of water through the channels of the CAA. Accommodating Arctic outflows on both sides of Greenland improves model performance (Holland et al., 2007). Fluxes through Nares Strait also reflect impacts of diminishing sea ice in the Arctic (Parkinson and Cavalieri, 2008), disintegrating ice shelves in northern Canada (Copland et al., 2007), and potentially surging glaciers and ice loss from the ice sheet in northern Greenland (Rignot and Steffen, 2008; Khan et al., 2010), especially influencing freshwater content.

Nares Strait is important for liquid freshwater flux (ice is land-locked for parts of the year). The strait facilitates a total southward volume flux estimated to be 0.7 Sv (Sv = 10^6 m^3 s^{-1}) (Sadler, 1976), 0.8 ± 0.3 Sv (Münchow et al., 2006), and 0.57 ± 0.09 Sv (Münchow and Melling, 2008). This compares to a net yearly southward volume transport in Fram Strait of 2 ± 2 to 4 ± 2 Sv (Schauer et al., 2004). Both straits are comparable for freshwater flux with Fram Strait exporting more freshwater in solid form and Nares Strait exporting more freshwater in liquid form.

Ice conditions in Nares Strait change between two states. Between June/August and November/March multi-year ice is drifting through the strait while during the remainder of the year ice is land-fast (hereafter called fast-ice). An ice bridge forms in Smith Sound anytime between November and March blocking ice advection (Dunbar, 1973; Barber et al., 2001; Kwok, 2005; Dumont et al., 2009; Kwok et al., 2010). Ice bridges are anchored to the coasts of both Greenland and Canada and tidal currents as well as local winds impact their formation (Samelson et al., 2006; Dumont et al., 2009). An ice index as used in Rabe et al. (2010) and defined by Münchow and Melling (2008) distinguishes between the two ice states in

Nares Strait. Table 3.1 lists approximate dates of transition and lengths of three fast-ice and four mobile ice seasons from 2003–2006.

This study extends the analysis of Münchow and Melling (2008) and Rabe et al. (2010) with time-dependent and vertical structure analysis in space and time of temperature, conductivity, velocity and pressure records (section 3.3). The year-round presence of ice and icebergs poses a constant threat to all moored equipment in these waters. A unique mooring design calls for unique data processing. Therefore we discuss calibration and a multiple linear regression model in detail in section 3.3 and the Appendices (3.8). Section 3.4 then describes variability of salinity and geostrophic currents on different sub-tidal time scales. Geostrophic volume and freshwater fluxes are described in section 3.5. Different forcing mechanisms—local wind and along-channel pressure difference forcing—will be discussed in section 3.6. Section 3.7 will discuss and conclude the results from this study.

3.3   Study Area and Data

The CAA consists of a network of straits and basins that connects the Arctic Ocean to the North Atlantic. These pathways are an important part of the Arctic Ocean freshwater budget. Nares Strait between Ellesmere Island (Canada) and north-west Greenland is about 38 km wide and 400 m deep. This study focusses on Nares Strait.

A mooring array consisting of Conductivity-Temperature (CT) strings (each with instruments at 30, 80, 130 and 200 m depth) and bottom-mounted 75-kHz ADCPs including one CT instrument was deployed in 2003 at 80.5°N, about 50 km north of the 230 m deep sill in Smith Sound (Fig. 3.1). The CT moorings were spaced about five km apart (Table 3.2). Fig. 3.2 shows the nominal position of all instruments within the cross-section. Naming convention starts with KS01 on the Ellesmere Island side going to KS14 on the Greenland side. KS02 will refer to the location of geostrophic velocity estimated from data collected at KS01 and KS03 while

KS10 refers to the same estimated from data at KS09 and KS13. Bottom-mounted mooring locations are indicated as KS02a, KS10a, etc. Two bottom pressure sensors were deployed in sheltered coastal water in Foulke and Alexandra Fjord off Greenland and Ellesmere Island, respectively, about 100 km to the south. Details of the CT and ADCP moorings are described in Rabe et al. (2010) and Münchow and Melling (2008). Overall 28 CT instruments were recovered in 2006 with gap-free three-year records. Appendix A (3.8.1) details potential sensor drift.

Our CT mooring strings have little buoyancy in the top 200 m in order to move downward during strong (tidal) currents to avoid snagging by ice. We take advantage of this vertical mooring motion at tidal time scales to increase the vertical resolution of our sub-tidal salinity and density fields. Appendix B (3.8.2) details a multiple regression model of mooring motions. The low-pass filtered salinity is used for geostrophic velocity calculation with a level of known motion at 200 m from ADCP site KS10a for all locations, representative for velocities at this depth across the whole strait. Fig. 3.3 displays the two-day low-pass filtered three-year ADCP velocity time series.

Three-year along-channel pressure difference time series were estimated by Münchow and Melling (2008) from two bottom pressure recorders on Smith Sound at the southern entrance of Nares Strait and one at Alert 300 km at the northern entrance. Atmospheric pressure systems impact both along-channel pressure difference and local wind. No direct wind observations exist from the period 2003–2006. Hence we use modeled wind (Samelson and Barbour, 2008) to estimate local wind stress forcing.

3.4 Salinity and Geostrophic Current Variability on Sub-Tidal Time Scales

3.4.1 Interannual Variability

3.4.1.1 Salinity

Fig. 3.4 shows salinity variability at KS01, close to Ellesmere Island. During the three-year deployment all mobile ice seasons illustrate salinity fluctuations with depth and time. During the 2003 mobile ice season freshwater incursions lasting around a week lowered salinity to less than 32 psu down to a depth of 100 m on seven occasions. In the 2004 mobile ice season salinities of less than 33 psu only reach a depth of 80 m on nine occasions. The same is true for the 2005 mobile ice season. Especially between December 2003 and February 2004 freshwater incursions reach a depth of 180 m three times with salinities of 33.5 psu in comparison to 34.25 psu the rest of the year.

During fast-ice seasons variability is reduced from the mobile ice seasons with almost no variability with depth. The 33 psu isohaline deepens by 50 m only in January 2005 and February 2006. Salinities during fast-ice seasons range from 32.5 to 34.25 psu with no visible freshwater incursions while during mobile ice seasons minimum salinities reach 30.2 psu in the top layers. From 2003 to 2006 a general freshening occurs at depth, deepening the 34.0 psu isohaline from 150 m to 180 m. During mobile ice seasons the surface layer is fresher than during fast-ice seasons due to ice melt, glacial runoff, and fresher water advected from the Arctic Ocean. These factors all enhance vertical stratification during mobile ice seasons.

Fig. 3.5 shows along-channel winds, which we use to demonstrate the connection between freshwater incursions during mobile ice seasons and wind events. Two particularly strong southward wind events with velocities of up to 20 m s^{-1} occur in January 2004. They coincide with freshwater incursions reaching down to 180 m at KS01. The second wind event lasts two weeks leading to the extended freshwater

core from the surface to 180 m. Peaks in wind in October 2003, November 2004, and December 2005 are all followed by similar freshwater incursions during mobile ice seasons.

The first mobile ice season lasts until March 2004 and coincides with consistent strong winds to the south. The water column is exposed to wind throughout January and February; the mobile ice season is longer than in other years. We speculate that strong winds mix the freshwater into deeper layers and therefore deepen isohalines and isopycnals.

Salinity at KS03, about four km from Ellesmere Island, looks similar to salinity at KS01 (Fig. 3.6). During all mobile ice seasons freshwater incursions with slightly less fresh water than at KS01 occur. The same number of freshwater incursions occur reaching the same depth. Again, large winds cause fresher water to be advected into this region from the north. During fast-ice seasons variability is much reduced in comparison to mobile ice seasons. In the 2003/04 fast-ice season the 33 psu isohaline deepens from 30 to 70 m. In the 2004/05 and 2005/06 fast-ice season the 33 psu isohaline drops by almost 50 m once in each season.

KS05 is located nine km from Ellesmere Island and shows less pronounced features in salinity than the two locations closer to Ellesmere Island (Fig. 3.7). During mobile ice seasons minimum salinities are higher and freshwater events therefore show a smaller vertical salinity gradient. The freshwater incursion in January 2003 still reaches a depth of 180 m but the two-week long fresher conditions are much less prominent. The freshwater incursion in the 2005 mobile ice season in December 2005 shows a similar magnitude than salinity at KS03. Fast-ice seasons show a freshening in the top layers in the 2003/04 fast-ice season (form 32.75 to 32.25 psu). The 2004/05 fast-ice season shows a much reduced event in January 2005. In contrast the third 2005/06 fast-ice season indicates fresher conditions throughout this whole season than at KS03 by almost 0.25 psu.

At KS07 in the middle of the strait we find a differently modulated dependence of the salinity field on ice states (Fig. 3.8). Water with salinities of less than 32 psu occur between 30 and 50 m during the early phase of the 2003 mobile ice season. In January 2004 saltier water (33 psu) reaches 30 m, the only time during the three years, which coincides with persistent southward winds of 12 m s^{-1}. During the 2004 mobile ice season the 32 psu isohaline is constant at 40 m until conditions change in November and December 2004 by 0.5 psu towards saltier waters. The 34 psu isohaline shoals, decreasing from 150 to 130 m during the fast-ice season in 2005, representing a trend towards saltier waters at depth. During the 2005/06 fast-ice season the 34 psu isohaline is constant at 130 m. Two freshwater incursions lowering salinity by 0.5 psu occur during this time period at 100 m. Water masses at 150 m vary between 34.5 psu and 33.25 psu. During the 2005/06 fast-ice season salinity varies at higher frequencies than during the two previous fast-ice seasons.

At KS09, 21 km from Ellesmere Island in the middle of the strait, the 2003 mobile ice season is similar to KS07 except for January/February 2004 when more persistent high salinities occur in the surface layer (Fig. 3.9). During the 2004 mobile ice season the fresher layer with less than 33 psu shallows (65 instead of 80 m). Strong freshwater incursions during the 2005 mobile ice season happen in December 2005. They do not reach as deep but are fresher. The 2003/04 fast-ice season is fresher by almost 0.5 psu in comparison to KS07. The 2004/05 fast-ice season is similar to KS07 except the second half shows a fresher top layer. The 2005/06 fast-ice season again shows a fresher top layer. The 32 psu isohaline drops by 30 m in April 2006.

The top 50 m of KS13, which is located in the eastern part of the strait off Greenland with a larger distance to KS09 than between other strings, are fresher than 32 psu during the first mobile ice season until November 2003 (Fig. 3.10). Between November 2003 and February 2004 strong salinity changes occur. Saltier

water upwells from 150 m to 30 m as surface salinity changes from 31.5 to 34.2 psu. These upwelling events are linked to the strong southward wind (Fig. 3.5).

There is more variability in salinity with time and depth during the fast-ice seasons at KS13 than there is in the middle and western part of the strait. During the 2005/06 fast-ice season in February 2006 water at 30 m becomes saltier by 0.5 psu when southward winds exceed 15 m s^{-1}. The surface salinity is comparable between the two ice seasons except for the fresher waters at the beginning of the record in the top layers and the salty waters during events between November 2003 and February 2004 throughout the full water column. These events coincide with strong southward winds during this time period (Samelson and Barbour, 2008), which is dynamically consistent with the upwelling off Greenland.

The two different ice seasons each year lead to different characteristics in salinity. During mobile ice seasons, when the strait is more exposed to local wind forcing, strong downwelling favorable winds on the western side of the strait (up to 20 m s^{-1}) cause fresher water to be advected into the strait from the north. During such an event we find fresher water down to a depth of 180 m in the western part of the strait due to downwelling. The same winds that cause downwelling off Ellesmere Island cause upwelling off Greenland. Downwelling events on the western side give an indication of the water mass characteristics in the top 30 m. Large wind speeds to the south lead to upwelling in the eastern part of the strait during mobile ice seasons. Fast-ice seasons remove the local wind as a forcing.

3.4.1.2 Geostrophic Velocity

Fig. 3.11 shows geostrophic velocities estimated at KS02, KS08, and KS10 with along-channel wind and the ice index. A 30-day low-pass filter applied to the data illuminates changes over the three years. Close to Ellesmere Island a sub-surface core of geostrophic velocities intensifies over the years, deepens, and is most pronounced during fast-ice seasons. Two anomalies with northward geostrophic flow

occur in November/December 2003 between 80 and 150 m. At KS08 in the middle of the strait a surface-intensified core exists during mobile ice seasons when the flow is geostrophic flow is weak at KS02. Strongest geostrophic velocities of up to 0.48 m s^{-1} occur in January 2003 and coincide with maximum southward wind. Reduced geostrophic velocities occur in the second year and intensify in the third year. Geostrophic velocity variability at KS10 is reduced in comparison to the other two locations. Two surface-intensified events occur in January 2004 and December 2005 linked to stronger wind speeds. At other times geostrophic velocities are more steady at KS10 and KS08.

The 30-day low-pass filter emphasizes variability at monthly to interannual time scales. Hence, we find that traditional ways to present seasonality as monthly means and annual cycles does not describe the variability in Nares Strait well. Instead, all seasonality relates to the presence of either fast-ice or mobile ice that we define as winter and summer seasons, respectively.

At KS02 close to Ellesmere Island all fast-ice seasons illustrate much stronger more consistent southward geostrophic flows (two-day low-pass filtered) than during the mobile ice season (Fig. 3.12). A subsurface maximum exists with up to 0.30 m s^{-1} in the 2003/04 fast-ice season, up to 0.35 m s^{-1} in the 2004/05 fast-ice season, and reaches maximum geostrophic velocities during the 2005/06 fast-ice season of up to 0.50 m s^{-1}. The core reaches from 30 m to a depth of 130 m during the 2005/06 fast-ice season. The magnitude of the geostrophic flow increases over the three years during fast-ice seasons and its position is consistent with the sub-surface geostrophic velocity core during fast-ice seasons close to Ellesmere Island described by Rabe et al. (2010).

During the mobile ice seasons the geostrophic flow is dominated by southward geostrophic velocities of 0.05 to 0.25 m s^{-1} concentrated in the top 80 m. The 2005 mobile ice season shows an increase in magnitude of the geostrophic velocity as

maximum values reach 0.55 m s^{-1}). During the 2003 mobile ice season switching bands of north and southward flowing geostrophic currents occur lasting one to six days each. One anomalous maximum southward geostrophic flow of 0.95 m s^{-1} exists as well as frequent northward geostrophic flow. During the 2004 mobile ice season the geostrophic flow is to the north on 12 occasions of comparable magnitude; only 8 shorter-lived northward geostrophic currents occur in the 2005 mobile ice season.

Variability in geostrophic velocity at KS04, about seven km from Ellesmere Island, looks drastically different for both ice stages in comparison to KS02 (Fig. 3.13). Less high frequency variability occurs, one strong southward geostrophic flow occurs, only few northward geostrophic velocities occur, during fast-ice seasons geostrophic velocity reduces over time. During fast-ice conditions the magnitude of geostrophic velocity decreases over the three years and the geostrophic velocity core deepens from 50 to 100 m. Maximum values in the 2003/04 fast-ice season reach 0.15 m s^{-1}. In the following two seasons they only reach 0.10 m s^{-1} (except for January 2005). The core is more persistent in the 2003/04 fast-ice season, in the 2004/05 fast-ice season is only persistent in the second half from March to June 2005. The 2005/06 fast-ice season has much reduced geostrophic velocities in the top 50 m with northward geostrophic velocities once.

During the mobile ice seasons the largest geostrophic velocities are associated with large wind. The 2003 mobile ice season shows maximum geostrophic velocities of up to 0.91 m s^{-1} around January 2004 (strong southward pulse in wind at that time). 17 times the geostrophic velocities switch to northward flow. In the 2004 mobile ice season the geostrophic velocity is more consistent to the south with one strong northward event in November 2004. Geostrophic velocities are much reduced in the 2005 mobile ice season in comparison to KS02 with no surface-intensified maximum geostrophic velocities.

Geostrophic velocities about 10 km from Ellesmere Island at KS06 demonstrate less temporal variability in comparison to geostrophic velocities close to the coast (Fig. 3.14). Fast-ice seasons have geostrophic velocities consistent at 0.10 m s^{-1}, much reduced from geostrophic velocities at KS02. The 2005/06 fast-ice season shows sub-surface southward geostrophic flow centered at 130 m and northward geostrophic velocities on six occasions in the 30 to 60 m layer.

During the 2003 mobile ice season seven southward pulses with around 0.40 m s^{-1} and a maximum of 0.85 m s^{-1} in January 2004 occur. The geostrophic velocity is to the north only twice. The following two mobile ice seasons present surface-intensified geostrophic velocities between 30 and 50 m. This location indicates an influence from wind as for example in January 2004.

Moving further towards the center of the channel, we demonstrate with Fig. 3.15 that geostrophic velocity for KS08, 17 km from Ellesmere Island, are around 0.05 m s^{-1} with sub-surface cores of 0.15 m s^{-1} at 50 m during fast-ice seasons. During the 2005/06 fast-ice season one strong southward geostrophic flow with velocities of up to 0.40 m s^{-1} occurs between 30 and 130 m in February 2006. During the 2003/04 and 2004/05 fast-ice seasons northward geostrophic velocities exist three and six times respectively.

Intermittent surface-intensified geostrophic velocities for the 2003 mobile ice season were between 30 and 100 m with maxima reaching 0.80 m s^{-1}. The 2004 mobile ice season has shallower geostrophic velocity cores only down to 80 m with 0.30 m s^{-1}, while the 2005 mobile ice season demonstrates an intensified geostrophic flow down to 100 m with maximum geostrophic velocities of 0.50 m s^{-1}. Over the three years the geostrophic velocities during mobile ice seasons decrease during the second year, and then intensify almost to the first year's strength again. The period around October 2004 has maximum geostrophic velocities in the top 30 m, followed by a northward geostrophic flow and a period of low geostrophic velocities

(0.05 m s^{-1}) until December 2004. The geostrophic flow is to the north only three times in the first 2003 mobile ice season, twice in the second, and once in the 2005 mobile ice season. Maximum geostrophic velocities exist during mobile ice seasons, consistent with channel-flow dynamics during this ice-free season with maximum geostrophic velocities in the middle of the channel.

At KS10 in the eastern half of the strait geostrophic velocities fluctuate between 0.02 m s^{-1} and 0.10 m s^{-1} during fast-ice seasons (Fig. 3.16). Geostrophic velocities are close to 0.05 m s^{-1} below 120 m; less than on the western side of the strait. In the 2005/06 fast-ice season one strong southward geostrophic flow event in February 2006 reaches down to 100 m with geostrophic velocities of up to 0.55 m s^{-1}. Northward geostrophic flow occurs once during the 2003/04 fast-ice season, ten times during the second, and three times in the 2005/06 fast-ice season influencing the whole water column.

During the 2003 mobile ice season a surface-intensified southward geostrophic flow reaches 0.60 m s^{-1} in January 2004 and exceeds 0.10 m s^{-1} down to 80 m nine times. Geostrophic velocities display northward geostrophic flows four times with 0.10 m s^{-1} in the full water column from 30 to 200 m. During the 2004 mobile ice season no strong southward geostrophic flows occur and the geostrophic flow reverses only once. In the 2005 mobile ice season, intensified southward geostrophic velocities occur in the top 50 m with geostrophic velocities of 0.25 m s^{-1} and a maximum of 0.50 m s^{-1}. This season reveals northward geostrophic flow influencing the full water column from 30 to 200 m twice. Over the three years geostrophic velocity events are reduced in magnitude from the middle of the strait.

3.4.2 Changes in Salinity and Geostrophic Velocity Over Time

Salinity and geostrophic velocity records contain statistically significant linear trends with time indicating temporal variability at scales longer than three years. Appendix A (3.8.1) explains that the trends represent a physical change in salinity,

temperature, and geostrophic velocity patterns in Nares Strait, because sensor drift is smaller than 0.07 psu over the three years towards fresher conditions.

3.4.2.1 Salinity

Fig. 3.17a shows interannual trends in salinity that are listed in Table 3.3. Surface waters off Ellesmere Island become saltier by 0.157 ± 0.010 psu year^{-1} at 50 m from 2003 to 2006. In contrast, waters at the same location below 120 m depth become fresher by -0.056 ± 0.004 psu year^{-1} at 150 m for the same time period. Salinity changes by -0.009 ± 0.004 psu year^{-1} at 150 m at KS03. Hence locations adjacent to Ellesmere Island become fresher at depth. KS01 freshens faster than KS03. This drift is both larger in magnitude and opposite in sign to the sensor drift and therefore a real signal. The trends between 120 and 200 m in the middle and the eastern side of the strait are close to zero. Salinity decreases in the top layers (30 to 100 m) on the eastern side by about -0.048 ± 0.008 psu year^{-1} at KS13 extending to about 15 km of Greenland.

The sectionally averaged temporal salinity change is $+0.018 \pm 0.003$ psu year^{-1} thus water becomes more salty overall. The strong increase in surface salinity off Ellesmere Island indicates less freshwater incursions during the last two years. Surface waters off Ellesmere Island become saltier and thus denser. In contrast deeper layers become fresher and therefore less dense off Ellesmere Island. Hence the water column in the western part of the strait becomes less stratified over time with smaller vertical density differences.

3.4.2.2 Geostrophic Velocity

Fig. 3.17b and Table 3.4 illustrate trends in the geostrophic velocity time series. A strong increase of about 0.092 ± 0.004 m s^{-1} year^{-1} at 50 m and 0.042 ± 0.002 m s^{-1} year^{-1} at 150 m occurs close to Ellesmere Island (KS02). The strongest increase happens in the shallowest layer. A small decrease of -0.042 ± 0.003 m s^{-1} year^{-1}

exists in the top layers in the middle of the strait down to 80 m (KS06). We observe no change in the lower layers and close to Greenland. The increase in geostrophic velocity close to Ellesmere Island relates to the different ways that salinity varies at KS01 and KS03 (Fig. 3.17a).

The largest increase of almost 0.1 m s^{-1} year^{-1} occurs in the top 100 m of the water column off Ellesmere Island where the freshest water resides and most of the freshwater outflow occurs. The sectionally averaged increase of geostrophic velocities is 0.009 $\pm$ 0.001 m s^{-1} year^{-1} and its influence on volume flux will be discussed section 3.7.

3.4.3 Interannual Variability of Seasonal Means of Geostrophic Velocity

This paper distinguishes between fast- and mobile ice seasons and observe changes in geostrophic velocity over the three years within these two seasons. Fig. 3.18 shows geostrophic velocity sections for each of the two different ice stages. The 2006 mobile ice season is cut short by mooring recovery early in the season.

During the 2003 mobile ice season a main shallow core close to the surface is observed in the middle of the strait with geostrophic velocities of 0.25 m s^{-1}. This core emerges from EOF analysis of salinity data (Rabe et al., 2010). In the 2004 mobile ice season, the geostrophic velocity in the core is reduced by 30% but returns to its first year's strength in the 2005 mobile ice season. The core is more confined to the middle of the strait (between km 12 and 25) whereas in the 2003 mobile ice season it stretches laterally (km 5 to 25). At the same time a second core with geostrophic velocities of 0.25 m s^{-1} appears on the Ellesmere Island side (also seen in 2006). This feature on the Ellesmere Island side is similar to fast-ice seasons, discussed next, although it has its maximum near the surface rather than at 40–60 m depth. Our data reveal a transition from a single jet in the center of the channel to an emerging coastal current adjacent to Ellesmere Island.

66

During fast-ice seasons an 0.18 m s^{-1} strong core exists within 7 km off Ellesmere Island at 40–60 m depth during the 2003/04 fast-ice season. During the 2004/05 fast-ice season geostrophic velocity increases to 0.22 m s^{-1} and resembles a more confined core to the eastern side. The 2005/06 fast-ice season demonstrates another increase to a maximum of 0.32 m s^{-1}, reaching from the surface down to 90 m and extending to km 3. The remainder of the strait shows uniform flow. The geostrophic velocity of the sub-surface core on the Ellesmere Island side increases and appears trapped adjacent to the Ellesmere Island coast during fast-ice seasons.

Seasonally averaged geostrophic flow change from year to year but increase off Ellesmere Island during all seasons. A second core occurs close to Ellesmere Island during mobile ice seasons 2005 and 2006.

3.5   Geostrophic Volume and Freshwater Fluxes

3.5.1   Definitions

With geostrophic velocity and salinity it is possible to calculate geostrophic volume and freshwater flux estimates. These do not include the top 30 m, nor freshwater carried in ice. The along- and across-channel directions are defined as x and y-coordinates, with u as the along-channel velocity (positive southward) and v the across-channel velocity (positive eastward).

Geostrophic volume flux is defined as:

$$q = \int_t \int_A u_g(y, z, t) dAdt \tag{3.1}$$

where $u_g(y, z, t)$ is the along-channel geostrophic velocity normal to area A in the (y, z) plane.

Geostrophic freshwater flux is defined as:

$$F = \int_t \int_A u_g(y, z, t)(1 - \frac{S(y, z, t)}{S_0})dAdt \tag{3.2}$$

67

where $S(y, z, t)$ is the salinity, and S_0 is a reference salinity of 34.8 psu representing the salinity of the Atlantic Ocean water flowing into the Arctic (Aagaard and Carmack, 1989). The part of the flux introduced by the level of known motion will be estimated and stated. The measured section is 58% of the total area above 200 m.

3.5.2 Ice Seasonally Mean Geostrophic Fluxes

Fig. 3.19 shows geostrophic volume and freshwater flux time series with the ice index overlaid. Geostrophic flux time series correlate with the ice index. During mobile ice seasons large geostrophic flux fluctuations occur in all years. The 2003 mobile ice season reveals the largest amplitudes and maximum geostrophic fluxes around January 14th 2004 (year day 379) during the three-year deployment. Maximum geostrophic volume fluxes reach 1.76 Sv, almost four times the mean geostrophic volume flux (discussed in section 3.5.3). The geostrophic freshwater flux reaches 92 mSv, also more than four times the mean geostrophic freshwater flux. This strong event is followed by geostrophic fluxes of opposite sign.

The 2004 mobile ice season depicts much reduced variability in comparison to the 2003 mobile ice season while the 2005 mobile ice season is similar to the first mobile ice season but with smaller extreme values. During all fast-ice seasons variability is smaller in comparison to the mobile ice seasons. Geostrophic fluxes are more constant from year to year. Geostrophic velocities appear constant as no freshwater incursions exist during this time period as seen in Fig. 3.4.

The seasonal means and uncertainties for each ice season for each year are listed in Table 3.5. Geostrophic freshwater fluxes have their largest values during mobile ice seasons. During mobile ice seasons geostrophic freshwater fluxes are increased by 30% relative to the fast-ice season. Geostrophic freshwater fluxes during mobile ice seasons reach 24 ± 7 mSv with the exception of the 2004 mobile ice season

68

(16 $\pm$ 5 mSv). During fast-ice seasons geostrophic freshwater fluxes vary between 17 $\pm$ 4 and 19 $\pm$ 4 mSv. Geostrophic freshwater flux is modulated by the ice seasons.

Geostrophic volume fluxes fluctuate by 20% during both ice seasons with no distinction from mobile to fast-ice seasons. The minimum occurs during the mobile ice season in 2004 with 0.38 $\pm$ 0.11 Sv and the maximum during the mobile ice season in 2006 with 0.57 $\pm$ 0.19 Sv. The largest uncertainties of 0.19 Sv occur during the 2003 and 2006 mobile ice seasons.

3.5.3   Three-Year Mean Geostrophic Fluxes

Integrating the geostrophic velocity over the section between 30 and 200 m depth and between KS02 and KS10, we calculate the three-year mean geostrophic volume flux to be 0.47 $\pm$ 0.05 Sv, which is equivalent to 15 $\pm$ 2 x 10^3 km^3 year^{-1}. The horizontal and vertical domain of the integral accounts for 58% of the cross-sectional area above 200 m. Note that 0.19 Sv or about 40% of this geostrophic volume flux is introduced by the reference velocity from the ADCP data at 200 m.

Earlier volume flux estimates include Sadler (1976) who calculated a volume flux of 0.7 Sv derived from a 40-day series of current measurements; Münchow and Melling (2008) calculated 0.57 $\pm$ 0.09 Sv from three-year mean ADCP mooring data using the full cross-section. Münchow et al. (2006) found 0.8 $\pm$ 0.3 Sv from a synoptic two-day ADCP survey. Comparing our data for this snapshot, we estimate the geostrophic volume flux from this study during the two-day period of August 6–8 at the beginning of our record which is 0.33 $\pm$0.08 Sv. Estimates from short-term surveys by Münchow et al. (2006) during that time thus represent a short-term pulse in volume flux at that specific time. The estimate is also not representative for the conditions on a monthly time scale. We thus emphasize the importance of long-term measurements to reveal the inherent temporal variability in fluxes that cannot be placed into context by instantaneous measurements alone.

We calculate a mean geostrophic freshwater flux for the same domain by taking the time mean of the freshwater flux time series (equation 3.2). The three-hour geostrophic velocity $u_g(y, z, t)$ is multiplied by the three-hour salinity anomaly $F_a(y, z, t)$: $< u_g(y, z, t) * F_a(y, z, t) >$ with $< . > = \int_{t_0}^{t_0+\Delta t} . \, dt$ and $\Delta t = 3$ hours before taking the spatial and then the temporal mean. The result is 20 ± 3 mSv or 630 ± 95 km^3 year^{-1} using a reference salinity S_0 of 34.8 psu. The reference velocity at 200 m accounts for 7 mSv or 35% of the total geostrophic freshwater flux (calculated by multiplying the three-hour reference velocity with the three-hour salinity anomaly at each three-hour time step, $< u_{ref}(y, z, t) * F_a(y, z, t) >$, then taking the spatial and the time mean). Therefore 13 mSv are associated with the baroclinic component of the freshwater flux. The measured section is again 58% of the total area above 200 m. For the freshwater flux the missing top 30 m are more crucial than for the volume flux as a large fraction of fresher water occurs in that layer (Fig. 3.4; (Melling, 2000)). Our estimate thus provides a lower bound since we have no data from the top 30 m.

When calculating the geostrophic freshwater flux from the product of the three-year mean of geostrophic velocity $< u_g(y, z, t) >$ and salinity anomaly $< F_a(y, z, t) >$ using $< . > = \int_{t_0}^{t_0+\Delta t} . \, dt$ with $\Delta t = 3$ years, the geostrophic freshwater flux is 20 mSv. Therefore the freshwater flux occurs at low frequencies and the covariance of shorter time scales (daily to seasonal)—relating to fluctuations in geostrophic velocity and freshwater anomaly—adds up to zero.

Münchow et al. (2007) calculated 22 ± 9 mSv excluding the top 30 m (or 28 ± 12 mSv including the top 30 m) for the freshwater flux for a section across Nares Strait from ship-based ADCP surveys based on short-term observations. These synoptic snapshots were made during a peak in the mobile ice season (Fig. 3.19b).

Fig. 3.19 place prior flux estimates from short-term measurements into a larger temporal context. Variability—especially during the mobile ice season—is

enhanced. Short-term measurements thus are always biased by strong events at weekly and seasonal time scales.

3.5.4 Geostrophic Freshwater Flux Extrapolation to the Surface

We estimate the geostrophic freshwater flux in the top 30 m making the assumption that during mobile ice seasons there is no shear in geostrophic velocity between 30 m and the surface, that is, $u_g(z = 0) = u_g(z = 30 \text{ m})$. In contrast, during fast-ice seasons we assume a linear shear towards $u_g(z = 0) = 0$ due to the ice cover. Salinity within the top 30 m is assumed to be $S(z = 0) = S(z = 30 \text{ m})$. These assumptions allow us to provide a rough estimate for flux contributions from this generally unresolved surface layer.

Making these assumptions, we find during the mobile ice season an additional 12 mSv of geostrophic freshwater flux. During the fast-ice season an additional 1 mSv would contribute to the geostrophic freshwater flux. These preliminary calculations indicate that the geostrophic freshwater flux during mobile ice season, when fresh water exists in the top 30 m, is potentially important. Since mobile ice seasons cover 41% of the time, the three-year mean geostrophic freshwater flux estimate can be adjusted to 26 mSv. The top 30 m thus contribute more than 25% to the long-term mean geostrophic freshwater flux.

3.6 Forcing

3.6.1 Pressure Difference Forcing

An important factor for the flow through straits is the pressure difference along the strait (Garrett and Toulany, 1982). Kliem and Greenberg (2003) show with numerical simulations that an increase in elevation in Baffin Bay relative to the Arctic Ocean results in a decrease in volume transport through the CAA, with Nares Strait being most sensitive. Münchow and Melling (2008) found that the along-channel pressure difference explains 60% of the variance at the 20-day period

with no phase lag for sectionally averaged flows. Fig. 3.20 shows the along-channel pressure difference time series from 2003 to 2006.

This paper evaluates data for both ice seasons in the frequency domain. Coherence squared is the degree of linear correlation between two signals as a function of frequency. We subdivide each time series into ten non-overlapping time series and then use the ensemble averages of the ten separate estimates. This increases the number of degrees of freedom, decreases uncertainty in estimated parameters, but reduces frequency resolution. We only focus on geostrophic freshwater fluxes since geostrophic volume and freshwater fluxes are highly correlated with a correlation coefficient of around 0.95 (details are explained in section 3.7).

Coherence squared, phase, and gain between the along-channel pressure difference and the geostrophic freshwater flux are plotted in Fig. 3.21 for mobile ice seasons. The coherence squared is significantly different from zero at all frequencies. The highest correlation occurs at 0.12 cycles per day (cpd) (8 days). Almost 40% of the variance in geostrophic freshwater flux is explained by the pressure difference at this weekly time scale. At other frequencies about 20% of the variance of the two time series are correlated. The phase for the peak at 8 days is around -10 degrees, which means that the along-channel pressure difference is leading the geostrophic freshwater flux by about one day. The gain is almost 160 x 10^3 Sv m^{-1} at weekly time scales, that is, a change in sea-level of 0.01 m results in a geostrophic freshwater flux change of 1.6 mSv. At higher frequencies the phase fluctuates between $+30$ degrees at 0.22 cpd (4.5 days), -30 degrees at 0.4 cpd (2.5 days), and $+15$ degrees at the highest frequencies with fluctuating lead/lag relationships; these large fluctuations relate to channel dynamics at different time scales.

Since the along-channel pressure difference also has an effect on the flow during fast-ice seasons, we calculate coherence squared, phase, and gain for the fast-ice seasons as well (Fig. 3.22). We exclude the first 2003/04 fast-ice season

from our analysis as it is much shorter and only focus on the two remaining fast-ice seasons. We average spectral results in the frequency domain over those two fast-ice seasons. During the two fast-ice seasons the coherence squared is above the 95% confidence level at frequencies below 0.15 cpd (6.7 days) meaning that coherence at higher frequencies cannot be distinguished from zero. The phase is zero at lowest frequencies and the along-channel pressure difference is therefore in-phase with the geostrophic freshwater flux. The gain varies between 50 and 100 x 10^3 Sv m^{-1} (0.5 to 1 mSv change per cm) with a higher gain the lower the frequency. The findings of geostrophic freshwater flux presented here are consistent with those presented by Münchow and Melling (2008) for sectionally averaged velocities.

3.6.2   Local Wind Forcing

The three-year mean along-channel wind speed in Nares Strait from the atmospheric model is plotted in Fig. 3.5; wind is towards the south with maximum values exceeding 15 m s^{-1} and at times towards the north with a maximum speed of 10 m s^{-1}. During fast-ice seasons, the local wind stress does not affect the channel flows. During mobile ice seasons, though, the wind acts as a local forcing agent. Münchow and Melling (2008) found no correlation between wind stress and the sectionally averaged ADCP currents using the entire three-year record which contains both seasons of moving and fast-ice. The period and timing for both ice stages change from year to year. We evaluate the coherence between the geostrophic freshwater flux and the local wind separately for mobile and fast-ice ice seasons.

In the frequency domain we calculate partial coherence squared, phase, and gain for mobile ice seasons from 2003 to 2005. Partial coherence is calculated using linear system analysis to only evaluate the component of the local wind that is not correlated with the along-channel pressure difference. The reason for this analysis is that local wind and the along-channel pressure difference are significantly correlated at times. To evaluate only the local wind effect, we will remove the part that is

73

correlated with the sea level height along the strait to distinguish between purely local and pressure difference forcing mechanisms.

The coherence squared during the mobile ice season is significantly different from zero at all frequencies lower than 0.37 cpd (2.7 days) (Fig. 3.23a). Maximum correlation occurs at a frequency of about 0.12 cpd (8 days) with around 40% of the variance explained. The phase is negative, i.e., local wind leads the geostrophic freshwater flux. A phase of -60 degrees at a frequency of 1/6 cpd indicates that the local wind leads geostrophic freshwater flux by one day. The gain fluctuates around 1×10^3 Sv/(m s^{-1}) at frequencies below 0.37 cpd (2.7 days).

The coherence squared between the local wind and the geostrophic freshwater flux during fast-ice seasons (Fig. 3.23a) is, as expected, below the 95% confidence level at all frequencies (light grey line). We regard wind and geostrophic freshwater to be uncorrelated. Phase and gain are therefore not shown as they have no meaning in this context.

Summarizing, we find local wind and geostrophic freshwater flux to be coherent at frequencies below 0.37 cpd (2.7 days) during mobile ice seasons with the local wind leading the geostrophic freshwater flux by approximately a day.

3.7 Conclusions and Discussion

This paper analyzes a three-year mooring data set from Nares Strait in the CAA and to the north-west of Greenland with a focus on CT data in combination with local wind, and along-channel pressure differences. These first long-term measurements at high spatial and temporal resolution are important for the evaluation of the Arctic freshwater budget. Recent changes in the Arctic can only be traced downstream if we establish a baseline for all regions first. This project in Nares Strait is a first step in that direction with an emphasis on establishing a baseline that can be used to obtain meaningful results.

A novel mooring CT string design (less buoyancy above 200 m leading to lean-over movements) developed for this project successfully solved one of the challenges in the CAA: iceberg encounter and ice-cover threat to instruments. With a multiple linear regression model a high resolution salinity data set was achieved.

This study focuses on sub-tidal variations in salinity and geostrophic velocity although ice, ocean, and atmosphere interact on different time scales in Nares Strait. The ice conditions are categorized into two seasons: mobile ice and land-fast ice. The two different ice states influence geostrophic freshwater flux, forcing, geostrophic velocity, and salinity.

The geostrophic freshwater flux (reference salinity of 34.8 psu) reveals larger variability and higher flux numbers by 30% during mobile ice seasons in comparison to fast-ice seasons. The three-year mean geostrophic freshwater flux is 20 ± 3 mSv excluding ice. This describes 58% of the cross-section above 200 m. The missing top 30 m of the water column are crucial and a first extrapolation leads to an additional 25% in geostrophic freshwater flux. This is still a lower bound since a constant salinity in the top 30 m was assumed even though salinity decreases towards the surface. Melling (2000) reviewed freshwater estimates from Prinsenberg and Bennett (1987) and found that up to 50% of the flux in summer occurs in the upper 10 m. In winter 50% of the flux is concentrated in the top 44 m. Our extrapolation suggests that the flux in the top 30 m is negligible during fast-ice winter seasons ($< 5\%$) but substantial during mobile ice summer seasons ($> 40\%$). The large variations on shorter time scales put values from the literature into context. No significant trend over the three years was observed in geostrophic freshwater flux. The implications of the modulated geostrophic freshwater flux by the ice cover could be important for the future. A transition towards a longer mobile ice season would lead to increased freshwater flux. The system would respond more strongly to time-dependent local and remote forcing and enhanced freshwater flux could lead to changes downstream.

In contrast to the freshwater flux, the geostrophic volume flux is not modulated by the ice cover; the three-year mean is 0.47 ± 0.05 Sv with a statistically significant $15\% \pm 4\%$ increase over the three years. Variability is large in geostrophic volume flux and comparisons to literature values reveal both seasonal weekly bias due to temporally varying ice cover and strong events, respectively.

The geostrophic freshwater and volume flux in Nares Strait are partially forced by along-channel local winds and pressure differences during the mobile ice season. At weekly time scales the combined variance during the mobile ice seasons from local wind and along-channel pressure difference forcing explains 80% of the variance. The along-channel pressure difference accounts for 35% of the variance while local winds account for 45%. This eight day fluctuation in geostrophic freshwater flux supports earlier observations of flow variability made in northern Baffin Bay by Melling et al. (2001). Fluctuations in the flow through Smith Sound are forced in part by the higher sea level of the Arctic Ocean and in part by winds channeled between the mountains of Greenland and Ellesmere Island. These fluctuations drive oscillations of five to ten day periods. During the fast-ice seasons 40% of the variance is explained at eight days with all variance from the along-channel pressure difference; local wind has no effect as the flow is decoupled from the atmosphere through the ice cover.

Geostrophic velocity shows large variability at monthly to interannual time scales while geostrophic freshwater flux shows large variability at weekly time scales. We conclude that traditional ways to present seasonality as monthly means and annual cycles does not describe the variability in Nares Strait well. Seasonality relates to the ice state and weekly flux estimates might be more meaningful for Nares Strait than monthly means.

Geostrophic volume and freshwater fluxes for the three years are highly correlated. For geostrophic freshwater flux we saw a change between mobile and fast-ice

seasons while the geostrophic volume flux stayed more constant. The correlation coefficient in the time domain is large during each season because fluctuation around the (different) means is correlated. The means per season in geostrophic volume and freshwater flux differ, but the fluctuations do not. Both fluxes are related to local wind and along-channel pressure difference depending on the state of the ice.

The seasonal mean interannual variability of geostrophic velocities shows a strengthening core in the middle of the strait and an additional core close to Ellesmere Island. The latter appears in the 2005 mobile ice season. During fast-ice seasons a sub-surface core close to Ellesmere Island exists which increases and condenses over the three years. A transition occurs from a single jet in the center of the channel to an emerging coastal current adjacent to Ellesmere Island over the three-year period.

Geostrophic velocities demonstrate large variability over time and a strong dependence on the ice cover. In the western part of the strait maximum geostrophic velocities occur during fast-ice seasons (increasing over the three years) with a sub-surface core. The middle of the strait presents maxima in the surface layer during mobile ice seasons. Much smaller geostrophic velocities exist close to Greenland during all ice seasons. During the mobile ice seasons reversing signs in geostrophic flow on short time scales can be observed throughout the strait.

Salinity plots show frequent freshwater incursions during mobile ice seasons and more steady conditions during fast-ice seasons. We identify up- and downwelling events on both sides of the strait.

Temporal variability at scales larger than three years from interannual trends of salinity and geostrophic velocity show a surface layer close to Ellesmere Island that becomes saltier over time and a bottom layer that becomes fresher off Ellesmere Island. Geostrophic velocities increase over the three years of our observations by up to 0.1 m s^{-1} year^{-1} in the top 100 m off Ellesmere Island. This locations not only

includes the part of the water column that contains most of the freshwater but it is also on the western side of the strait with the freshest water (Fig. 3.4). The increase in geostrophic velocity is offset by water masses getting saltier at this location over the three years therefore leading to no increase in geostrophic freshwater flux (trends in the geostrophic freshwater flux are not significant at the 95% confidence level). The sectionally averaged increase in geostrophic velocity from the three-year deployment leads to the statistically significant increase in geostrophic volume flux of 15% ± 4% but does not imply long-term change (Table 3.6). Münchow and Melling (2008) found a 20% ± 10% volume flux increase from ADCP data for the same time period.

The two ice states discussed in this paper depend on an ice bridge forming in Smith Sound. This ice bridge failed to form in 2006/07 (Münchow et al., 2007; Kwok et al., 2010), 2008/09, and 2009/10. These were the first recorded such occurrences perhaps indicating a transition to a different dynamic state. As we here demonstrated, a longer mobile ice season implies larger freshwater fluxes by up to 40%. Furthermore, such change also implies an extended period of thick ice streaming south. In combination such conditions increase total freshwater flux. We hypothesize that the dynamics of Nares Strait after August 2006 are in a state of transition as the season of land-fast ice cover diminishes. A continued data set in Nares Strait from 2007–09 will test, if the freshwater flux through the CAA is transitioning to the dynamic state that is characterized by mobile ice. This regime change to longer mobile ice seasons would cause more variability in ice and ocean motion. It would also cause a potential increase in freshwater flux since the system responds more strongly to time-dependent local atmospheric surface forcing in addition to remote forcing by the ambient Arctic Ocean and Baffin Bay. Changes in the duration of land-fast ice seasons impact vertical and horizontal stratification as well as the distribution, transit time, and pathways of Arctic freshwater.

An extension of this data set from 2007–2009 will investigate if the time-dependent changes in the strait continue. Data in Nares Strait for the analyzed three years, especially geostrophic flux numbers, are very variable between seasons, and are useful to put historical flux numbers into context. Nares Strait is a strongly changing environment related to ice conditions, local wind, and remote atmospheric forcing. Note that we only used geostrophic estimates here, a comparison between CT and ADCP data will evaluate the assumption that the flow in Nares Strait is geostrophic. The 2007–2009 data set with CT and ADCP instruments covering the same part of the strait will help with the analysis.

3.8 Appendices

3.8.1 Appendix A: Calibration

All instruments were factory calibrated by SeaBird Electronics prior to deployment. Discrepancies between true and measured salinity result predominantly from drift in conductivity, not temperature sensors. Typically, cell fouling biases conductivity sensor readings towards lower values. Cell fouling increases by about 0.05 psu per year in Arctic environments with maximum drifts of several tenths (from prior personal Arctic mooring experience). In the equatorial Pacific Ando et al. (2005) found maximum conductivity drifts of 0.010 (0.0053) S m^{-1} after a one-year deployment in the top layers (thermocline layer), which is equivalent to 0.065 (0.034) psu at 30°C in the very similar SBE37IM instruments. Freitag et al. (1999) also found conductivity drifts of the same magnitude in other similar SeaBird instruments.

Ando et al. (2005) found that the drift of the conductivity sensors in the shallower layers was caused by the environment, such as biofouling and scouring effects relative to current speed. Biofouling in Nares Strait is limited and even shallow moorings revealed little noticeable fouling after a three-year deployment.

To estimate an upper bound on conductivity drift we use data from CT instruments deployed two meters above the seafloor. At the ∼300 m deep locations water masses are stable with only small salinity variations (see Figs. 3.4 and 3.10). These instruments represent a worst case concerning sediments because of their vicinity to the seafloor.

Figs. 3.25a and b show histograms of bottom salinity at sites KS02a and KS10a. The histograms show the salinity values for the first and last three months of the record. Salinity shifted towards fresher conditions over the three years. A Gaussian normal distribution is shown for comparison in grey. This is a conservative estimate of error for the salinity data as it includes drift and signal.

Figs. 3.25c and d illustrate histograms of temperature at the same sites. The distribution is normal again with a shift towards lower temperatures by about 0.05 to 0.08°C over the three years. Temperature sensors are generally stable over time so we speculate that this drift is associated with a cooling of the water mass at the bottom of Nares Strait. The concurrent cooling and freshening of bottom waters in Nares Strait may in part relate to a change of bottom waters towards a fresher and cooler Pacific influence as opposed to the warmer and saltier Atlantic influence. Hence we conclude that drifts in salinity and geostrophic velocity above 200 m are dominated by real signals associated with changing water mass characteristics in Nares Strait and not associated with sensor drifts (Table 3.3).

When looking at T-S relations from bottom-mounted moorings at KS02 and KS10, the constant slope predicts how much salinity change corresponds to a temperature change since we assume temperature sensors to be stable (Fig. 3.24). The difference between salinity at the beginning and the end of the record at both locations indicates a change of 0.07 psu over the three years. Instantaneous CTD measurements in 2003 and 2006 are plotted at locations KS03 and KS11 in 2003, and KS10 in 2006, assuming that conditions at depth are representative across the

whole strait. The CTD data indicates a change of 0.03°C at both locations over the three years. Assuming that the temperature of the environment changed over the three years as seen in the histogram and explained above, the change in salinity would be associated with a sensor drift. The change of 0.07 psu towards fresher conditions is therefore related to cell fouling.

3.8.2   Appendix B: Multiple Linear Regression Model

Because the mooring strings are pulled down by current, as explained by Rabe et al. (2010), the depth of measurement is strongly modulated by tidal currents (many tens of meters), and less strongly by tide elevation (several meters). Therefore it was necessary to design an analysis method to remove tidal influence from the time series from each instrument that measured the water column from the moving strings.

Rabe et al. (2010) used linear system analysis to remove signals due to vertical mooring motions at coarse vertical resolution. For this paper we take advantage of the vertical sampling of the water column at tidal period to obtain a higher vertical resolution in salinity and temperature. A simple harmonic analysis is not possible since the measurements were not taken at a fixed point in space. To evaluate the tidal demodulation we developed a model for the temporal variation salinity using multiple linear regression based on least squares, e.g.,

$$S(p,t) = s + at + bp + cp^2 + d\sin(\frac{2\pi t}{\tau}) + e\cos(\frac{2\pi t}{\tau}) \qquad (3.3)$$

The six unknowns are a, b, c, d, e and s. The data are S for salinity, p for pressure, and t for time. The variable τ is chosen to represent the dominant period of variation, here the M_2 tide (12.42 hours). The six unknowns are to be determined by the method of least squares, solving the over-determined set of equation, one for each time of measurement (four per hour) by substituting data values into the

equation. The system is solved at selected times for each of the two depth ranges and the chosen time range (one day). The coefficients of fit were then used to interpolate to values at the depths of interest at the mid-time of the window. The processor advanced in three-hour steps to repeat the calculation.

The model is a simplified representation of the signal recorded by instruments dragged vertically through a salt stratified water column. It incorporates a quadratic dependence of background salinity on pressure, a possible linear change in background salinity with time (the same at all depth), and a sinusoidal variation of the salinity at the nominal semidiurnal period. The latter term represents the vertical movement of the sensor through the background field of salinity in response to the ebb and flood of the tide. This simple model of the signal is useful only for short windows in time; we used a window width of about two cycles of the semi-diurnal tide. The regression analysis provides coefficients that separately represent background and tidal effects. A de-tided field can then be generated simply by substituting values for depth and time using only those coefficients that represent the background field.

The equation represents a compromise between a full representation of the complexity of the signal and a practical regression model that was stable throughout the three-year period of measurement at all sites. The model ignores the diurnal tide. It assumes that the pull-down modulation of salinity is the same at all depths of measurement, even though the sensors higher on the mooring are pulled down a greater distance than those lower down, and even though the change in salinity via pull-down is dependent on the local vertical gradient of salinity. It separately fits the amplitude of the pull-down signal without cross-reference to the vertical gradient embodied in coefficients b and c.

The vertical dimension to the window spans three levels of measurements, namely 30–80–130 m and 80–130–200 m. We develop separate regression curves for

82

these depth windows and after evaluating the results chose a 100 m depth level to switch between regression coefficient one and two.

If the removal of the vertical variability is perfect, the sub-tidal salinity field will consist of the mean steady field and a residual field caused by the unresolved sub-tidal temporal and vertical variability. The aim is not to fit the data exactly at every measurement point, but rather to minimize some measure of the deviations of the approximating functions to the actual data values (Candela et al., 1992).

Statistics were used to evaluate the goodness of fit after reconstruction of the original data was complete. R^2 is close to 0.98 and small estimates of error variances around 0.02 indicates high levels of confidence in the regression model. The residuals varied mostly between $\pm$ 0.3 psu but were further reduced to less than 0.1 psu by a low-pass filter.

To reconstruct the data set without a tidal variation (taking out the internal tide) we used all regression coefficients except the sin and cos terms from equation 3.3. We reconstructed the data at one meter resolution. We thus constructed a $S = S(y, p, t)$ data set of salinity that minimizes the sampling bias introduced by mooring motions.

3.9   Acknowledgments

Table 3.1: Ice index: Start and end dates of each ice season including length in days for each season. Mobile ice refers to late summer, fall, early winter and fast-ice to late winter, spring, early summer depending on the ice index defined by Münchow and Melling (2008).

Season	Start date	End date	Length [days]
Mobile ice 2003	08/04/2003*	03/11/2004	220
Fast-ice 2003/04	03/11/2004	06/17/2004	97
Mobile ice 2004	06/17/2004	12/18/2004	184
Fast-ice 2004/05	12/18/2004	07/02/2005	196
Mobile ice 2005	07/02/2005	01/13/2006	195
Fast-ice 2005/06	01/13/2006	06/15/2006	153
Mobile ice 2006	06/15/2006	08/13/2006+	59

*: time of mooring deployment

+: time of mooring recovery

Table 3.2: Recovered instruments: Mooring name, type of mooring, location (Latitude, Longitude), record length [days], nominal depth [m] including pressure sensor depth on CT moorings.

Name	Type	Lat	Lon	record length	nom. depth
KS01	CT	80 33.470 N	68 54.456 W	1108	30* 80 130 200*
KS02a	CT	80 33.228 N	68 52.466 W	1103	302
KS03	CT	80 32.697 N	68 47.307 W	1104	29* 79* 129 199*[1]
KS05	CT	80 31.139 N	68 34.808 W	1104	27* 77 127 197*
KS07	CT	80 29.372 N	68 19.455 W	1105	32* 82 132 202*
KS09	CT	80 27.349 N	68 03.839 W	1104	38* 88 138 208*
KS10a	CT	80 26.326 N	67 55.779 W	1105	299
KS12a	CT	80 24.553 N	67 40.255 W	1104	263
KS13	CT	80 23.801 N	67 34.575 W	1106	32* 82 132 202*
KS14a	CT	80 23.305 N	67 26.751 W	1103	157
P1 Foulke	Pressure	78 18.000 N	72 34.200 W	1116	24
P2 Alexandra	Pressure	78 54.600 N	75 48.000 W	1099	23
P Alert	Pressure	82 29.512 N	62 19.038 W	ongoing	Height Above Chart Datum: 3 m

*: pressure sensor
1: pressure sensor malfunction after 500 days

Table 3.3: Salinity offset [psu] and trends [psu year^{-1}] with uncertainties; finding a linear trend for six positions across the strait at selected depth levels (50, 150 m, and sectionally average) and from bottom-mounted instruments after the mean has been removed. Uncertainties are using a significance test to get the 95% confidence intervals using the null hypothesis according to Fofonoff and Bryden (1975). Degrees of freedom (dof) and decorrelation time scales T_D in hours are listed as well.

Mooring	Depth	Offset [psu]	Trend [psu year^{-1}]	dof	T_D
Sec. ave.	all	-0.040 ± 0.006	0.018 ± 0.003	36	726
KS01	50	-0.331 ± 0.022	0.157 ± 0.010	29	909
KS03	50	-0.339 ± 0.018	0.161 ± 0.008	28	938
KS05	50	-0.222 ± 0.018	0.105 ± 0.008	29	888
KS07	50	-0.061 ± 0.015	0.029 ± 0.006	33	777
KS09	50	0.075 ± 0.014	-0.036 ± 0.006	47	549
KS13	50	0.100 ± 0.018	-0.048 ± 0.008	33	780
KS01	150	0.117 ± 0.009	-0.056 ± 0.004	93	282
KS03	150	0.018 ± 0.009	-0.009 ± 0.004	137	192
KS05	150	-0.033 ± 0.009	0.016 ± 0.004	68	381
KS07	150	-0.036 ± 0.009	0.017 ± 0.004	40	648
KS09	150	-0.025 ± 0.007	0.011 ± 0.003	36	711
KS13	150	-0.028 ± 0.009	0.013 ± 0.004	51	504
KS02a	302	0.0775 ± 0.0005	-0.0341 ± 0.0002	13	1929
KS10a	299	0.0626 ± 0.0007	-0.0258 ± 0.0002	18	1426
KS12a	263	0.0989 ± 0.0009	-0.0348 ± 0.0004	22	1201
KS14a	157	-0.0058 ± 0.0038	0.0016 ± 0.0017	420	63

Table 3.4: Geostrophic velocity offset [m s^{-1}] and trends [m s^{-1} year^{-1}] with uncertainties; finding a linear trend for five positions across the strait at selected depth levels (50, 150 m, and sectionally average) after the mean has been removed. Uncertainties are using a significance test to get the 95% confidence intervals using the null hypothesis according to Fofonoff and Bryden (1975). Degrees of freedom (dof) and decorrelation time scales T_D in hours are listed as well.

Mooring	Depth	Offset [m s^{-1}]	Trend [m s^{-1} year^{-1}]	dof	T_D
Sec. ave.	all	-0.019 ± 0.002	0.009 ± 0.001	69	381
KS02	50	-0.194 ± 0.008	0.092 ± 0.004	19	1383
KS04	50	0.047 ± 0.005	-0.022 ± 0.002	84	313
KS06	50	0.088 ± 0.006	-0.042 ± 0.003	49	528
KS08	50	0.018 ± 0.006	-0.009 ± 0.003	56	471
KS10	50	0.012 ± 0.004	-0.006 ± 0.002	118	223
KS02	150	-0.089 ± 0.004	0.042 ± 0.002	29	890
KS04	150	-0.028 ± 0.003	0.014 ± 0.001	46	570
KS06	150	-0.009 ± 0.002	0.004 ± 0.001	96	273
KS08	150	0.004 ± 0.001	-0.002 ± 0.001	274	96
KS10	150	0.003 ± 0.001	-0.001 ± 0.001	388	68

Table 3.5: Geostrophic volume and freshwater flux estimates (relative to 34.8 psu): Three-year means, three-year means per ice season, and fluxes per ice season with respective degrees of freedom (dof). The uncertainty in the flux estimates is a 95% confidence limit: $1.96\text{*std*}\sqrt{\frac{2}{n}}$ with $n = \frac{T}{T_D}$ the dof, T the record length, and T_D the decorrelation time scale of 200 hours.

Time	Geostr. Volume [Sv]	Geostr. Freshwater [mSv]	dof
3-year mean	0.47 ± 0.05	20 ± 3	132
3-year mean mobile ice	0.49 ± 0.08	22 ± 4	77
3-year mean fast-ice	0.48 ± 0.07	18 ± 3	55
Mobile ice 2003	0.49 ± 0.19	23 ± 10	25
Mobile ice 2004	0.38 ± 0.11	16 ± 5	23
Mobile ice 2005	0.51 ± 0.12	23 ± 6	24
Mobile ice 2006	0.57 ± 0.19	24 ± 7	5
Fast-ice 2003/04	0.49 ± 0.12	17 ± 3	12
Fast-ice 2004/05	0.43 ± 0.11	17 ± 4	24
Fast-ice 2005/06	0.51 ± 0.10	19 ± 4	19

Table 3.6: Geostrophic volume and freshwater flux offset [Sv/mSv] and trends [Sv/mSv year^{-1}] with uncertainties; finding a linear trend after the mean has been removed. Uncertainties are using a significance test to get the 95% confidence intervals using the null hypothesis according to Fofonoff and Bryden (1975) (* not significant).

Geostrophic Flux	Offset	Trend
Volume	-0.049 ± 0.013 Sv	0.023 ± 0.006 Sv year^{-1}
Freshwater*	-0.417 ± 0.620 mSv	0.198 ± 0.272 mSv year^{-1}
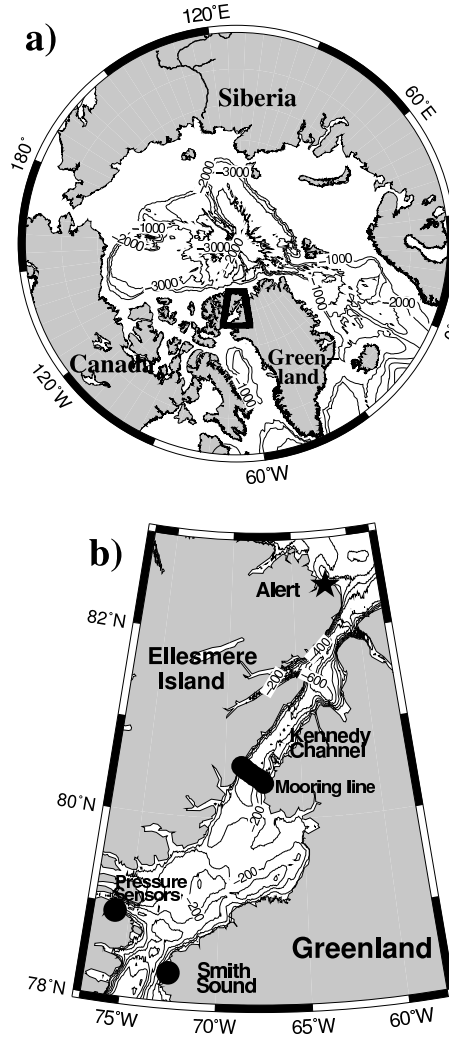
Figure 3.1: Study Area: a) Arctic Ocean with bottom topography with Nares
Strait marked in black triangle between Canada and Greenland, b)
Nares Strait with bottom topography with thick black line denoting
mooring line in Kennedy Channel. Black circles represent recovered
sub-surface pressure moorings with Foulke Fjord on the Greenland side
and Alexandra Fjord on the Ellesmere Island side (Canada). The star
denotes Alert in northeastern Ellesmere Island (tide gauge location).
Greenland lies to the east of Nares Strait. Smith Sound is to the south
with a sill depth of 230 m.
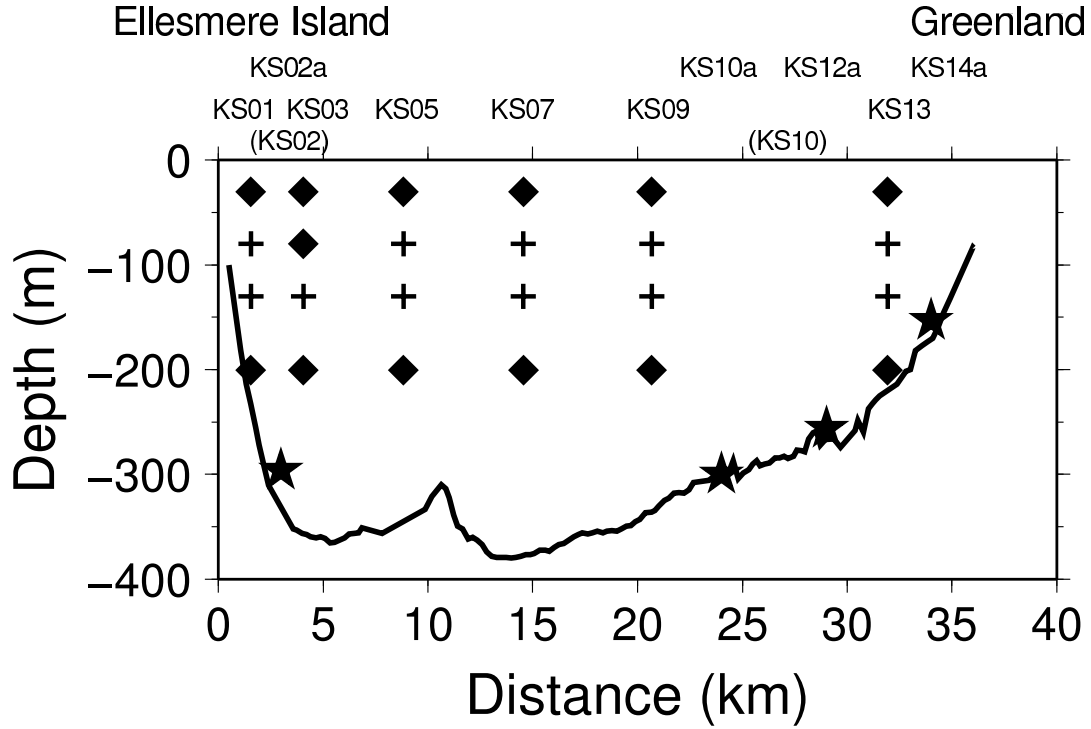
Figure 3.2: Position of recovered CT-strings including four CT instruments per string and bottom-mounted moorings including an ADCP and CT instrument in the strait, with Ellesmere Island (E. I.) on the left (west) and Greenland on the right (east). CT instruments were deployed at nominal 30, 80, 130 and 200 m, diamonds are instruments with pressure sensor, crosses without at their location and nominal depth in the strait. Stars denote bottom-mounted moorings. Mooring numbering is in sequence starting on the Ellesmere Island side with CT-moorings as odd numbers and bottom-mounted moorings as even numbers with an 'a' at the end. (KS02) shows mean position of geostrophic velocity between KS01 and KS03; (KS10) shows mean position of geostrophic velocity between KS09 and KS13.
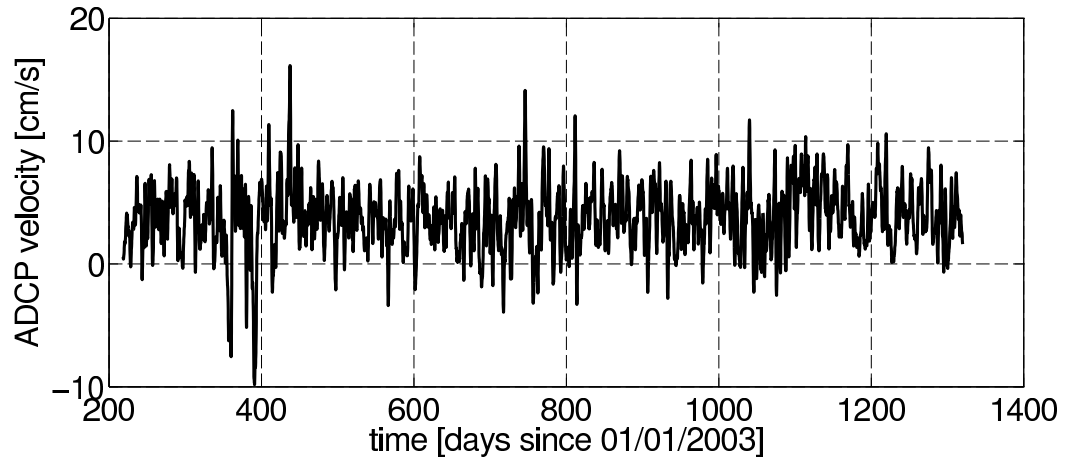
Figure 3.3: Time series of two-day low-pass filtered ADCP velocity used as the level of known motion from KS10a at 200 m in cm s^{-1}. Positive velocities are to the south. This time series is representative for velocities at 200 m across the whole strait.
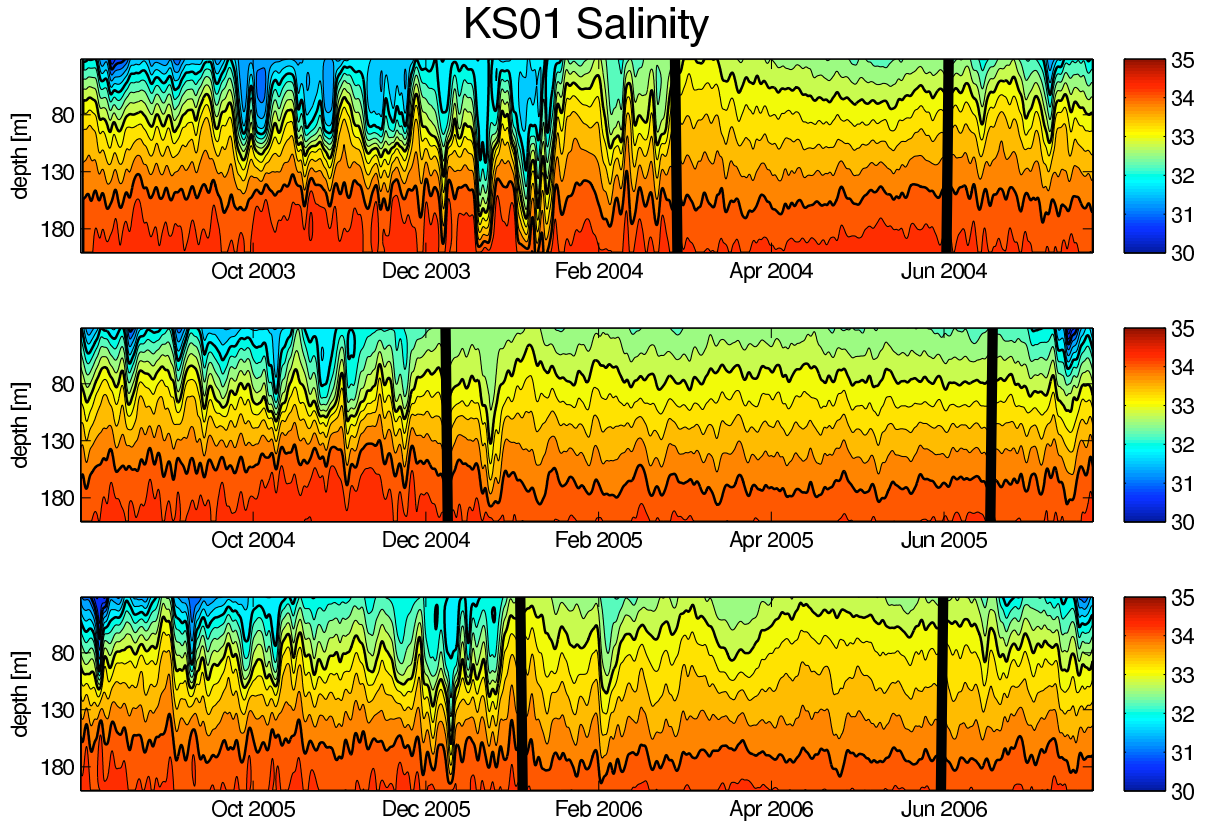
Figure 3.4: Hovmüller diagram for salinity as a function of time and depth at KS01. Each panel represents one year from August to August for 30 to 200 m. Thick vertical black lines represent change in the ice index, left and right side of each panel representing mobile ice seasons, middle part of each panel representing fast-ice seasons. Thicker isohalines are 34.0, 33.0, 32.0, 31.0 and 30.0 psu, thinner isohalines are 0.25 psu.
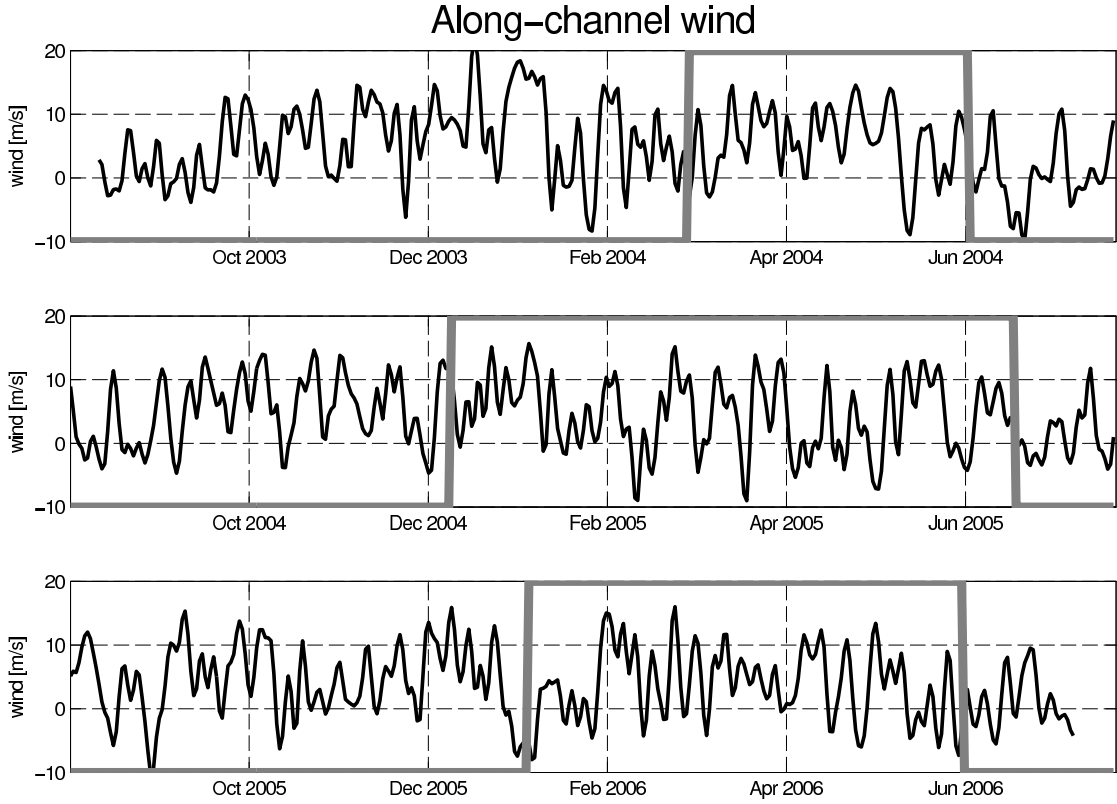
Figure 3.5: Time series of daily values of along-channel wind speed from the atmospheric model by Samelson and Barbour (2008) after Münchow and Melling (2008) in m s^{-1}. Positive velocities denote wind to the south. Each panel represents one year from August to August. The ice index is overlayed in grey with negative values for mobile ice seasons and positive values for fast-ice seasons (middle part of each panel representing fast-ice seasons and left and right side of each panel representing mobile ice seasons).
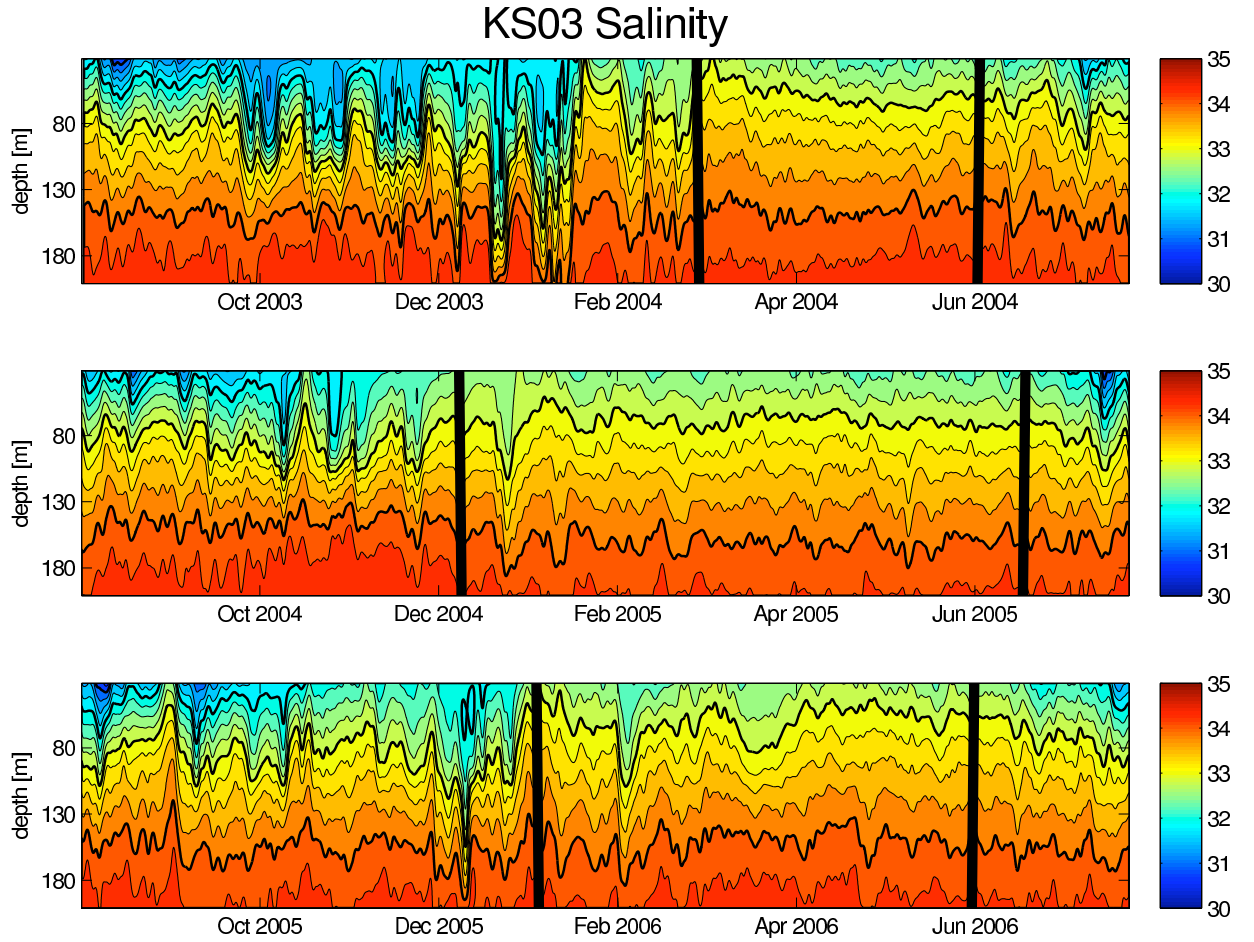
Figure 3.6: Hovmüller diagram for salinity as a function of time and depth at KS03. Each panel represents one year from August to August for 30 to 200 m. Thick vertical black lines represent change in the ice index, left and right side of each panel representing mobile ice seasons, middle part of each panel representing fast-ice seasons. Thicker isohalines are 34.0, 33.0, 32.0, 31.0 and 30.0 psu, thinner isohalines are 0.25 psu.
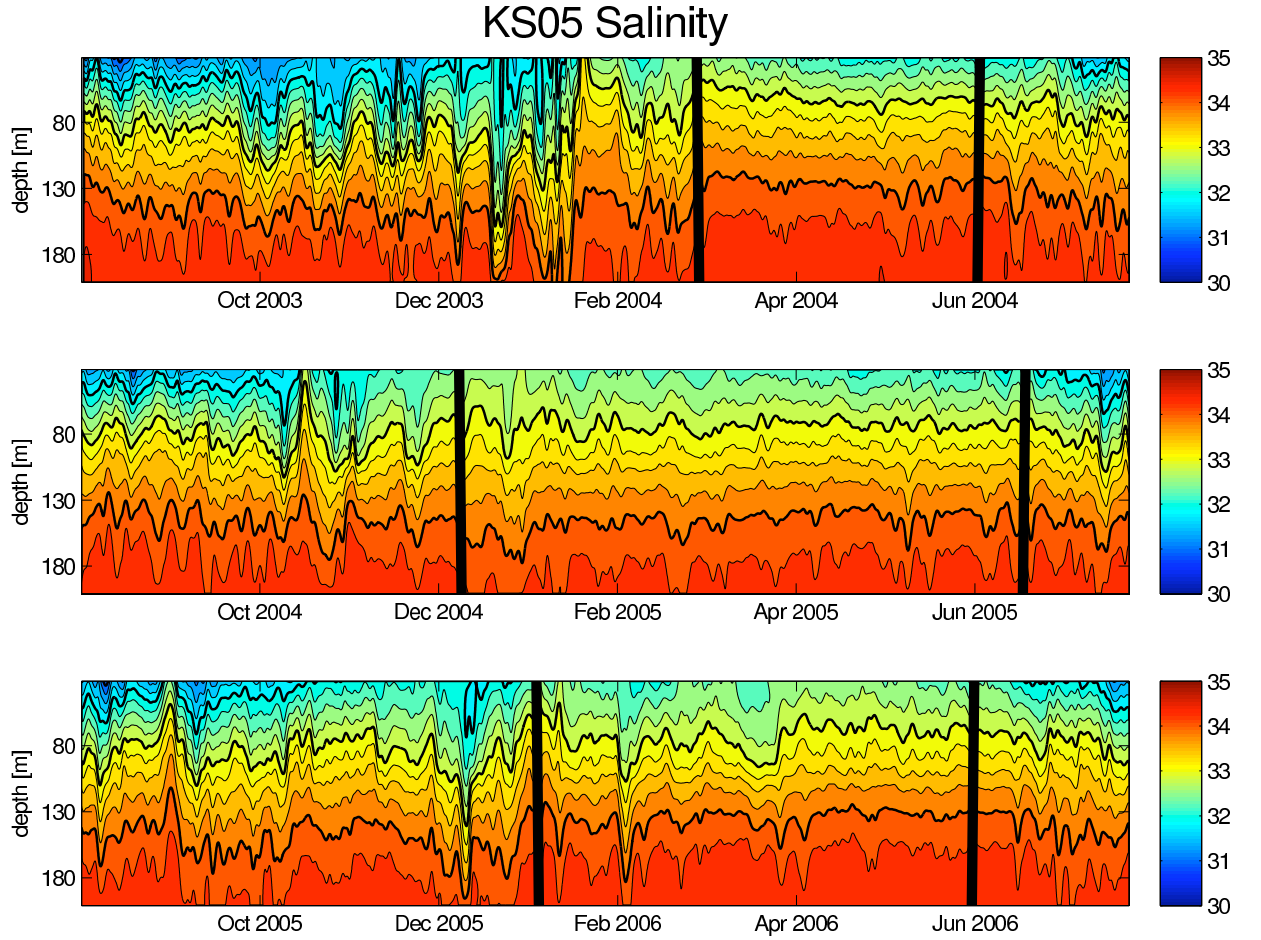
Figure 3.7: Hovmüller diagram for salinity as a function of time and depth at KS05. Each panel represents one year from August to August for 30 to 200 m. Thick vertical black lines represent change in the ice index, left and right side of each panel representing mobile ice seasons, middle part of each panel representing fast-ice seasons. Thicker isohalines are 34.0, 33.0, 32.0, 31.0 and 30.0 psu, thinner isohalines are 0.25 psu.
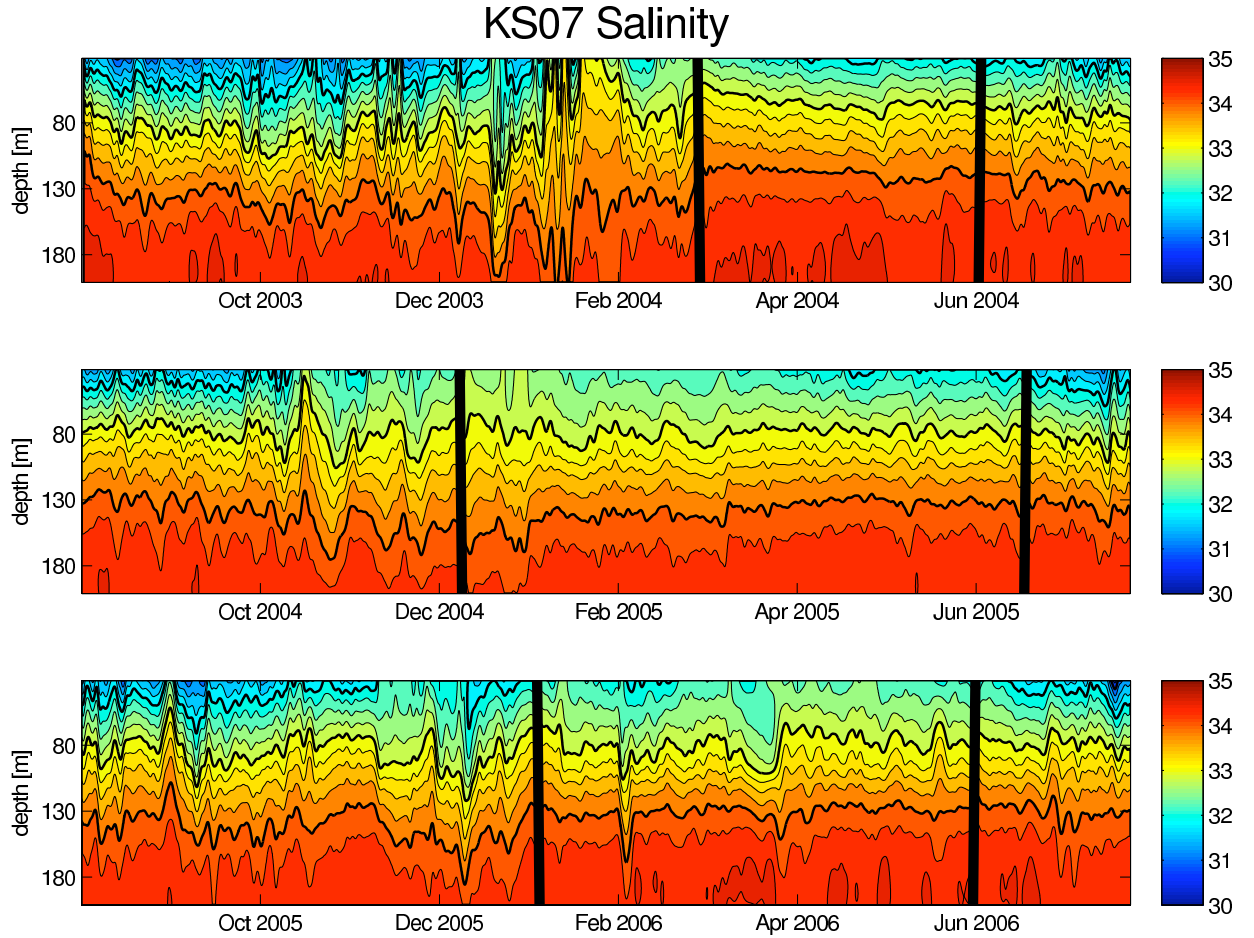
Figure 3.8: Hovmüller diagram for salinity as a function of time and depth at KS07. Each panel represents one year from August to August for 30 to 200 m. Thick vertical black lines represent change in the ice index, left and right side of each panel representing mobile ice seasons, middle part of each panel representing fast-ice seasons. Thicker isohalines are 34.0, 33.0, 32.0, 31.0 and 30.0 psu, thinner isohalines are 0.25 psu.

97
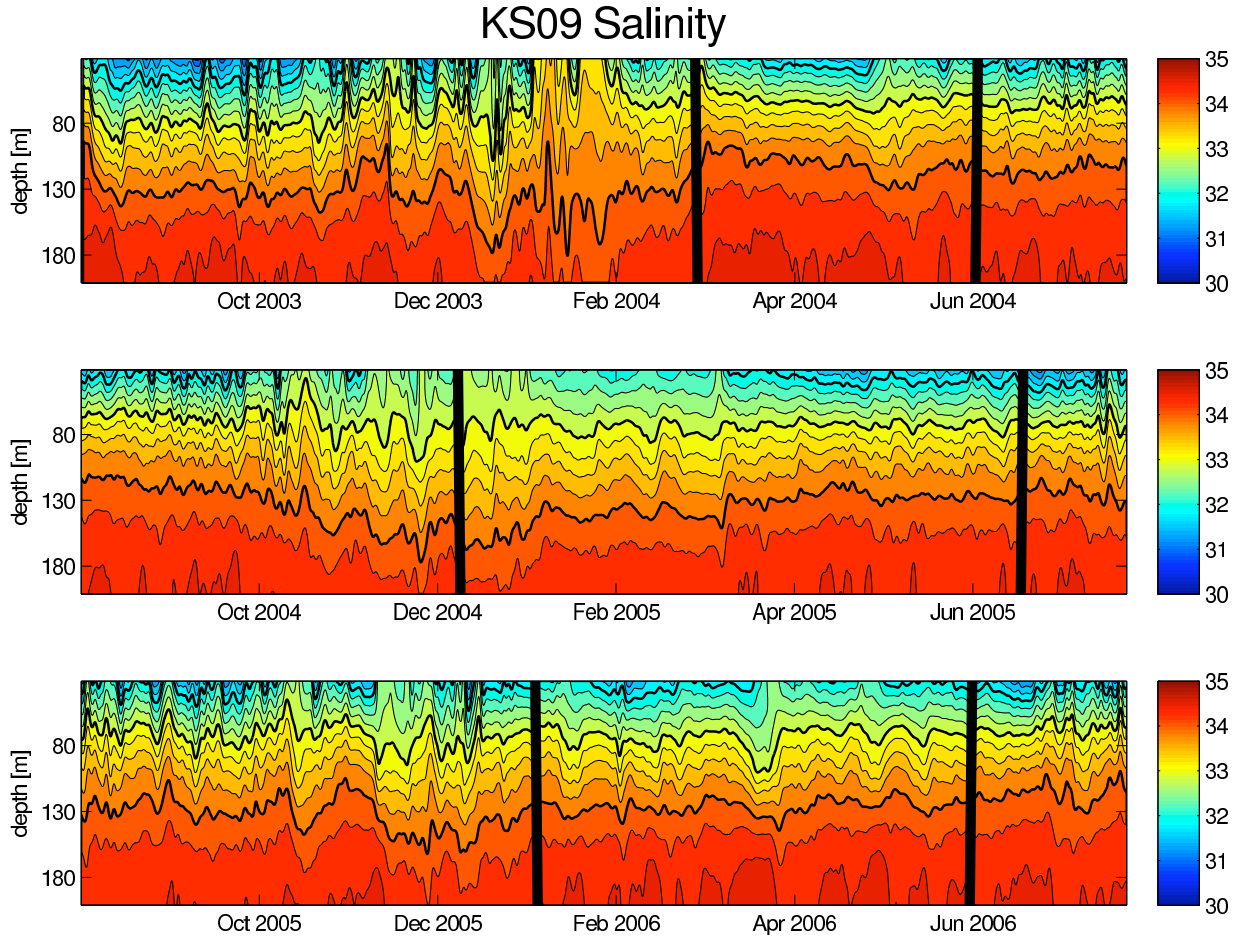
Figure 3.9: Hovmüller diagram for salinity as a function of time and depth at KS09. Each panel represents one year from August to August for 30 to 200 m. Thick vertical black lines represent change in the ice index, left and right side of each panel representing mobile ice seasons, middle part of each panel representing fast-ice seasons. Thicker isohalines are 34.0, 33.0, 32.0, 31.0 and 30.0 psu, thinner isohalines are 0.25 psu.
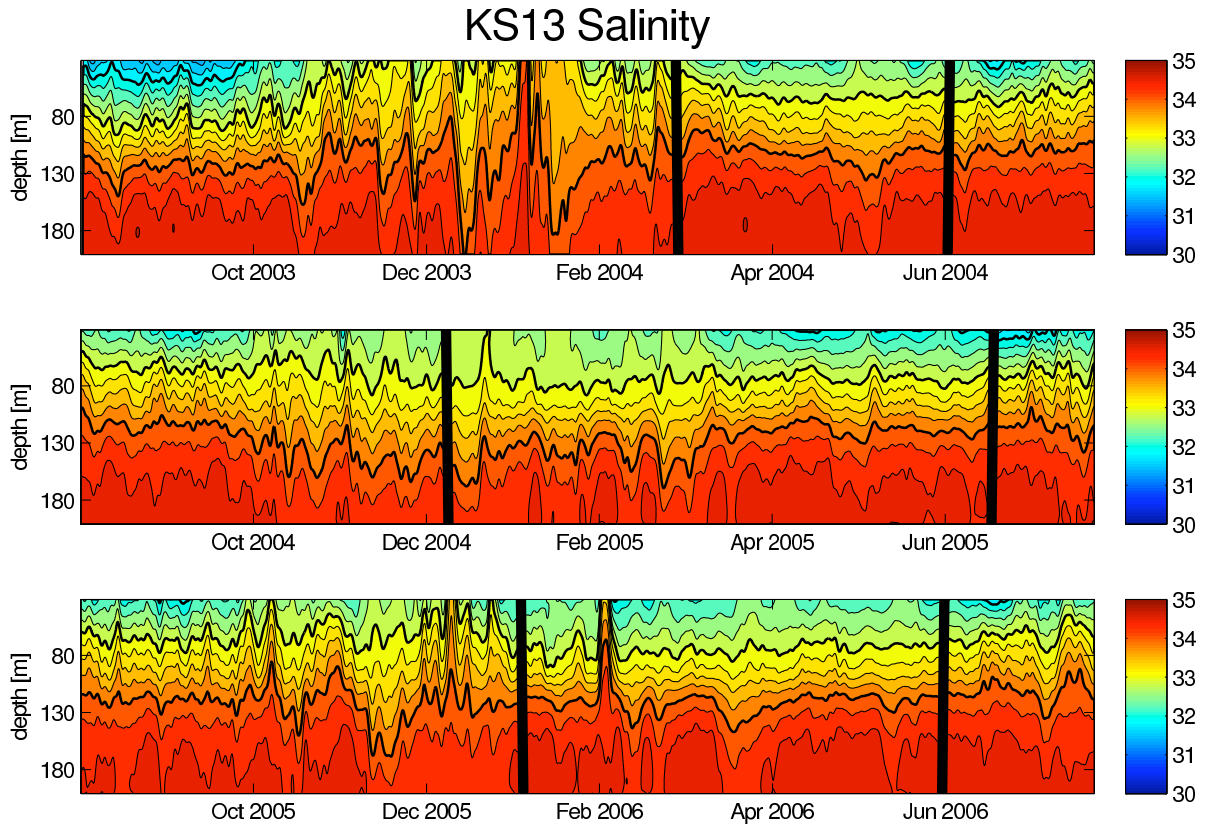
Figure 3.10: Hovmüller diagram for salinity as a function of time and depth at KS13. Each panel represents one year from August to August for 30 to 200 m. Thick vertical black lines represent change in the ice index, left and right side of each panel representing mobile ice seasons, middle part of each panel representing fast-ice seasons. Thicker isohalines are 34.0, 33.0, 32.0, 31.0 and 30.0 psu, thinner isohalines are 0.25 psu.
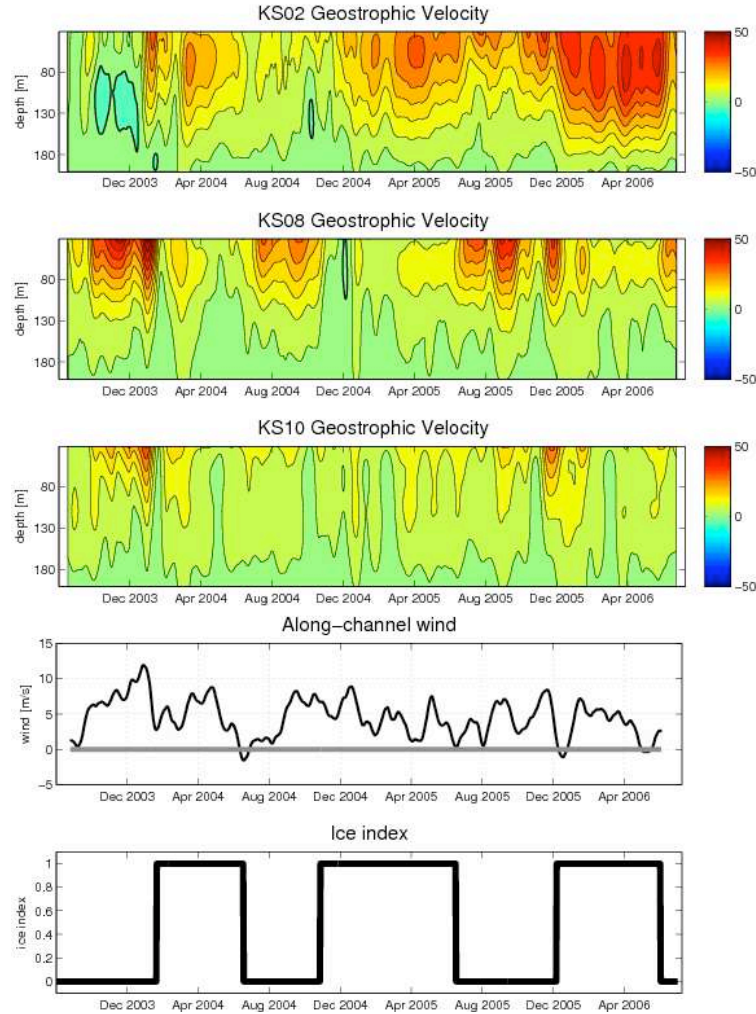
Figure 3.11: Hovmüller diagrams for 30-day low-pass filtered absolute geostrophic velocity as a function of time and depth at KS02, KS08, and KS10. Positive geostrophic velocities are to the south in cm s^{-1}. Each panel represents the three-year record for each location from August 2003 to August 2006 for 30 to 200 m. The zero line in geostrophic velocity is marked by a thicker black contour line with darker blue being negative (to the north), thinner contour lines are 0.05 cm s^{-1}. The 30 day low-pass filtered along-channel wind is plotted (zero line in grey) as well as the index with zero representing mobile ice seasons and one fast-ice seasons.

100

KS02 Geostrophic Velocity
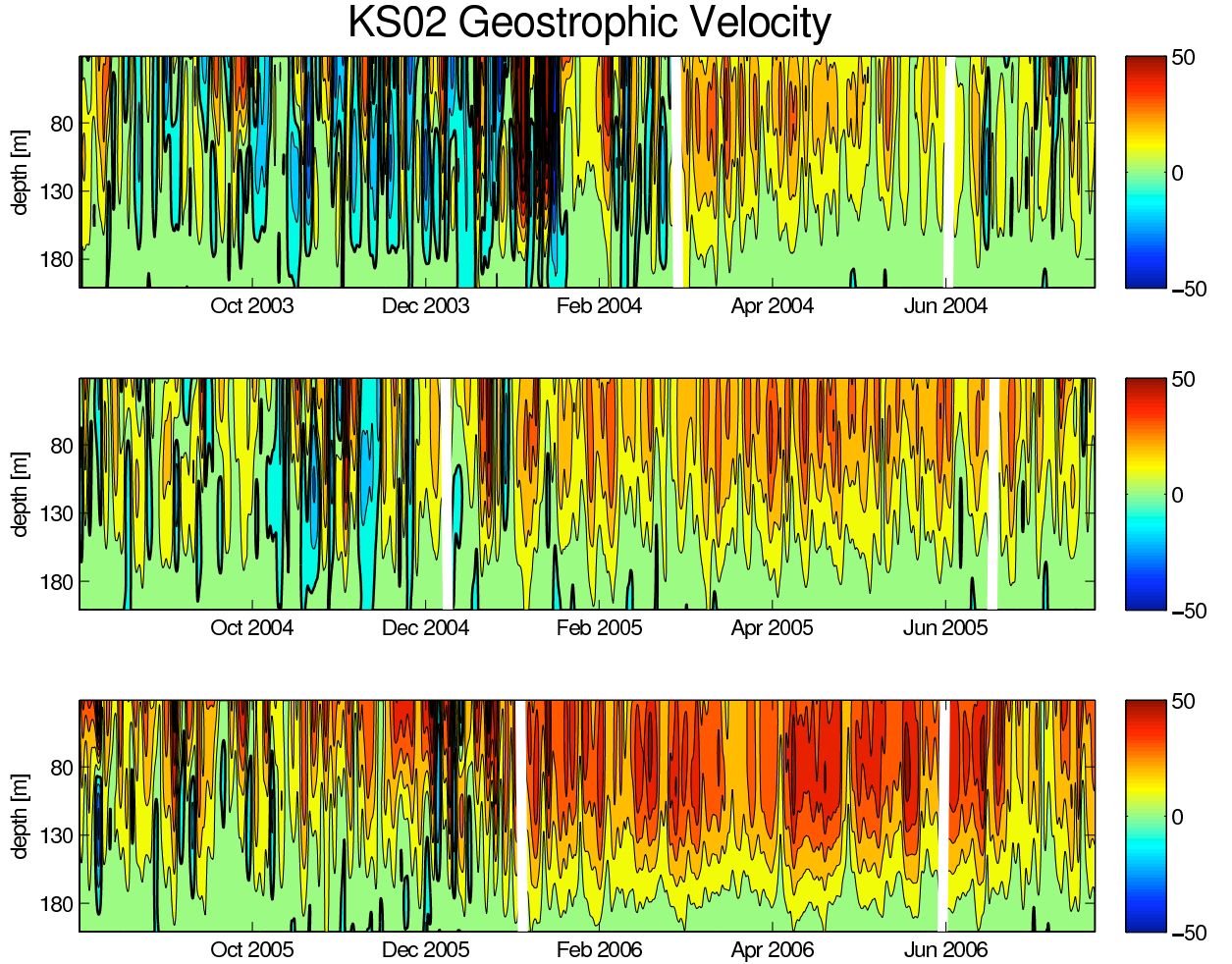
Figure 3.12: Hovmüller diagram for absolute geostrophic velocity as a function of time and depth at KS02. Positive geostrophic velocities are to the south in cm s^{-1}. Each panel represents one year from August to August. Thick vertical white lines represent change in the ice index, left and right side of each panel representing mobile ice seasons, middle part of each panel representing fast-ice seasons. The zero line in geostrophic velocity is marked by a thicker black contour with darker blue being negative (to the north), thinner contour lines are 10 cm s^{-1}.
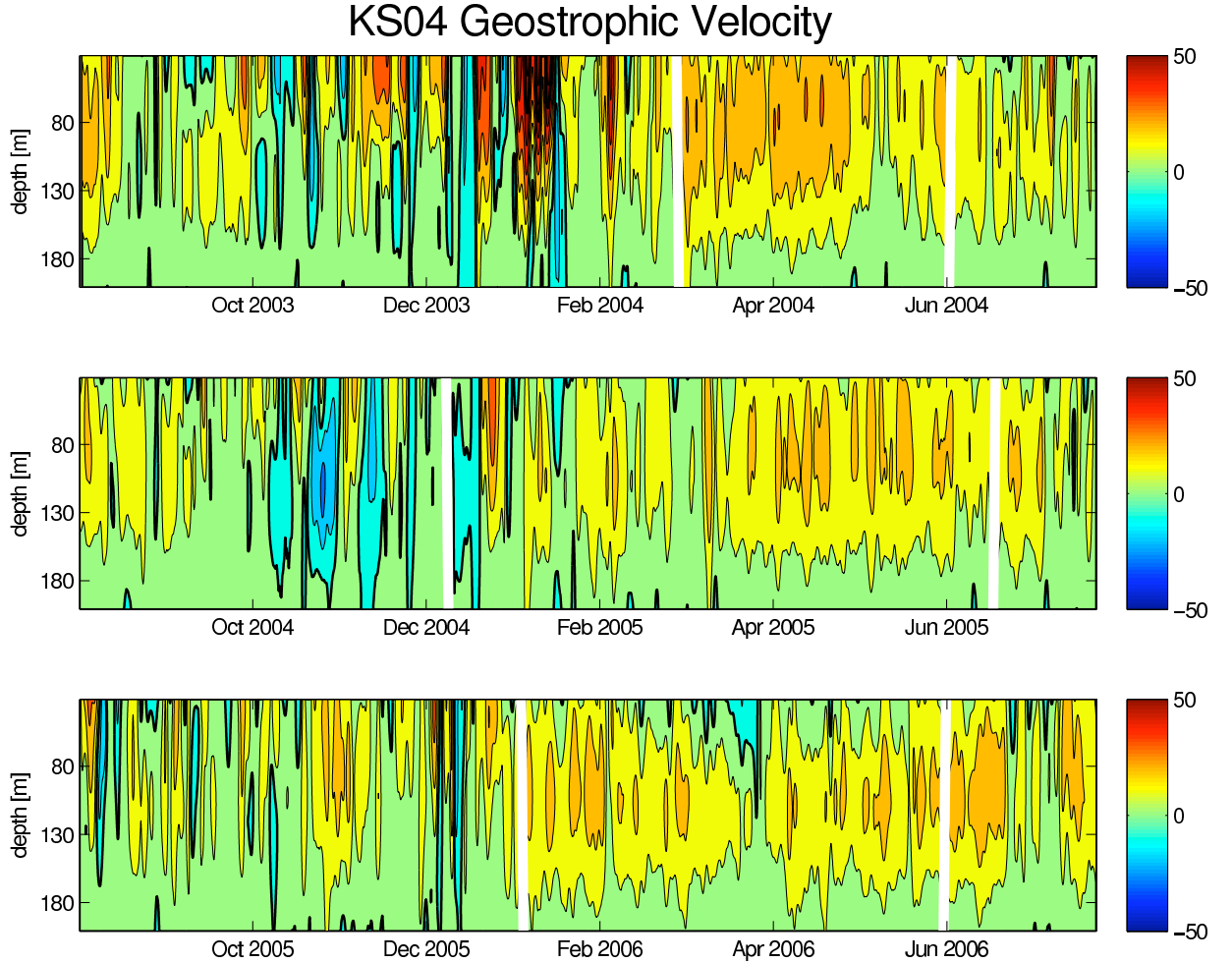
Figure 3.13: Hovmüller diagram for absolute geostrophic velocity as a function of time and depth at KS04. Positive geostrophic velocities are to the south. Each panel represents one year from August to August. Thick vertical white lines represent change in the ice index, left and right side of each panel representing mobile ice seasons, middle part of each panel representing fast-ice seasons. The zero line in geostrophic velocity is marked by a thicker black contour with darker blue being negative (to the north), thinner contour lines are 10 cm s^{-1}.
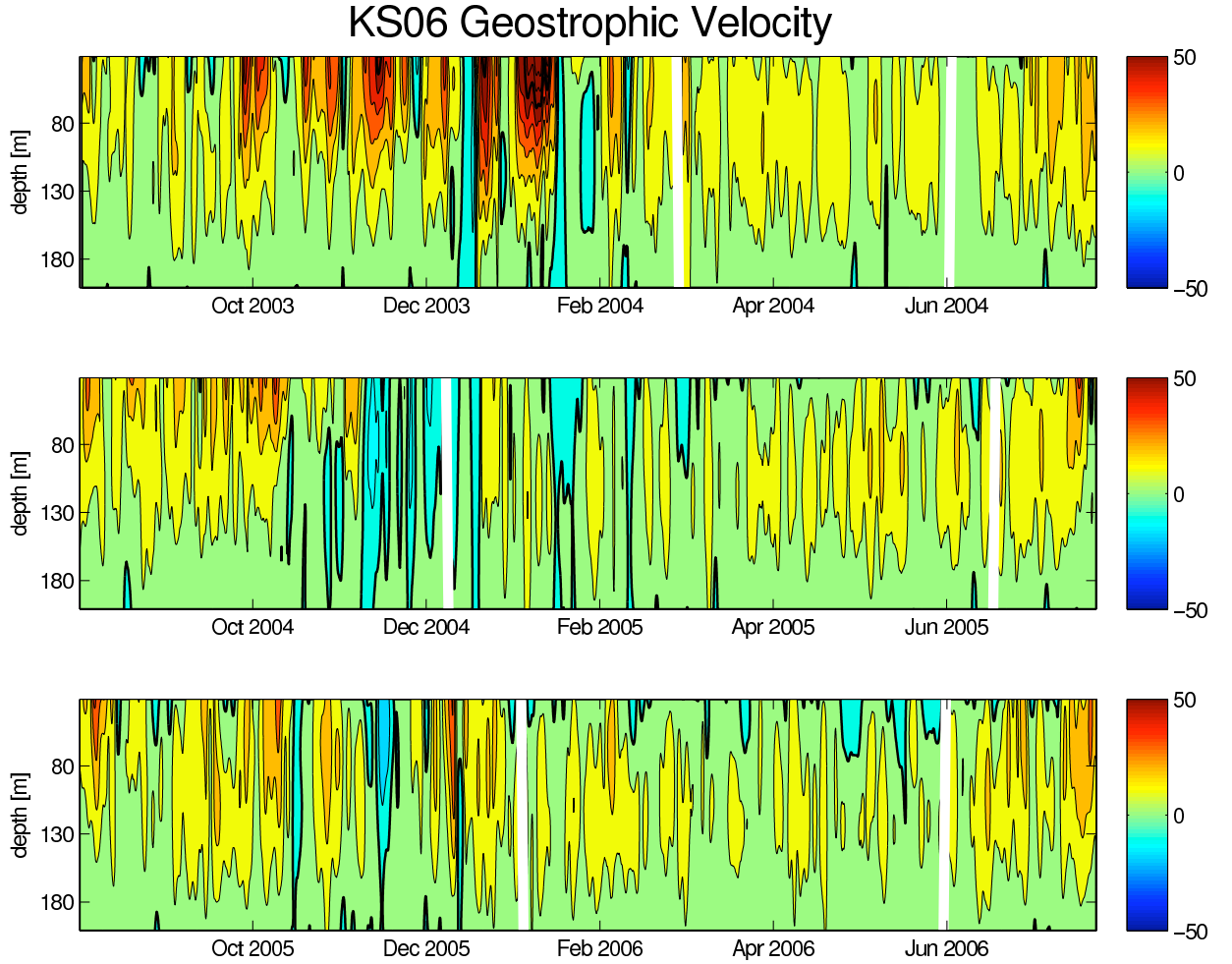
Figure 3.14: Hovmüller diagram for absolute geostrophic velocity as a function of time and depth at KS06. Positive geostrophic velocities are to the south in cm s^{-1}. Each panel represents one year from August to August for 30 to 200 m. Thick vertical white lines represent change in the ice index, left and right side of each panel representing mobile ice seasons, middle part of each panel representing fast-ice seasons. The zero line in geostrophic velocity is marked by a thicker black contour with darker blue being negative (to the north), thinner contour lines are 10 cm s^{-1}.
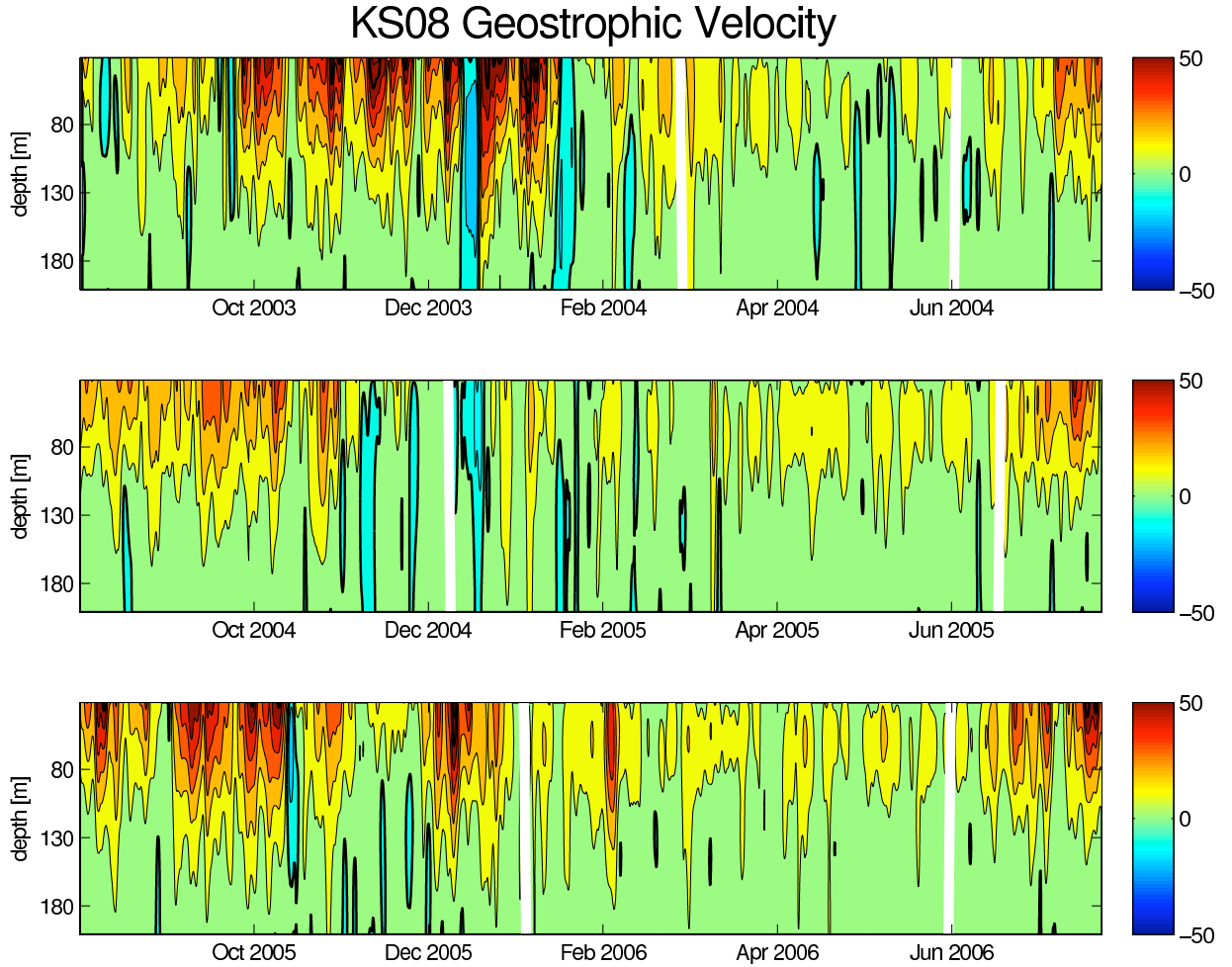
Figure 3.15: Hovmüller diagram for absolute geostrophic velocity as a function of time and depth at KS08. Positive geostrophic velocities are to the south in cm s^{-1}. Each panel represents one year from August to August for 30 to 200 m. Thick vertical white lines represent change in the ice index, left and right side of each panel representing mobile ice seasons, middle part of each panel representing fast-ice seasons. The zero line in geostrophic velocity is marked by a thicker black contour with darker blue being negative (to the north), thinner contour lines are 10 cm s^{-1}.

KS10 Geostrophic Velocity
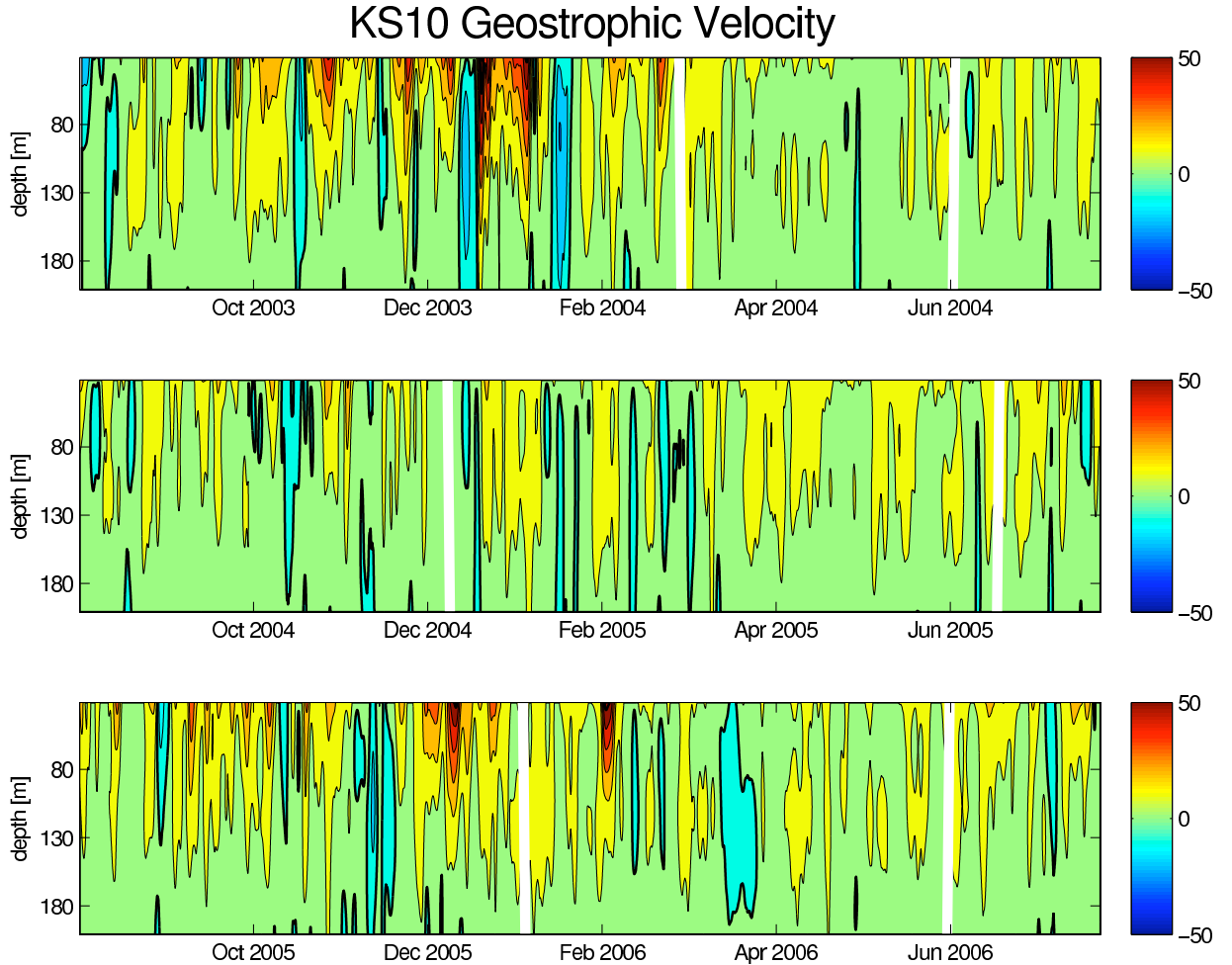
Figure 3.16: Hovmüller diagram for absolute geostrophic velocity as a function of time and depth at KS10. Positive geostrophic velocities are to the south in cm s^{-1}. Each panel represents one year from August to August for 30 to 200 m. Thick vertical white lines represent change in the ice index, left and right side of each panel representing mobile ice seasons, middle part of each panel representing fast-ice seasons. The zero line in geostrophic velocity is marked by a thicker black contour with darker blue being negative (to the north), thinner contour lines are 10 cm s^{-1}.
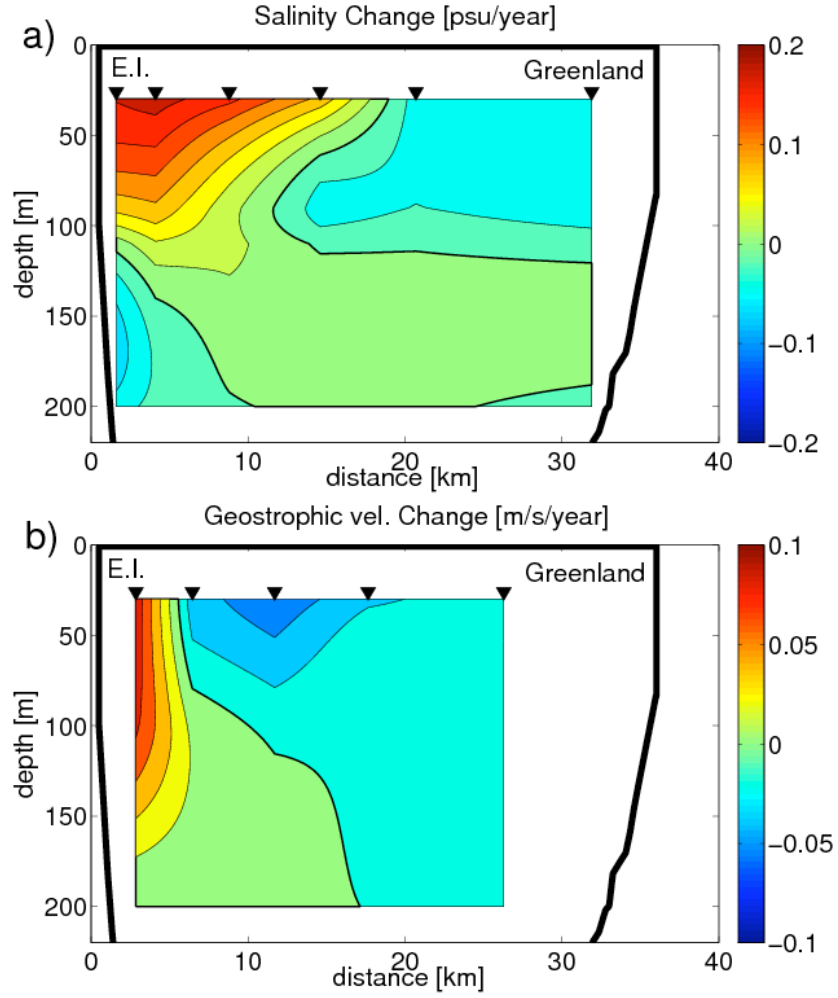
Figure 3.17: Salinity rate of change [psu year^{-1}] with contours of 0.025 psu year^{-1} (a) and geostrophic velocity rate of change [m s^{-1} year^{-1}] with contours of 0.02 m s^{-1} year^{-1} (b). Black triangles denote position of data points at one meter vertical resolution. Thick isolines demonstrates zero change with blue and red denoting opposite signs. The error from sensor drift is explained in detail in Appendix 3.8.1.
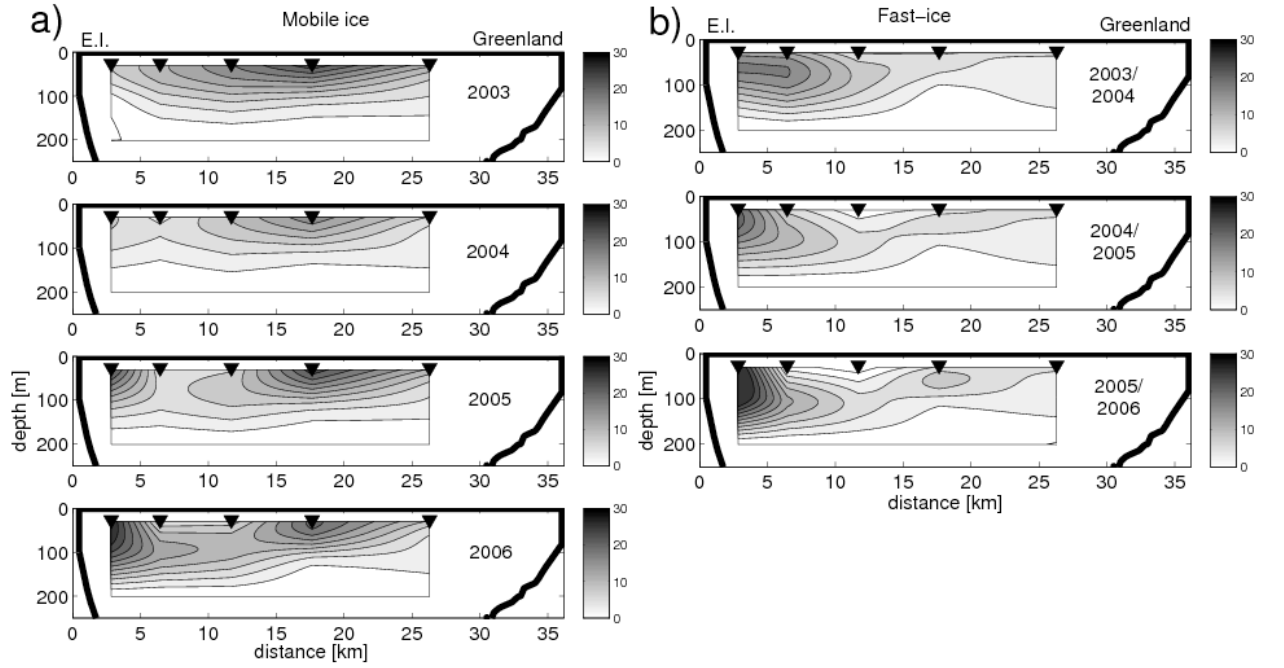
Figure 3.18: Sections of geostrophic velocity at seasonal time scales during each mobile (a) and fast-ice (b) ice season. Zero geostrophic velocity is denoted in white, maximum geostrophic velocity to the south in black [cm s^{-1}]. Black triangles denote position of data points at one meter vertical resolution. Contour lines are 2.5 cm s^{-1}.
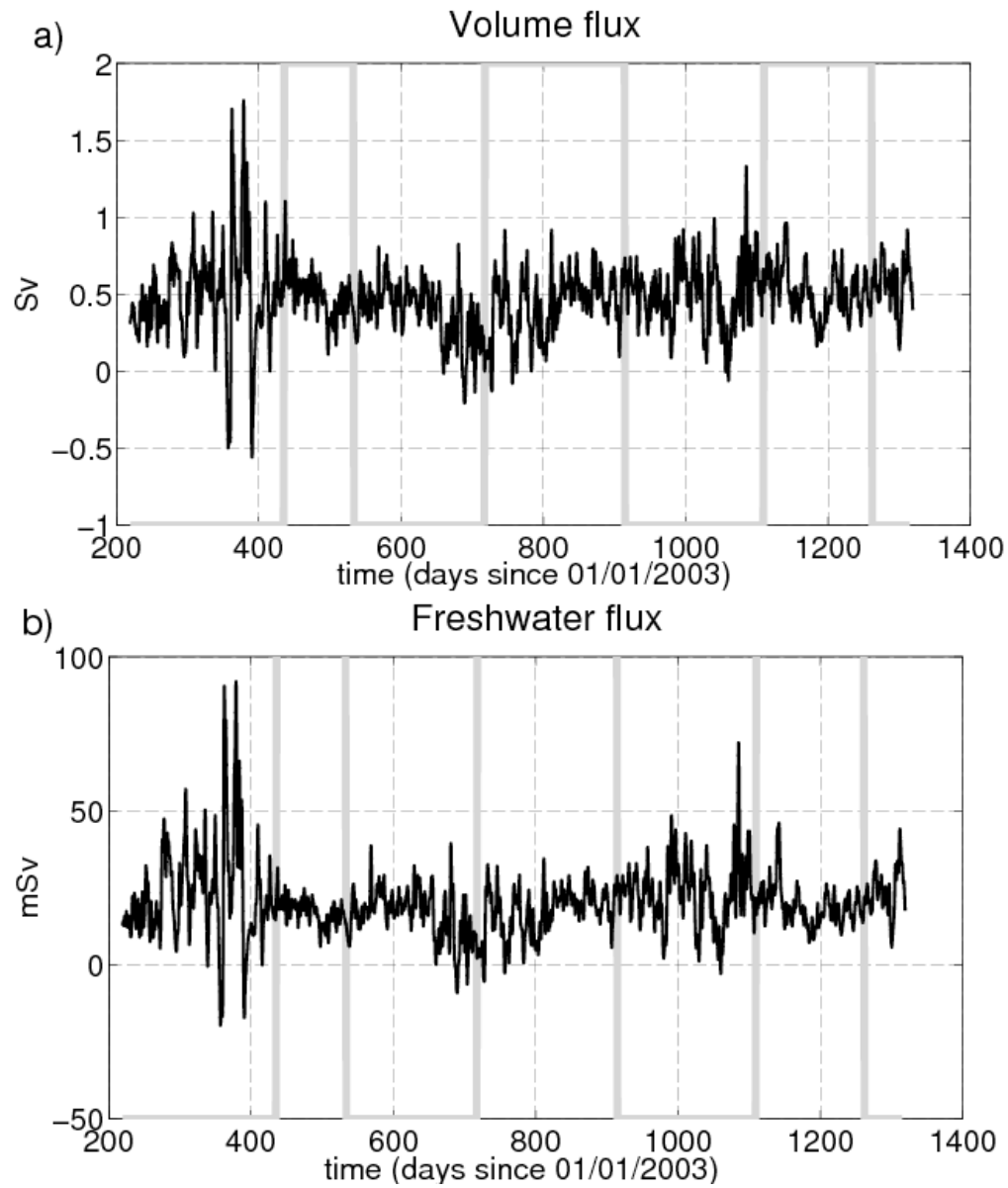
Figure 3.19: Three-year geostrophic volume flux (a), and freshwater flux (relative to 34.8 psu) (b) time series (daily values, two-day low-pass filtered). The ice index is overlayed (light gray step function) with positive values representing fast-ice seasons, and negative values representing mobile ice seasons. Note the large dependence on the ice state with large variability during mobile ice seasons.
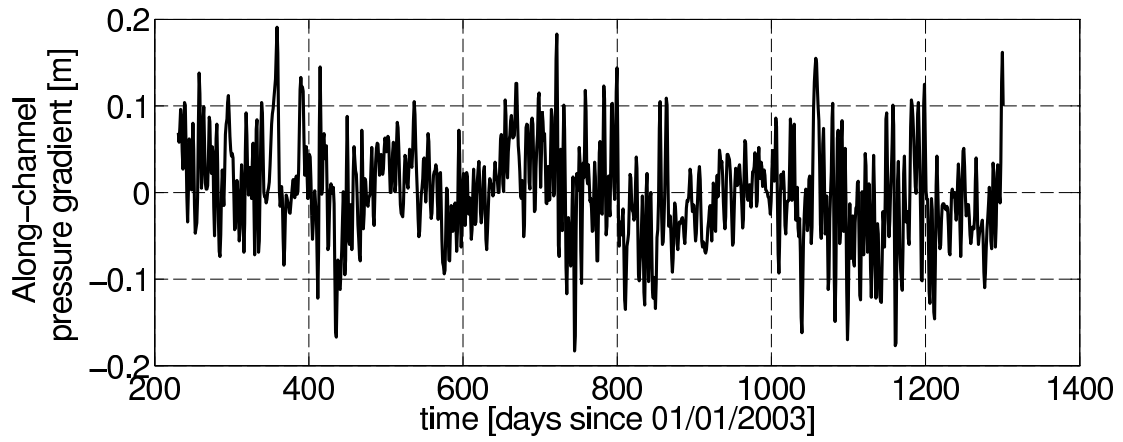
Figure 3.20: Time series of along-channel pressure difference after Münchow and Melling (2008) in m. Positive velocities denote a higher pressure in the north.
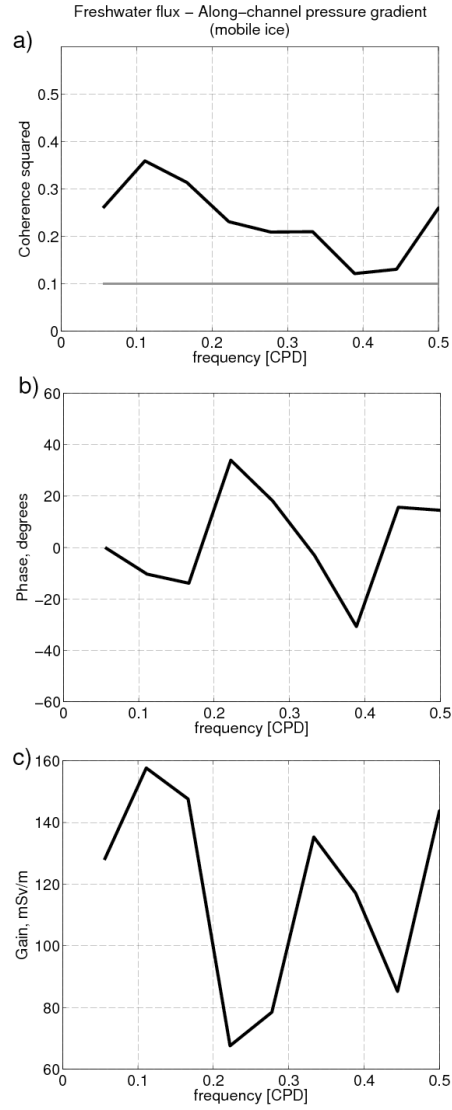
Figure 3.21: Coherence squared (a), phase [degrees] (b), and gain [mSv m^{-1}] (c) between geostrophic freshwater flux and along-channel pressure difference during mobile ice seasons (185 days per season). The gray line in a) denotes the 95% confidence level.
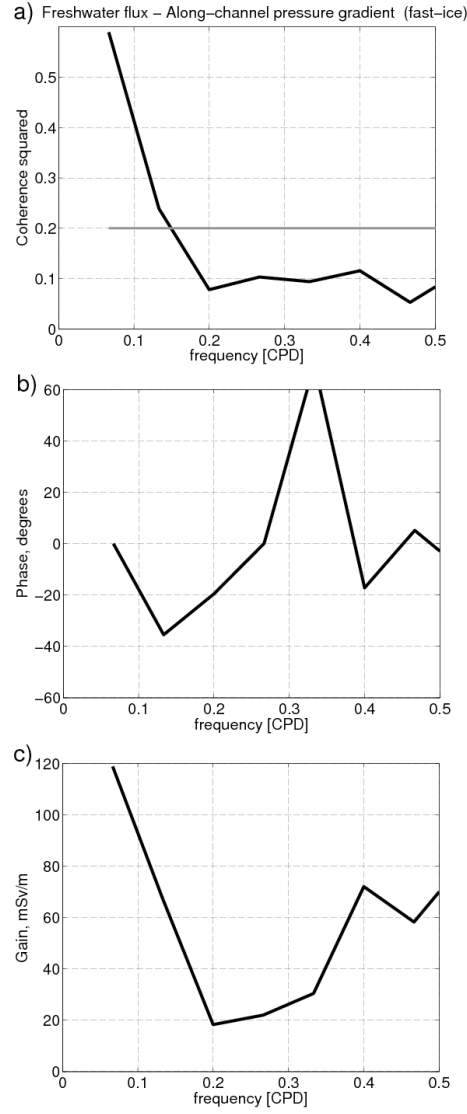
Figure 3.22: Coherence squared (a), phase [degrees] (b), and gain [mSv m^{-1}] (c) between geostrophic freshwater flux and along-channel pressure difference during fast-ice seasons in 2004/05 and 2005/06 (153 days per season). The gray line in a) denotes the 95% confidence level.
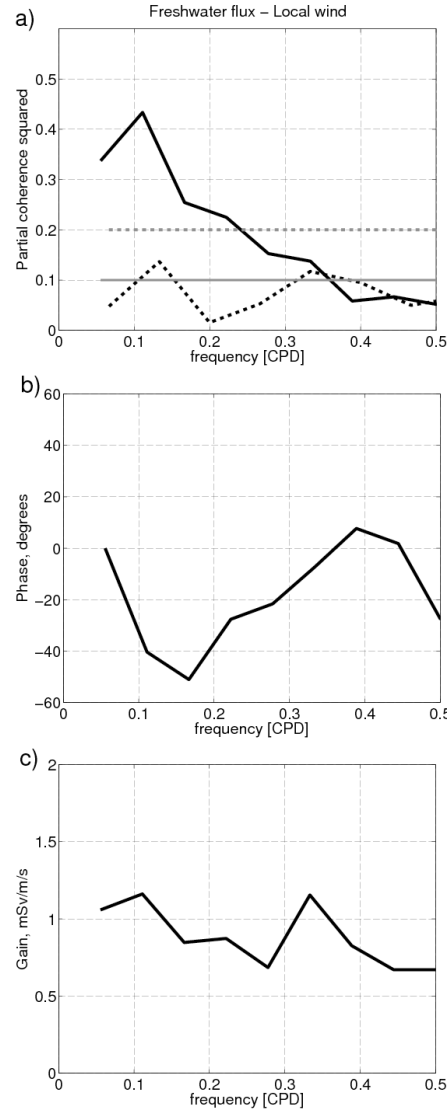
Figure 3.23: Partial coherence squared (a), phase [degrees] (b), and gain [mSv (m/s)$^{-1}$] (c) between geostrophic freshwater flux and local wind stress (not correlated with the along-channel pressure difference). In a) the black line denotes the partial coherence squared during mobile ice seasons, the dark gray line denotes the corresponding 95% confidence level. The black dotted line is the partial coherence squared during fast-ice seasons in 2004/05 and 2005/06 with the light grey dotted line the corresponding 95% confidence level. The partial coherence squared is always below the 95% confidence level therefore phase and gain are not plotted for fast-ice seasons only for the mobile ice seasons.
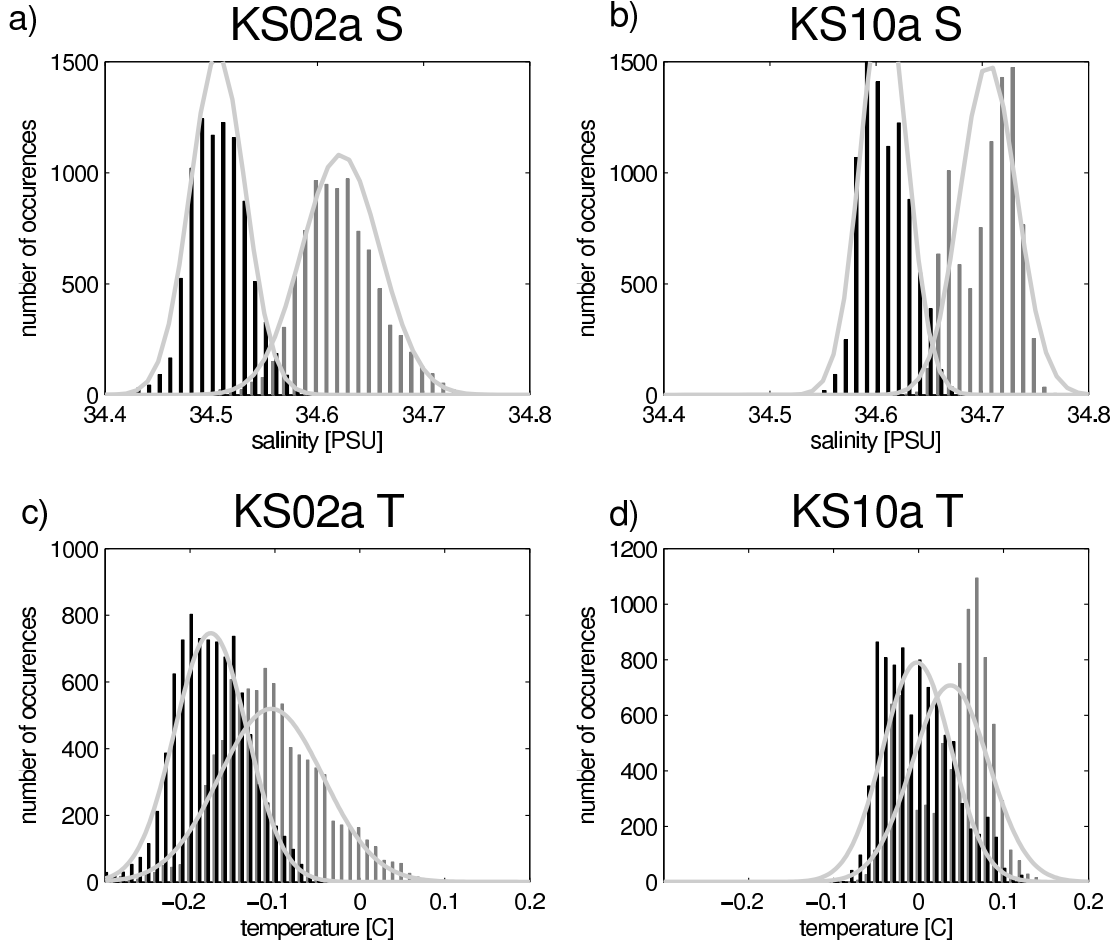
Figure 3.24: Salinity and temperature data from bottom-mounted CT instruments used for calibration from KS02a (a and c) and KS10a (c and d). a) and b) are histograms of salinities for beginning (first three months in gray) and end (last three months in black) of record with a Gaussian distribution in light gray overlaid. Salinities are normally distributed and shifted towards lower salinities during the deployment period. b) and d) are histograms of temperature for beginning (first three months in gray) and end (last three months in black) of record with a Gaussian distribution in light gray overlaid. Temperatures are normally distributed as well and shifted towards lower temperatures during the deployment period.

113
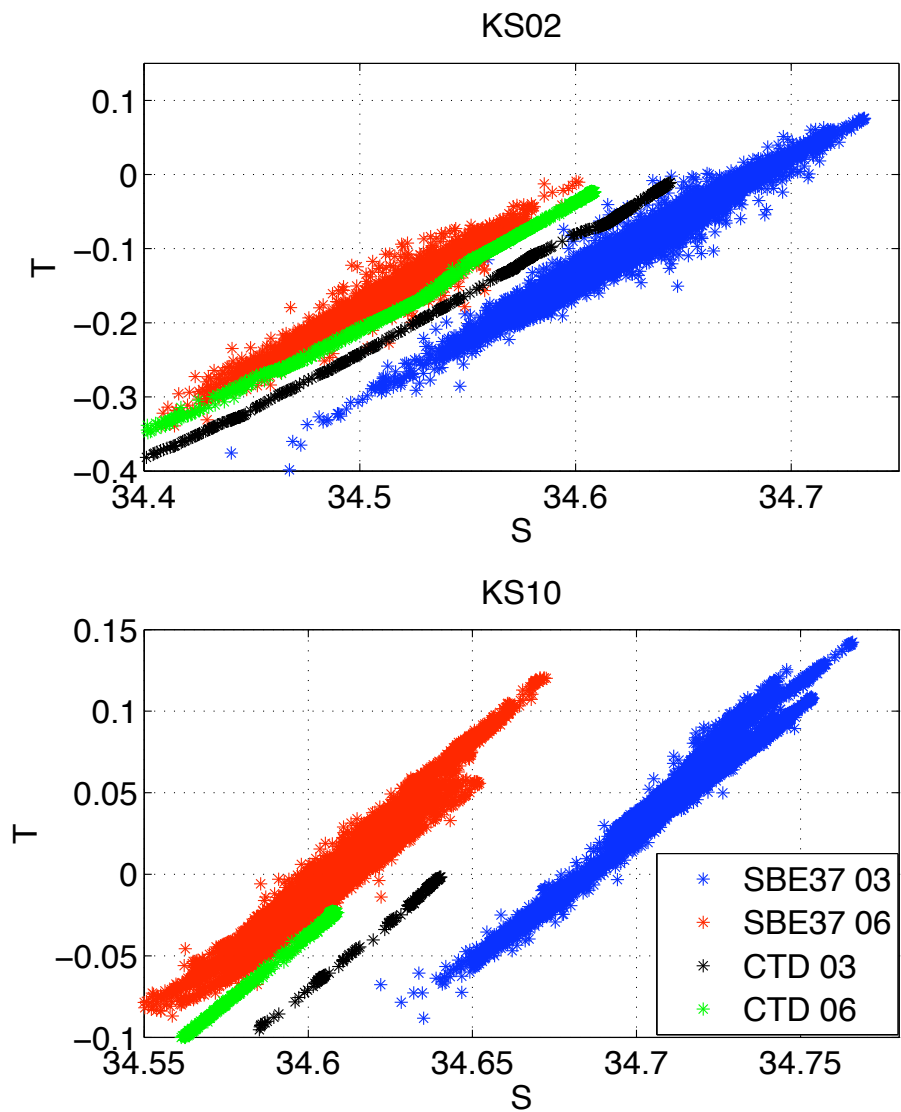
Figure 3.25: TS diagrams at KS02 and KS10 with first three months of SBE37 data plotted in blue, last three months of SBE37 data in red, CTD data in 2003 at KS03 for KS02 and KS11 for KS10 in black, and CTD data in 2006 at KS10 for both plots.

Chapter 4

COMPARISON BETWEEN GEOSTROPHIC
AND ADCP VELOCITY IN NARES STRAIT
BETWEEN 2003 AND 2006

4.1   Introduction

In the previous chapters the focus has been on geostrophic flows and fluxes in
Nares Strait with the only use of ADCP velocity measurements as the level of known
motion at 200 m. Münchow and Melling (2008) evaluated only the depth-averaged
ADCP velocities for 2003–06. In this chapter we will evaluate if the flow in Nares
Strait is indeed geostrophic. A direct comparison between calculated geostrophic
velocities with measured ADCP velocities will be performed at two locations.

In this chapter, first the data is presented in 4.2, then the velocity comparison
at two locations within the time domain is performed (section 4.3.1), followed by a
frequency domain analysis (section 4.3.2). A discussion of the discrepancy on the
Ellesmere Island side including the lateral boundary condition is explained using
free-slip/no-slip arguments and vertical friction arguments from Valle-Levinson's
(2008) model runs (section 4.4) before concluding this chapter (section 4.5).

4.2   Study Area and Data

As in the previous chapters the focus here is on Nares Strait with an analysis
of the mooring data from 2003–06. The high vertical resolution CT data from the
multiple linear regression model from chapter 3 is used here. In this chapter we will

compare the geostrophic velocities calculated from the high resolution data set with the measured ADCP velocity where the two data sets overlap. On the western side of the strait ADCP site KS02 and geostrophic velocity calculated between KS01 and KS03 cover the same portion of the strait. On the eastern side a comparison will be made between ADCP site KS10 and the geostrophic velocity calculated between KS09 and KS13, roughly representing the same portion of the strait. Fig. 4.1 shows the locations of ADCP sites KS02, and KS10, and the CT strings KS01, KS03, KS09, and KS13 between which the geostrophic velocity is calculated. We compare estimated geostrophic velocities from the CT moorings with currents from ADCPs at two different locations during the two different ice states. Note that ADCP data above 50 m is not plotted here at this point due to data processing problems in the top layers.

4.3 Velocity Comparison at two locations in Nares Strait

4.3.1 Time Domain Analysis

Comparing geostrophic and ADCP velocities at KS10 in the eastern part of the strait, velocities overlap and are comparable during both ice conditions. During fast-ice seasons the geostrophic velocity resembles an S shape similar to the feature in the ADCP data (Fig. 4.2d). During the 2003/04 fast-ice season ADCP velocities decrease above 100 m in comparison to the other years. During mobile ice seasons geostrophic velocity increases from 200 m to about 70 m and then increases more strongly in the top layers (Fig. 4.2b). A similar feature is again observed in the ADCP data.

At KS02 in the western part of Nares Strait close to Ellesmere Island during fast-ice seasons the profile shapes of both velocities are congruent with increasing velocities from 200 m to about 75 m and a decrease in velocities above that (Fig. 4.2c). The ADCP velocities are similar during all three fast-ice seasons. The geostrophic velocities increase about 0.05 m s^{-1} from the 2003/04 to the 2004/05 fast-ice season

116

mostly in the top 100 m. The difference between 2004/05 and 2005/06 fast-ice seasons demonstrates another increase of up to 0.08 m s^{-1} at all levels. The maximum geostrophic velocity between 60 m and 80 m reaches 0.36 m s^{-1}. The observed currents from the ADCP at this location are a factor of two smaller than the geostrophic currents estimated from CT data.

During the 2003 and 2004 mobile ice seasons the two different velocities are comparable (Fig. 4.2a). Velocities are almost constant with depth suggesting a barotropic flow. The 2005 mobile ice season demonstrates an increase in geostrophic velocity in comparison to the previous mobile ice season. Geostrophic velocities in the top layers increase by up to 0.15 m s^{-1}. The 2006 mobile ice season (only 59 days long due to mooring recovery) shows another increase by 0.10 m s^{-1}, most pronounced at a depth of 100 m, consistent with the strengthening sub-surface core on the Ellesmere Island side as discussed earlier. The agreement between geostrophic and ADCP velocity close to the Ellesmere Island coast is low during all fast-ice seasons and the 2005 and 2006 mobile ice seasons and will be discussed below.

4.3.2   Frequency Domain Analysis

We here compare geostrophic and ADCP velocity time series in the frequency domain because we want to evaluate the correlated variance between geostrophic and ADCP velocities as a function of frequency. Fig. 4.3 shows the results at three selected depths (50, 100, and 150 m) for KS02 and KS10.

At KS10 we already saw in the vertical velocity profiles that geostrophic and ADCP velocities are of comparable magnitude at all depths. The agreement between both velocities in the center of the channel is good. The coherence squared (Fig. 4.3d) shows at which frequencies the correlated variance is highest. At frequencies below 0.08 cpd (12.5 days) the coherence squared is high—larger than 0.4 for 100 m and 0.5 for 50 m. About 50–80% of the correlated variance between geostrophic and ADCP velocity is explained at frequencies lower than about 0.1 cpd

(10 days). Velocities at deeper layers are insignificantly correlated at frequencies higher than 0.04 cpd (25 days). Coherence squared between velocities in the top layers is below the 95% confidence level at frequencies higher than 0.3 cpd (3.3 days) and 0.08 cpd (12.5 days) for 50 and 100 m, respectively. The gain—the amplitude relationship between the two velocity time series data as a function of frequency—is close to one for the top layers at frequencies below 0.08 cpd (12.5 days). This means that the amplitude of variations in geostrophic and ADCP velocities are comparable. The phase fluctuates around zero degrees for all depths (Fig. 4.3c and f) so geostrophic and ADCP velocities are in phase.

At KS02 close to Ellesmere Island the vertical velocity profiles already gave an indication for the discrepancy between geostrophic and ADCP velocity. In the frequency domain we see that at frequencies between 0.08 cpd (12.5 days) and 0.3 cpd (3.3 days) 40–50% of the variance between geostrophic and ADCP velocity is explained for velocities at 50 and 100 m depth (Fig. 4.3a). At lowest frequencies— less than 0.05 cpd (20 days)—the coherence squared drops below the 95% confidence level only at 50 m. This emphasized the discrepancy in shallow layers at low frequencies. At 150 m the coherence squared is only above the 95% significance level at frequencies below 0.1 cpd (10 days). The gain between geostrophic velocity and ADCP velocity is between 0.2 and 0.5 for all three depth levels at all frequencies (Fig. 4.3c) meaning that geostrophic velocities are consistently higher than ADCP velocities at this locations as also seen in Fig. 4.2a and c. The phase fluctuates around zero for 50 m, and is positive (between 0 and +40) at all frequencies at 100 m and 150 m (Fig. 4.3b). In deeper layers ADCP velocities therefore lead geostrophic velocities by one day.

4.4 Discussion of Velocity Discrepancy on Ellesmere Island Side due to the Lateral Boundary Condition

Geostrophic and ADCP velocities close to Ellesmere Island indicate that the flow is not geostrophic at that location. We speculate that the large difference on the Ellesmere Island side between the calculated geostrophic and the measured ADCP velocity is related to the lateral boundary layer. KS02 might be close enough to Ellesmere Island to be within the horizontal boundary layer.

4.4.1 Free-Slip versus No-Slip

Geostrophic velocity calculations assume a balance between the pressure gradient and Coriolis force and friction is neglected. Therefore free-slip conditions, assuming no friction on boundaries, leads to high velocities close to the wall. In a channel flow friction occurs in the bottom boundary layer and along the side boundaries.

The ADCP velocity measures both the barotropic and baroclinic part of the velocity. It also includes ageostrophic effects due to vertical and lateral friction. It is influenced by the friction from the nearby wall and resembles a no-slip case where the velocity has to drop to zero at the wall.

Spall et al. (2008) use an idealized numerical model of the shelfbreak jet in the western Arctic to investigate eddy formation and ventilation, and discuss no-slip and free-slip lateral boundary conditions. With no-slip conditions the mean boundary current structure shows a viscous shear layer near the boundary; with free-slip conditions the velocity increases towards the boundary. In the no-slip case, the mean zonal velocity at 115 m (averaged over the final 100 days of integration) decreases toward zero within about two km of the boundary. Geostrophic velocity assumes no friction and resembles free-slip conditions while the measured ADCP velocities resemble the no-slip case. In general the scale of the lateral boundary

layer is a function of rotation, ice/wind stress, bottom friction, lateral friction, and stratification.

In Fig. 4.4 we plot the along-channel depth-averaged geostrophic velocity (crosses) and ADCP velocity (circles) between 30 and 200 m against distance across the strait. Geostrophic velocity has its maximum 3 km from the coast with 0.14 m s^{-1}. It then decreases rapidly to less than 0.10 m s^{-1} 7 km from the coast. We speculate that those high geostrophic velocities close to the wall exist due to free-slip conditions. ADCP velocity 3 km from the coast shows velocities of 0.07 m s^{-1}. No ADCP velocity data exists in the middle of the strait although Münchow and Melling (2008) suggest a velocity maximum there. ADCP velocities close to Greenland are of comparable values than on the Ellesmere Island side. For ADCP data we speculate that velocity goes to zero at the wall due to no-slip.

4.4.2 Vertical Friction Arguments from Valle-Levinson's (2008) Model Runs

Another approach to try to explain the discrepancy in velocity on the Ellesmere Island side analyzes figures from analytical model results from Valle-Levinson (2008) (Fig. 4.5). The model consists of a density-stratified channel with variable bottom depth and uses linear, steady-state momentum balances that includes vertical bottom friction. The model excludes lateral friction completely and only discusses vertical friction at the bottom. It also does not take a seasonal ice cover into account and assumes a non-zero volume flux, which changes the surface boundary condition from no-stress to no-slip when the ice is land-fast. These assumptions need to be kept in mind here but as a first interpretation the model helps us understand the discrepancy between geostrophic and ADCP velocity close to Ellesmere Island.

Model results categorize density-driven exchange flows in terms of two non-dimensional parameters:

120

- Kelvin number K_e: introduced by Garvine (1995), measure of baroclinic pressure gradients, defined as the ratio between the channel width (W, here 40 km) and the internal Rossby radius of deformation ($L_D \sim 10$ km): $K_e = \frac{W}{L_D}$. Nares Strait: $K_e \sim 4$ (Münchow et al., 2006).

- Ekman number E_k: measure of the vertical friction term, defined as the ratio between the vertical boundary layer thickness ($D_E = \sqrt{\frac{A_z}{f}}$ with A_z the vertical viscosity) and the local water depth (H, here 300 m): $E_k = \frac{D_E^2}{H^2}$. Nares Strait: typical Ekman layer scales ~ 30 m, therefore $E_k \sim 0.01$.

Valle-Levinson's (2008) model predictions use different parameter settings with changing E_k and K_e for a given symmetric channel. Concentrating on a topography closest resembling Nares Strait and Kelvin and Ekman numbers that occur in Nares Strait, we focus on two model runs that use $K_e = 4$ with $E_k = 0.0002$ and $E_k = 0.1111$.

Velocities increase continuously towards the coast for the almost inviscid case $E_k = 0.0002$, denoted by the arrow in Fig. 4.5a. This resembles our geostrophic estimates. As discussed earlier the geostrophic velocity resembles an inviscid (free-slip) case.

In contrast, the more viscous case $E_k = 0.1111$ results in a surface jet with largest velocities seaward (Fig. 4.5b). Maximum flows reach 0.14 (non-dimensional flow, normalized by maximum inflow) away from the wall. This case resembles more closely our directly measured ADCP velocities where a no-slip condition at the coast leads to zero velocity at the boundary.

4.5 Summary and Future Work

We here compared geostrophic and ADCP velocities in the time and frequency domain at different depths and locations. The outcome is different for the eastern half of the strait and the location close to the Ellesmere Island coast.

At KS10 in the eastern half of the strait geostrophic and observed velocities are comparable. In the top 100 m, 50–80% of the correlated variance between geostrophic and ADCP velocity is explained at frequencies below 0.1 cpd (10 days) at zero phase at this location.

Geostrophic and ADCP velocities depict a large discrepancy at KS02 close to the Ellesmere coast during all ice seasons. We associate this discrepancy with the lateral boundary layer. Geostrophic velocity resembles free-slip conditions. The velocity increases towards the boundary and assumes no friction. ADCP velocity resembles no-slip conditions with a viscous shear layer and zero velocity at the wall. The CT measurements are close to the Ellesmere coast to possibly be within the horizontal boundary layer. Figures from Valle-Levinson's (2008) model runs demonstrate different vertical friction scenarios by using different Kelvin and Ekman number scenarios relevant for Nares Strait. Evaluating these graphs show that the more viscous case shows maximum velocities away from the wall, and the almost inviscid case shows continuously increasing velocities towards the wall.

In the future this discrepancy needs to be evaluated in more detail. No CT and ADCP measurements exist within 4–5 km of the lateral boundary in Nares Strait from subsequent mooring deployments. More rigorous measurements and comparisons close to the lateral boundary will be required in the future. A model similar to Valle-Levison's but with volume flux, lateral friction, and a changing ice cover might also help to investigate this interesting feature. Also oceanic fields in Nares Strait are not only influenced by the lateral boundary layer but are forced by vertical and horizontal boundary layer physics at the ice-water, air-water, water-land, and ice-air interfaces.

Implications from this analysis are that flows close to lateral boundaries are not in geostrophic balance. ADCP measurements might be required to measure the actual flow field close to boundaries. Geostrophic flow and flux calculations from

CT and CTD measurements close to lateral boundaries are possibly an overestimate. More analysis is needed with regard to this topic and consequences will need to be drawn with respect to future cruise planning and mooring array designs.
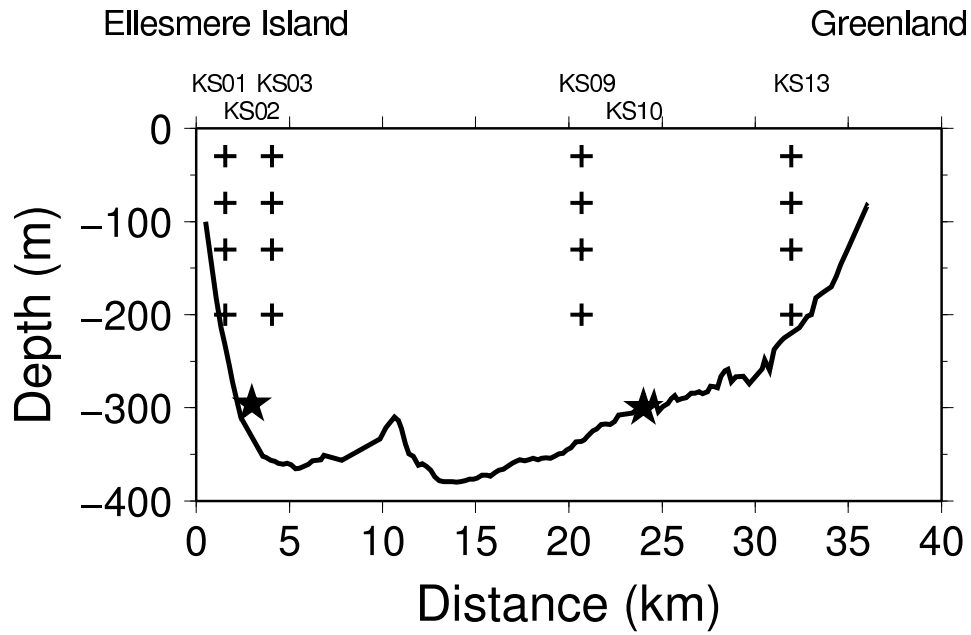
Figure 4.1: Cross-section of Nares Strait showing locations of CT instruments (crosses) and ADCP moorings (stars) used for comparisons. We compare geostrophic velocities calculated between KS01 and KS03 to ADCP data from KS02, and geostrophic velocities calculated between KS09 and KS13 to ADCP data from KS10.
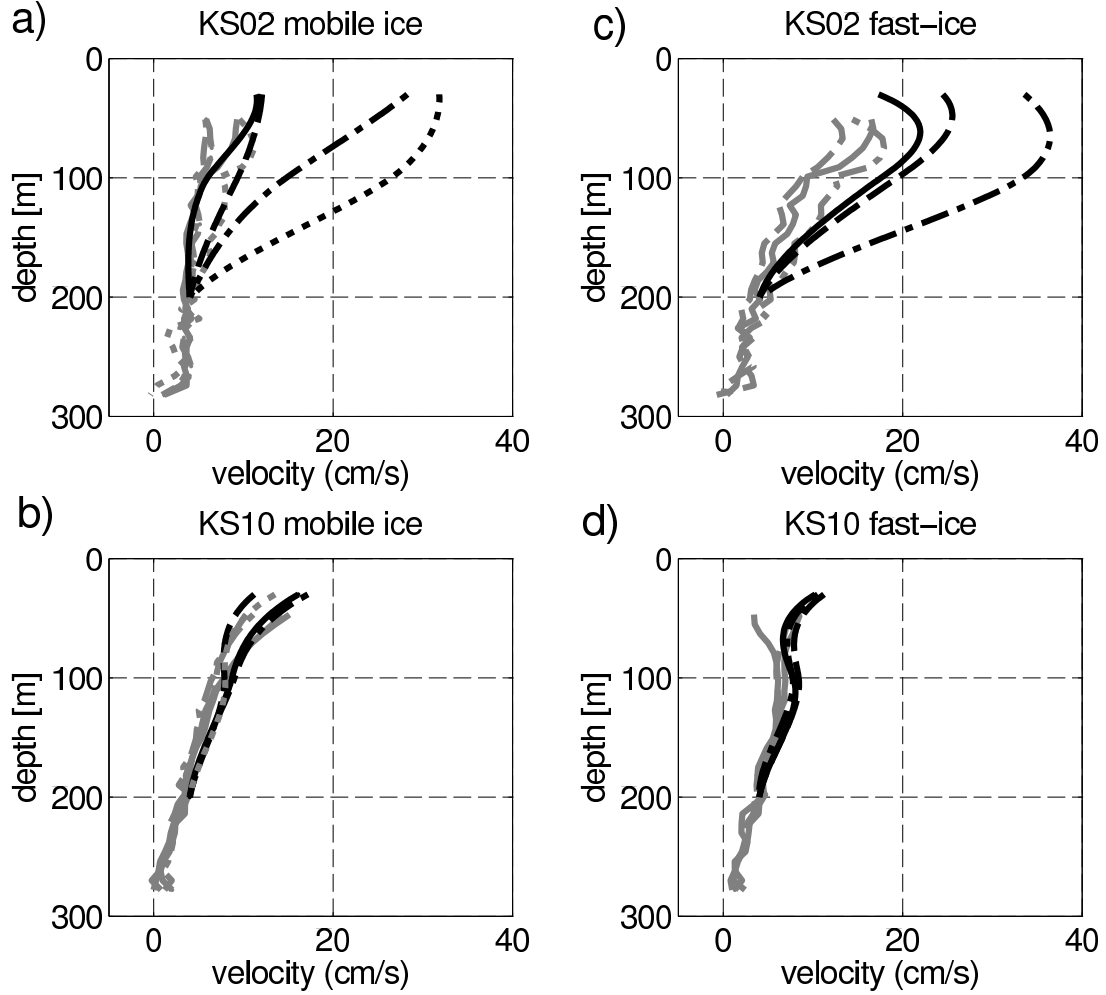
Figure 4.2: Vertical profiles of geostrophic (black) and ADCP (gray) velocity at
KS02 (a and c) and KS10 (b and d). The different line styles denote
different seasonal means: solid = 2003 mobile ice season/ 2003/04 fast-
ice season, dashed = 2004 mobile ice season/ 2004/05 fast-ice season,
dash-dotted = 2005 mobile ice season/ 2005/06 fast-ice season, dotted
= 2006 mobile ice season. a) and b) are mobile ice seasons and c) and
d) fast-ice seasons. Due to ADCP processing problems the ADCP
data only reaches up to 50 m depth and not above.
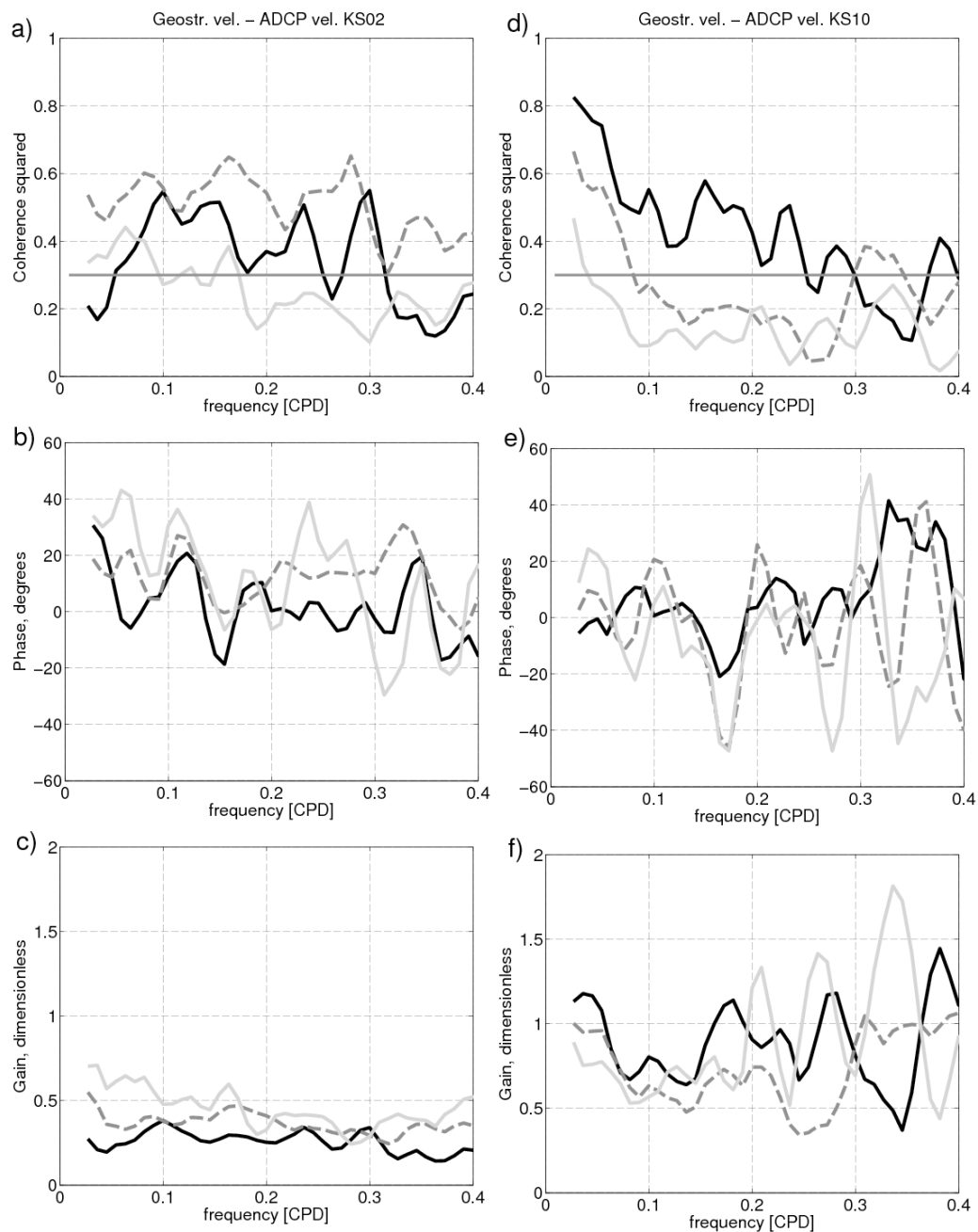
Figure 4.3: Coherence squared (a and d), phase [degrees] (b and e), and gain [dimensionless] (c and f) for KS02 and KS10 between geostrophic and ADCP velocity. Black lines denote 50 m depth, dark gray dashed line 100 m depth, and light gray lines 150 m depth. The dark gray solid line in the coherence squared plots is the 95% confidence level.
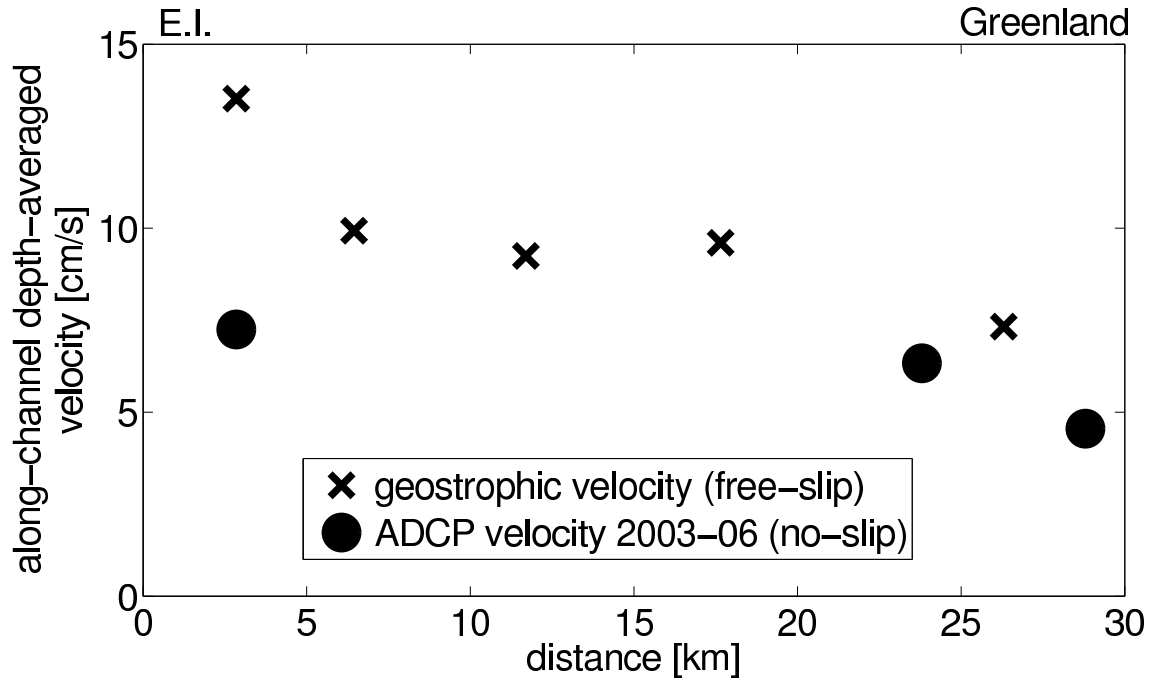
Figure 4.4: Along-channel depth-averaged geostrophic (crosses) and ADCP (circles) velocities between 30 and 200 m between 2003–06. Geostrophic velocity is similar to free-slip conditions leading to increasing geostrophic velocity close to the wall; ADCP velocities resemble no-slip conditions leading to a zero velocity at $x = 0$. Note the discrepancy between geostrophic and ADCP velocities close to Ellesmere Island (E.I.). Geostrophic velocity data points resemble the mean geostrophic velocity between the two neighboring CT mooring locations while ADCP data points were measured at exactly that point.
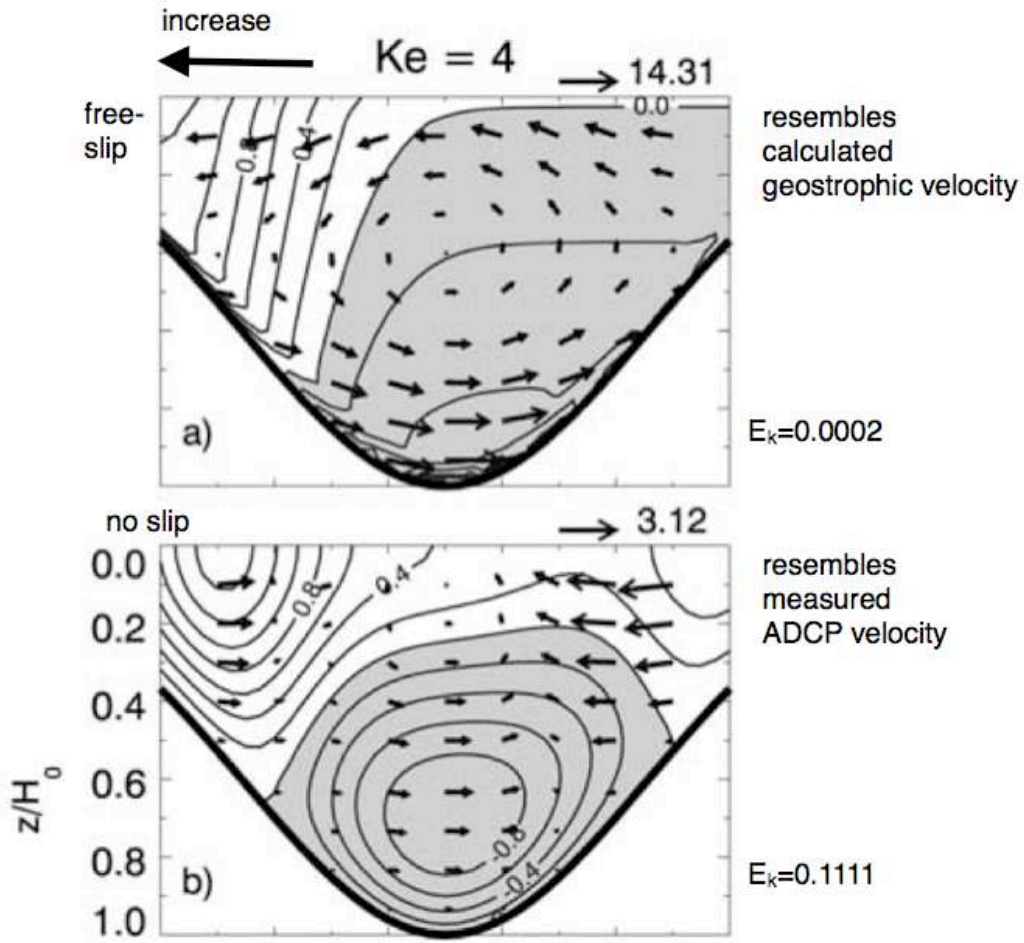
Figure 4.5: Plots of along-strait (normalized by maximum inflow) and cross-strait (scale noted in top right corner in cm s^{-1}) flows in a cross-section from model output (adjusted from Valle-Levinson, 2008). Darker areas denote regions of inflows. Contours are drawn at 0.2 intervals. The view is looking into the strait, in our case with Ellesmere Island on the left and Greenland on the right. Both subplots assume $K_e = 4$ with a) $E_k = 0.0002$, and b) $E_k = 0.1111$. Subplot a) resembles calculated geostrophic velocities more closely and shows velocity increasing towards the western wall comparable to free-slip conditions. Subplot b) resembles measured ADCP velocity comparable to no-slip conditions with maximum flows away from the wall and velocities decreasing towards the wall.

Chapter 5

CONCLUSIONS

5.1   Conclusions

This dissertation analyzes a three-year mooring data set from 2003–06 from Nares Strait in the CAA to the NW of Greenland with a focus on CT data in combination with local wind, along-channel pressure gradients, and ADCP data. These first long-term measurements at high spatial and temporal resolution are important for the evaluation of the Arctic freshwater budget. Recent changes occurred in the Arctic and can only be traced downstream if we establish a baseline for all outflow regions first. This mooring array in Nares Strait helps establishing a baseline.

An innovative mooring design proved to be successful to support CT sensors at shallow depth while minimizing risk from iceberg encounter and ice-cover threat in Nares Strait, one of the main challenges in the strait. The moorings small components and low net buoyancy within the domain of greatest risk above 200-m depth allow it to be drawn down out of harms way when current (and iceberg drift) is fast.

Due to the novel mooring design two different methodologies were developed to analyze the CT data. First, a frequency domain linear system analysis was used to minimize the "noise" arising from the draw-down of sensors. The result was analyzed with regard to hydrography and salinity fields. Second, a multiple linear regression model was developed resulting in a high vertical resolution salinity and temperature data set. This high vertical resolution data set was the bases for geostrophic ocean current and flux analysis.

This research focuses on sub-tidal variations in salinity, geostrophic velocity, and fluxes although ice, ocean, and atmosphere interact on different time scales in Nares Strait. Throughout this work I have categorized the ice conditions into two seasons that vary on an irregular basis: mobile ice in late summer, fall, and early winter, and land-fast ice in late winter, spring, and early summer. The two different ice states influence geostrophic freshwater flux, forcing, geostrophic velocity, and salinity.

The geostrophic freshwater flux (reference salinity of 34.8 psu) reveals larger variability and higher flux numbers by 30% during mobile ice seasons in comparison to fast-ice seasons. The three-year mean geostrophic freshwater flux is 20 ± 3 mSv excluding ice. This describes 58% of the cross-sectional area above 200 m excluding the top 30 m and including a level of known motion at 200 m. The missing top 30 m of the water column are crucial and a first extrapolation leads to an additional 25% in geostrophic freshwater flux. This is still a lower bound since a constant salinity in the top 30 m was assumed even though salinity decreases towards the surface. Our extrapolation suggests that the flux in the top 30 m is negligible during fast-ice winter seasons ($< 5\%$) but substantial during mobile ice summer seasons ($> 40\%$). The large variations on shorter time scales put values from the literature into context. No significant trend over the three years was observed in geostrophic freshwater flux. The implications of the modulated geostrophic freshwater flux by the ice cover could be important for the future. A transition towards a longer mobile ice season would lead to increased freshwater flux. The system would respond more strongly to time-dependent local and remote forcing and enhanced freshwater flux could lead to changes downstream.

In contrast to the freshwater flux, the geostrophic volume flux is not modulated by the ice cover; the three-year mean is 0.47 ± 0.05 Sv with a statistically significant $15\% \pm 4\%$ increase over the three years. Variability is large in geostrophic

volume flux and comparisons to literature values reveal both seasonal weekly bias due to temporally varying ice cover and strong events, respectively.

The geostrophic freshwater and volume flux in Nares Strait are partially forced by along-channel local winds and pressure gradients during the mobile ice season. At weekly time scales the combined variance during the mobile ice seasons from local wind and along-channel pressure gradient forcing explains 80% of the variance. During the fast-ice seasons 40% of the variance is explained at eight days with all variance from the along-channel pressure gradient; local wind has no effect as the flow is decoupled from the atmosphere through the ice cover.

The three-year mean geostrophic current flows southward in the middle and on the western side of the channel. Direct measurements by ADCP near the coast of Greenland during the same time period indicate that current flows northward there (Münchow and Melling, 2008). As a three-year average, the geostrophic flow through the section in Kennedy Channel is southward and surface-intensified with a maximum of 0.20 m s^{-1} on the Ellesmere Island side and a secondary maximum of 0.14 m s^{-1} at the shallowest depth of measurement near the middle of the section, including a reference level velocity from ADCP data.

The seasonal mean interannual variability of geostrophic velocities shows a strengthening core in the middle of the strait and an additional core close to Ellesmere Island during mobile ice conditions. The latter appears in the 2005 mobile ice season. During fast-ice seasons a sub-surface core close to Ellesmere Island exists which increases and condenses over the three years. A transition occurs from a single jet in the center of the channel to an emerging coastal current adjacent to Ellesmere Island over the three-year period.

Geostrophic velocities demonstrate large variability over time and a strong dependence on the ice cover. In the western part of the strait maximum geostrophic

velocities occur during fast-ice seasons (increasing over the three years) with a sub-surface core. The middle of the strait presents maxima in the surface layer during mobile ice seasons. Much smaller geostrophic velocities exist close to Greenland during all ice seasons. During the mobile ice seasons reversing signs in geostrophic flow on short time scales can be observed throughout the strait.

The waters found on opposite sides of Nares Strait have different characteristics. Those on the western side are colder and less saline than those on the eastern side. Isopycnals generally have their maximum slope near the middle of the strait consistent with the enhanced geostrophic velocity here. The freshest, coldest water is found near the sea surface on the Ellesmere Island side, flowing southward from the Arctic Ocean as a buoyant outflow similar to a coastal current (Yankovsky et al., 2000; Bacon et al., 2002; Chapman, 2003; Pickart et al., 2005). Over the three-year survey the greatest temporal variability in salinity was observed within this cold outflow. Salinity demonstrates frequent freshwater incursions during mobile ice seasons and more steady conditions during fast-ice seasons. I identify up- and downwelling events on both sides of the strait. The greatest temporal variability in temperature was observed on the Greenland side. Variability is small at depth where waters are isolated from surface salt and heat fluxes by ice cover and by a statically stable water column.

Temporal variability at scales larger than three years from interannual trends of salinity and geostrophic velocity show a surface layer close to Ellesmere Island that becomes saltier over time and a bottom layer that becomes fresher off Ellesmere Island. Geostrophic velocities increase over the three years of our observations by up to 0.1 m s^{-1} year^{-1} in the top 100 m off Ellesmere Island. This locations not only includes the part of the water column that contains most of the freshwater but it is also on the western side of the strait with the freshest water. The increase in geostrophic velocity is offset by water masses getting saltier at this location over the

three years therefore leading to no increase in geostrophic freshwater flux (trends in the geostrophic freshwater flux are not significant at the 95% confidence level). The sectionally averaged increase in geostrophic velocity from the three-year deployment leads to the statistically significant increase in geostrophic volume flux of $15\% \pm 4\%$ but does not imply long-term change.

An EOF analysis of salinity variations across the section has revealed two modes that together explain 3/4 of the total variance. Mode one (54% of the variance) is surface-intensified and has maximum amplitude at the coast of Ellesmere Island; with negative eigenvalue it represents a south-flowing buoyant boundary current. Mode two (19% of the variance) represents a tendency for surface-intensified northward flow, strongest on the Greenland side, to accompany strong southward flow near 100 m depth on the Ellesmere side, and vice versa. Interplay of these modes can create a seesaw behavior between the Ellesmere and Greenland sides of the strait and between the top and the middle depths close to Ellesmere Island. When the top layer is saltier, the mid-layer on the Ellesmere Island side is fresher and vice versa, resulting in times of small and large vertical stratification.

The first EOF mode of salinity variations appears to be correlated with the state of the ice cover, so that the cross-strait variation in surface salinity is strongest during drifting ice conditions. The annual modulation of the second EOF mode of salinity variations appears better correlated with date than with ice condition; the variation is large and positive at the beginning of January (high surface salinity) and large and negative at the end of August (low surface salinity). In combination, these modes create strong geostrophic current near the ocean surface mid-strait in late summer, and a sub-surface jet of geostrophic current adjacent to Ellesmere in mid-winter, as shown earlier.

One intense anomaly in salinity occurred in July 2005. Salinity at 35-m depth decreased by close to two psu over two days and isohalines shoaled sharply near the

133

middle of the strait. This event can also be seen in the principal component time series of the first EOF mode of salinity with a large, negative amplitude indicating a location near the surface on the Ellesmere side. At the same time a rapid ice export within the Rossby radius of deformation close to Ellesmere Island existed, associated with strong southward winds. The associated geostrophic flow was southward at 0.30 m s^{-1} in the top layers in the middle of the strait.

Geostrophic velocity shows large variability at monthly to interannual time scales while geostrophic freshwater flux shows large variability at weekly time scales. I conclude that traditional ways to present seasonality as monthly means and annual cycles does not describe the variability in Nares Strait well. Seasonality relates to the ice state.

In the eastern part of the strait geostrophic and ADCP velocities compare well during all ice seasons. In the top 100 m 50–80% of the correlated variance between geostrophic and ADCP velocity is explained at frequencies below 0.1 cpd (10 days) at zero phase. In the western part of the strait close to Ellesmere Island the geostrophic and ADCP velocities do not compare well during all ice seasons. This discrepancy I associate with the lateral boundary layer. Geostrophic velocity resembles free-slip conditions, the velocity increases towards the boundary and assumes no friction. ADCP velocity resembles no-slip conditions with a viscous shear layer and zero velocity at the wall. The CT measurements are close enough to Ellesmere Island to be within the horizontal boundary layer. Valle-Levinson's (2008) analytical model runs use different Kelvin and Ekman number scenarios. The more viscous case shows maximum velocities away from the wall, and the almost inviscid case shows continuously increasing velocities towards the wall, which we associate with ADCP and geostrophic velocities, respectively.

The two ice states discussed in this dissertation depend on an ice bridge forming in Smith Sound. This ice bridge failed to form in 2006/07 (Münchow et

al., 2007; Kwok et al., 2010), 2008/09, and 2009/10. These were the first recorded such occurrences possibly indicating a transition to a different dynamic state. As demonstrated in this dissertation, a longer mobile ice season implies larger freshwater fluxes by up to 40%. Furthermore, such change also implies an extended period of thick ice streaming south. In combination such conditions increase total freshwater flux. A potential increase in freshwater flux is caused since the system responds more strongly to time-dependent local atmospheric surface forcing in addition to remote forcing by the ambient Arctic Ocean and Baffin Bay. Changes in the duration of land-fast ice seasons impact vertical and horizontal stratification as well as the distribution, transit time, and pathways of Arctic freshwater. I hypothesize that the dynamics of Nares Strait after August 2006 are in a state of transition as the season of land-fast ice cover diminishes. A continuation of the data set in Nares Strait from 2007–09 (and 2009–11) will test if the freshwater flux through the CAA is indeed transitioning to a dynamic state that is characterized by mobile ice. This regime change to longer mobile ice seasons would cause more variability in ice and ocean motion.

From the analyzed three years of data in Nares Strait I found large variability and dependence on the ice seasons. Salinity, geostrophic velocity, and fluxes are influenced by the ice cover. These first long-term measurements are useful to put historical flux numbers into context. Short-term measurements include a seasonal bias and large covariance on short time scales for geostrophic fluxes emphasized this.

5.2 Future Work

As seen in the previous chapters Nares Strait is a strongly changing environment related to ice conditions, local along-channel wind, and pressure gradients. Future work will further investigate the 2003–06 data set that this dissertation has focused on. An extension of this data set exists from 2007–09 (Fig. 5.1). In addition moorings were deployed again in 2009 for another two-year period (Fig. 5.2).

The mooring array during those two time periods was a little bit further north in Kennedy Channel at 80.5°N with less instrumentation. The 2007–09 data set includes 12 moorings with 11 along a mooring line with complete across-strait coverage with CT strings and ADCPs (Fig. 5.1), and one pressure sensor in Smith Sound. The 2009–11 deployment includes eight moorings with seven along a mooring line (Fig. 5.2), and one pressure sensor in Smith Sound. The extended data set covers the whole cross-section with ADCP and CT instruments in comparison to the 2003–06 data set with missing CT data on the Greenland side and ADCP data in the middle of the strait.

Also during the 2009 cruise weather stations obtaining wind data were maintained at Cape Baird, Pim Island, Cape Isabella, and Hans Island within Nares Strait (location in Fig. 5.3). The observations will complement the atmospheric model; a first comparison can be found in Wilkinson et al. (2009).

Questions for future work that could be answered by the extended data sets could address the following points:

- Is the increasing linear trend in geostrophic volume flux by $15\% \pm 4\%$ continuing after 2006? Can this trend also be traced further downstream into Davis Strait?

- What was the effect of the missing ice bridge in Smith Sound in the winters of 2006/07, 2008/09, and 2009/10? Did the missing ice bridge have an effect on the flow structure in the strait and the number of freshwater incursions as seen during mobile ice conditions between 2003 and 2006? Did the geostrophic freshwater flux increase during those years as hypothesized as no winter (fast-ice) conditions existed? Is there a transition towards a different state in the strait when evaluating 2003–11?

- Is the mean structure and the interannual variability of the seasonal means of the geostrophic velocity changing? Is the trend of a second geostrophic velocity core emerging during mobile ice seasons and an intensified geostrophic velocity core during fast-ice seasons continuing? What would this change mean for future mooring deployments and hydrographic sampling?

- Another focus of the data set can be on the strong freshwater incursions during mobile ice seasons: What are their contributions to the overall freshwater flux? Can these incursions be compared in magnitude to Hudson Strait where freshwater pulses (caused by eddies in Hudson Strait) make up 50% of the mean freshwater transport out of the strait (Sutherland et al., 2010)?

The extended mooring deployment until 2009 and possibly 2011 will lead to a longer-term data set. Estimates of volume, and freshwater fluxes—not only geostrophic—will help evaluate variability over multiple years. In the long-run a closer collaboration with modelers might be desirable. Modeling the Arctic outflow through Nares Strait in the CAA will therefore improve. Also models focussing on the Labrador Sea further downstream evaluating convection and circulation might be able to use these longer-term estimates. In general models with high horizontal resolution are necessary to resolve the 40-km wide Nares Strait.

A simple, high-resolution, regional model could address ocean and sea ice dynamics, forcing mechanisms, and frictional issues related to the lateral boundary layer, the ice cover, and the bottom. Contribution of the top 30 m might be evaluated as well as sensitivity of the fluxes to different conditions like ice cover, baroclinic pressure gradients, etc.

Not only examining liquid freshwater but also ice, MODIS images might be used to track strong ice outflow from the Arctic Ocean in the whole strait and especially within the internal Rossby radius of deformation as seen during the strong event in July 2005. The Ice Profiling Sonars measure ice thickness and their data

results in a valuable data set concerning ice fluxes as well. MODIS images might also be possible to evaluate surface velocities and surface temperatures at times in the future.

In the long-run a combination of Nares Strait flux estimates with flux estimates from other straits in the CAA (Lancaster Sound, Barrow Strait, Cardigan Strait, Hells Gate, Wellington Channel, Hudson Strait) is needed to draw a complete picture of what is happening in the CAA. A comparison to Davis Strait flux estimates downstream would also help understand the complete system. More questions are concerned with where the increase in liquid freshwater flux after 2005 in Davis Strait is originated (de Steur et al., 2010). Eventually a reevaluation of the overall Arctic freshwater budget might be the goal once long-term measurements have been taken along all pathways of all components.

The issue of the lateral boundary layer close to Ellesmere Island mentioned in this dissertation will need to be investigated further. The extended data sets include CT and ADCP instruments covering the same part of the strait. Therefore it will be possible to evaluate if the flow is indeed geostrophic in the middle of the strait. No measurements close to the lateral boundary exist though to further test if friction leads to non-geostrophic conditions close to the side wall.

Future work will also need to investigate and extrapolate data in more detail from 30 m to the sea surface where most of the freshwater flux occurs. The novel CT string design proved successful between 30 and 200 m but as shown above the top 30 m play a crucial role in freshwater flux. Summer CTD measurements from surface to bottom only lead to snapshots. Downwelling events during mobile ice seasons demonstrate the fresh conditions in the top layers that are measured at 30 m. Additional mooring instruments like Ice-Tethered Profilers for example could help determine water properties above 30 m while the strait is ice covered. More innovative methodologies and techniques will need to be developed and tested in

the future to access the top layers in the strait.

In the future some efforts will also be needed to better understand the formation and collapse of ice bridges in Smith Sound (with changing conditions the ice bridge north of Robeson Channel). Since the formation and ice conditions in Nares Strait largely influence the oceanic conditions in the strait a thorough understanding is necessary especially since the implications on the freshwater flux could be severe.

To conclude the data set from 2003–06 and in combination with the subsequent mooring data from 2007–09 and 2009–11 offers a wide range of science questions in Nares Strait. Previous publications and this dissertation only present a first step in the analysis.
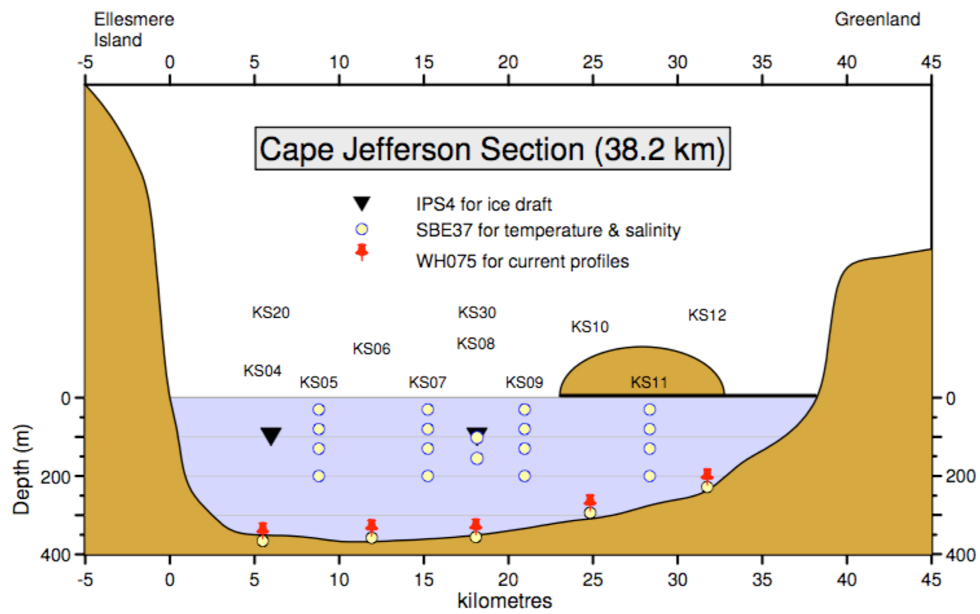
Figure 5.1: Mooring array at Cape Jefferson deployed in 2007 and recovered in 2009 in Kennedy Channel including four CT-strings with four SBE37 instruments each, two Ice Profiling Sonars, one with two SBE37 instruments, and five ADCPs with SBE37s (Melling, 2009).
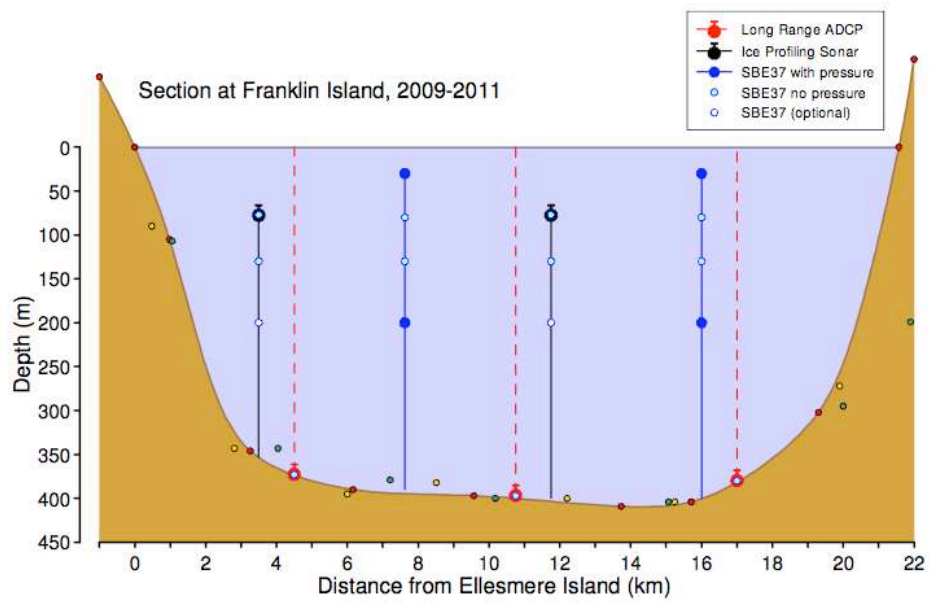
Figure 5.2: Mooring array at Franklin Island deployed in 2009 with a planned recovery date in 2011 in Kennedy Channel including two CT-strings with four SBE37 instruments each, two Ice Profiling Sonars strings with three SBE37s each, and three ADCPs (Melling, 2009).
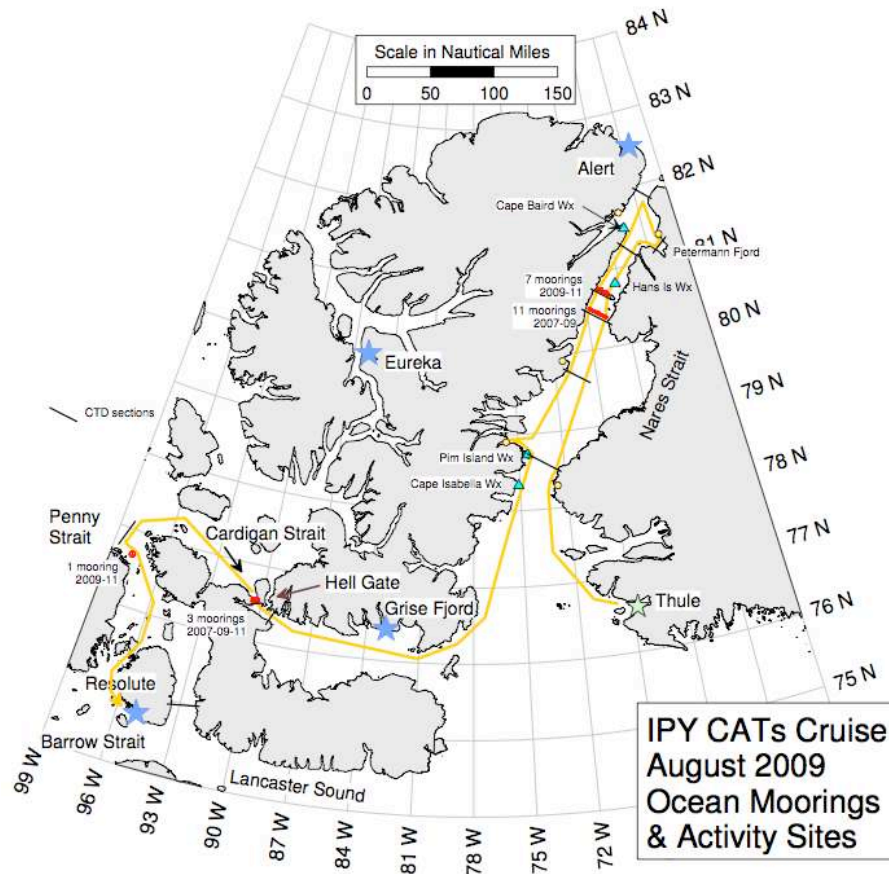
Figure 5.3: CCGS Larsen cruise plan for August 2009 cruise in yellow including location of mooring sections 2007–09 and 2009–11 as red lines, and location of weather stations as blue triangles (Melling, 2009).

REFERENCES

Aagaard, K. and E. C. Carmack, 1989: The role of sea ice and other fresh water in the Arctic circulation. *J. Geophys. Res.*, **94 (C10)**, 14,485–14,498.

Ando, K., T. Matsumoto, T. Nagahama, I. Ueki, Y. Takatsuki, and Y. Kuroda, 2005: Drift characteristics of a moored conductivity-temperature-depth sensor and correction of salinity data. *J. Atmos. Oceanic Technol.*, **22 (3)**, 282–291.

Bacle, J., E. Carmack, and R. Ingram, 2002: Water column structure and circulation under the North Water during spring transition: April-July 1998. *Deep-Sea Res. part II*, **49 (22-23)**, 4907–4925.

Bacon, S., G. Reverdin, I. Rigor, and H. Snaith, 2002: A freshwater jet on the East Greenland Shelf. *J. Geophys. Res.*, **107 (C7)**.

Barber, D., R. Marsden, P. Minnett, G. Ingram, and L. Fortier, 2001: Physical processes within the North Water NOW Polynya. *Atmos.-Oceans*, **39 (3)**, 163–166.

Bell, W., 1979: A three-dimensional subsurface mooring model. Pacific Marine Science Report 79-20, Fisheries and Oceans Canada, Institute of Ocean Sciences, Sidney, Canada.

Bendat, J. and A. Piersol, 1993: *Engineering Applications of Correlations and Spectral Analysis.* John Wiley & Sons, New York, NY, 458 pp.

Bourke, R., V. Addison, and R. Paquette, 1989: Oceanography of Nares Strait and northern Baffin Bay in 1986 with emphasis on deep and bottom water formation. *J. Geophys. Res.*, **94**, 8289–8302.

Candela, J., R. Beardsley, and R. Limeburner, 1992: Separation of tidal and subtidal currents in ship-mounted Acoustic Doppler Current Profiler observations. *J. Geophys. Res.*, **97 (C1)**, 769–788.

Chapman, D., 2003: Separation of an advectively trapped buoyancy current at a bathymetric bend. *J. Phys. Oceanogr.*, **33 (5)**, 1108–1121.

Coachman, L. K. and K. Aagaard, 1966: On water exchange through Bering Strait. *Limnol. Oceanogr.*, **11 (1)**, 44–59.

Copland, L., D. R. Mueller, and L. Weir, 2007: Rapid loss of the Ayles ice shelf, Ellesmere Island, Canada. *Geophys. Res. Let.*, **34 (21)**, L21 501.

Cuny, J., P. B. Rhines, and R. Kwok, 2005: Davis Strait volume, freshwater and heat fluxes. *Deep-Sea Res.*, **52 (3)**, 519–542.

Davis, R., 1976: Predictibility of sea surface temperature and sea level pressure anomalies over the North Pacific Ocean. *J. Phys. Oceanogr.*, **6**, 249–266.

de Steur, L., M. Steele, J. Morison, I. G. Rigor, C.M. Lee, and E. Hansen, 2010: Recent changes in Arctic Ocean freshwater distribution. Submitted to *Geophys. Res. Let.*.

Dickson, R. R., J. Meincke, S. A. Malmberg, and A. J. Lee, 1988: The Great Salinity Anomaly in the northern North-Atlantic 1968-1982. *Progr. Oceanogr.*, **20 (2)**, 103–151.

Dumont, D., Y. Gratton, and T. Arbetter, 2009: Modeling the dynamics of the North Water Polynya ice bridge. *J. Phys. Oceanogr.*, **39 (6)**, 1448–1461.

Dunbar, M., 1973: Ice regime and ice transport in Nares Strait. *Arctic*, **26 (4)**, 282–291.

Fahrbach, E., J. Meincke, S. Østerhus, G. Rohardt, U. Schauer, V. Tverberg, and J. Verduin, 2001: Direct measurements of volume transports through Fram Strait. *Polar Research*, **20 (2)**, 217–224.

Fofonoff, N. and H. Bryden, 1975: Density of sea waters. *J. Mar. Res.*, **41**, 69–82.

Freitag, H., M. McCarty, C. Nosse, R. Lukas, M. McPhadden, and M. Cronin, 1999: COARE Seacat data: Calibrations and quality control procedures. *NOAA Tech. Memo.*, **ERL PMEL-115**, 89 pp.

Garvine, R. W., 1995: A dynamical system for classifying buoyant coastal discharges. *Cont. Shelf Res.*, **15 (13)**, 1585–1596.

Garrett, C. and B. Toulany, 1982: Sea-level variability due to meteorological forcing in the northeast Gulf of St-Lawrence. *J. Geophys. Res.*, **87 (NC3)**, 1968–1978.

Gill, A. E., 1982: *Atmosphere-Ocean Dynamics.* Academic Press, Orlando, FL, 662 pp.

Goosse, H., T. Fichefet, and J. M. Campin, 1997: The effects of the water flow through the Canadian Archipelago in a global ice-ocean model. *Geophys. Res. Let.*, **24 (12)**, 1507–1510.

Harms, S. and C. Winant, 1998: Characteristic patterns of the circulation in the Santa Barbara Channel. *J. Geophys. Res.*, **103 (C2)**, 3041–3065.

Hakkinen, S., 1993: An Arctic source for the Great Salinity Anomaly: A simulation of the Arctic ice-ocean system for 1955-1975. *J. Geophys. Res.*, **98 (C9)**, 16 397–16 410.

Hakkinen, S., 1999: Variability of the simulated meridional heat transport in the North Atlantic for the period 1951-1993. *J. Geophys. Res.*, **104 (C5)**, 10 991–11 007.

Holland, M. M., J. Finnis, A. P. Barrett, and M. C. Serreze, 2007: Projected changes in Arctic Ocean freshwater budgets. *J. Geophys. Res.*, **112 (G4)**, G04S55.

Holliday, N. P., S. L. Hughes, S. Bacon, A. Beszczynska-Moeller, B. Hansen, A. Lavin, H. Loeng, K. A. Mork, S. Osterhus, T. Sherwin, and W. Walczowski, 2008: Reversal of the 1960s to 1990s freshening trend in the northeast North Atlantic and Nordic Seas. *Geophys. Res. Let.*, **35 (3)**.

Jones, E. and A. Eert, 2006: Water of Nares Strait in 2001. *Polarforschung*, **74 (1-3)**, 186–189.

Jones, E., J. Swift, L. Anderson, M. Lipizer, G. Civitarese, K. Falkner, G. Kattner, and F. McLaughlin, 2003: Tracing Pacific water in the North Atlantic Ocean. *J. Geophys. Res.*, **108 (C4)**.

Khan, S. A., J. Wahr, M. Bevis, I. Velicogna, and E. Kendrick, 2010: Spread of ice mass loss into northwest Greenland observed by GRACE and GPS. *Geophys. Res. Let.*, **37**, doi:10.1029/ 2010GL042460.

Kliem, N. and D. A. Greenberg, 2003: Diagnostic simulations of the summer circulation in the Canadian Arctic Archipelago. *Atmos.-Oceans*, **41 (4)**, 273–289.

Koenigk, T., U. Mikolajewicz, H. Haak, and J. Jungclaus, 2007: Arctic freshwater export in the 20th and 21st centuries. *J. Geophys. Res.*, **112 (G4)**, G04S41.

Kundu, P. and J. Allen, 1976: Some three-dimensional characteristics of low-frequency current fluctuations near the Oregon coast. *J. Phys. Oceanogr.*, **6**, 181–199.

Kwok, R., 2005: Variability of Nares Strait ice flux. *Geophys. Res. Let.*, **32 (24)**, L24 502.

Kwok, R., L. T. Pedersen, P. Gudmandsen, and S. Pang, 2010: Large sea ice outflow into the Nares Strait in 2007. *Geophys. Res. Let.*, **37**, doi:10.1029/ 2009GL041872.

Lazier, J., 1980: Oceanographic conditions at Ocean Weather Ship Bravo, 1964-1974. *Atmos.-Ocean*, **18 (3)**, 227–238.

LeBlond, P. H., 1980: On the surface circulation in some channels of the Canadian Arctic Archipelago. *Arctic*, **33 (1)**, 189–197.

Lindsay, R. and J. Zhang, 2005: The thinning of Arctic sea ice, 1988-2003: Have we passed a tipping point? *J. Climate*, **18 (22)**, 4879–4894.

Lindsay, R., J. Zhang, A. Schweiger, M. Steele, and H. Stern, 2009: Arctic sea ice retreat in 2007 follows thinning trend. *J. Climate*, **22 (1)**, 165–176.

Lorenz, E., 1956: Empirical orthogonal functions and statistical weather predictions. Tech. rep., Scientific Report No.1, Statistical Forecasting Project, Dept. of Meteorology, MIT.

Melling, H., 2000: Exchanges of freshwater through the shallow straits of the North American Arctic. *The Freshwater Budget of the Arctic Ocean*, **In: Lewis, E.L., Jones, E.P., Lemke, P., Prowse, T.D., Wadhams, P. (Eds.)**, Springer, 479–502.

Melling, H., 2004: Fluxes through the northern Canadian Arctic Archipelago. *ASOF Newsletter*, **2**, 3–7.

Melling, H., T. A. Agnew, K. K. Falkner D. A. Greenberg, C. M. Lee, A. Münchow, B. Petri, S. J. Prinsenberg, R. M. Samelson, and R. A. Woodgate, 2008: Fresh-water fluxes via Pacific and Arctic outflows across the Canadian polar shelf. *Arctic-Subarctic Ocean Fluxes*, **R. R. Dickson, J. Meincke and P. Rhines (Eds.)**, Springer, 193–261.

Melling, H., 2009: Science Plan Larsen Cruise 2009. *Larsen Cruise Report*, 1–32.

Melling, H., Y. Gratton, and G. Ingram, 2001: Ocean circulation within the North Water polynya of Baffin Bay. *Atmos.-Oceans*, **39 (3)**, 301–325.

Mosby, H., 1962: Water, salt and heat balance of the north Polar Sea and of the Norwegian Sea. *Geophys. Norv.*, **24**, 289–313.

Münchow, A., 1998: Tidal currents in a topographically complex channel. *Cont. Shelf Res.*, **18 (5)**, 561–584.

Münchow, A. and R. Chant, 2000: Kinematics of inner shelf motions during the summer stratified season off New Jersey. *J. Phys. Oceanogr.*, **30 (2)**, 247–268.

Münchow, A., K. Falkner, and H. Melling, 2007: Spatial continuity of measured seawater and tracer fluxes through Nares Strait, a dynamically wide channel bordering the Canadian Archipelago. *J. Mar. Res.*, **65 (6)**, 759–788.

Münchow, A., A. Masse, and R. Garvine, 1992: Astronomical and nonlinear tidal currents in a coupled estuary shelf system. *Cont. Shelf Res.*, **12 (4)**, 471–498.

Münchow, A. and H. Melling, 2008: Ocean current observations from Nares Strait to the west of Greenland: Interannual to tidal variability and forcing. *J. Mar. Res.*, **66 (6)**, 801–833.

Münchow, A., H. Melling, and K. K. Falkner, 2006: An observational estimate of volume and freshwater flux leaving the Arctic Ocean through Nares Strait. *J. Phys. Oceanogr.*, **36 (11)**, 2025–2041.

Padman, L. and S. Erofeeva, 2004: A barotropic inverse tidal model for the Arctic Ocean. *Geophys. Res. Let.*, **31 (2)**, L02 303.

Parkinson, C. L. and D. J. Cavalieri, 2008: Arctic sea ice variability and trends, 1979-2006. *J. Geophys. Res.*, **113 (C7)**, C07 003.

Peterson, B., R. Holmes, J. McClelland, C. Vorosmarty, R. Lammers, A. Shiklomanov, I. Shiklomanov, and S. Rahmstorf, 2002: Increasing river discharge to the Arctic Ocean. *Science*, **298 (5601)**, 2171–2173.

Pickart, R., 2004: Shelfbreak circulation in the Alaskan Beaufort Sea: Mean structure and variability. *J. Geophys. Res.*, **109 (C4)**.

Pickart, R., D. Torres, and P. Fratantoni, 2005: The East Greenland Spill Jet. *J. Phys. Oceanogr.*, **35 (6)**, 1037–1053.

Polyakov, I. and M. Johnson, 2000: Arctic decadal and interdecadal variability. *Geophys. Res. Let.*, **27 (24)**, 4097–4100.

Prinsenberg, S. and E. Bennett, 1987: Mixing and transports in Barrow Strait, the central part of the Northwest Passage. *Cont. Shelf Res.*, **7 (8)**, 913–935.

Prinsenberg, S. J. and E. B. Bennett, 1989: Vertical variations of tidal currents in shallow land fast ice-covered regions. *J. Phys. Oceanogr.*, **19 (9)**, 1268–1278.

Prinsenberg, S. J. and J. Hamilton, 2005: Monitoring the volume, freshwater and heat fluxes passing through Lancaster Sound in the Canadian Arctic Archipelago. *Atmos.-Oceans*, **43 (1)**, 1–22.

Proshutinsky, A., R. Krishfield, M.-L. Timmermans, J. Toole, E. Carmack, F. McLaughlin, W. J. Williams, S. Zimmermann, M. Itoh, and K. Shimada, 2009: Beaufort Gyre freshwater reservoir: State and variability from observations. *J. Geophys. Res.*, **114**, doi:10.1029/ 2008JC005104.

Rabe, B., A. Münchow, H. Johnson, and H. Melling, 2010: Nares Strait Hydrography and Salinity Field from a Three-Year Moored Array. *J. Geophys. Res.*, in press., doi:10.1029/ 2009JC005966.

Rennermalm, A., E. Wood, S. Dery, A. Weaver, and M. Eby, 2006: Sensitivity of the thermohaline circulation to Arctic Ocean runoff. *Geophys. Res. Let.*, **33 (12)**.

Rignot, E. and K. Steffen, 2008: Channelized bottom melting and stability of floating ice shelves. *Geophys. Res. Let.*, **35 (2)**, L02 503.

Rigor, I., J. Wallace, and R. Colony, 2002: Response of sea ice to the Arctic Oscillation. *J. Climate*, **15 (18)**, 2648–2663.

Rudels, B., E. Jones, U. Schauer, and P. Eriksson, 2004: Atlantic sources of the Arctic Ocean surface and halocline waters. *Polar Research*, **23 (2)**, 181–208.

Sadler, H., 1976: Water, heat, and salt transport through Nares Strait, Ellesmere Island. *J. Fish. Res. Board Can.*, **33**, 2286–2295.

Samelson, R. M., T. Agnew, H. Melling, and A. Münchow, 2006: Evidence for atmospheric control of sea-ice motion through Nares Strait. *Geophys. Res. Let.*, **33 (2)**, L02 506.

Samelson, R. and P. Barbour, 2008: Low-level winds in Nares Strait: a model-based mesoscale climatology. *Mon. Weather Rev.*, **136**, 4746–4759.

Schauer, U., E. Fahrbach, S. Østerhus, and G. Rohardt, 2004: Arctic warming through the Fram Strait: Oceanic heat transport from 3 years of measurements. *J. Geophys. Res.*, **109 (C6)**.

Schauer, U., H. Loeng, B. Rudels, V. K. Ozhigin, and W. Dieck, 2002: Atlantic Water flow through the Barents and Kara Seas. *Deep-Sea Res.*, **49 (12)**, 2281–2298.

Serreze, M. C. and J. A. Francis, 2006: The Arctic amplification debate. *Clim. Change*, **76 (3-4)**, 241–264.

Serreze, M. C., A. P. Barrett, A. G. Slater, R. A. Woodgate, K. Aagaard, R. B. Lammers, M. Steele, R. Moritz, M. Meredith, and C. M. Lee, 2006: The large-scale freshwater cycle of the Arctic. *J. Geophys. Res.*, **111 (C11)**, C11 010.

Spall, M., R. Pickart, P. Fratantoni, and A. Plueddemann, 2008: Western Arctic shelfbreak eddies: Formation and transport. *J. Phys. Oceanogr.*, **38 (8)**, 1644–1668.

Steele, M., D. Thomas, D. Rothrock, and S. Martin, 1996: A simple model study of the Arctic Ocean freshwater balance, 1979-1985. *J. Geophys. Res.*, **101 (C9)**, 20 833–20 848.

Stouffer, R. J., J. Yin, J. M. Gregory, K. W. Dixon, M. J. Spelman, W. Hurlin, A. J. Weaver, M. Eby, G. M. Flato, H. Hasumi, A. Hu, J. H. Jungclaus, I. V. Kamenkovich, A. Levermann, M. Montoya, S. Murakami, S. Nawrath, A. Oka, W. R. Peltier, D. Y. Robitaille, A. Sokolov, G. Vettoretti, and

S. L. Weber, 2006: Investigating the causes of the response of the Thermohaline Circulation to past and future climate changes. *J. Climate*, **19 (8)**, 1365–1387.

Straneo, F. and F. Saucier, 2008: The outflow from Hudson Strait and its contribution to the Labrador Current. *Deep-Sea Res. part I*, **55 (8)**, 926–946.

Stroeve, J., M. Serreze, F. Fetterer, T. Arbetter, W. Meier, J. Maslanik, and K. Knowles, 2005: Tracking the Arctic's shrinking ice cover: Another extreme September minimum in 2004. *Geophys. Res. Let.*, **32 (4)**.

Sutherland, D. A. and R. S. Pickart, 2008: The East Greenland Coastal Current: structure, variability, and forcing. *Progr. Oceanogr.*, **78 (1)**, 58–77.

Sutherland, D. A., F. Straneo, S.J. Lentz, and P. St-Laurent, 2010: Observations of fresh, anticyclonic eddies in the Hudson Strait outflow. Submitted to *J. Marine Sys.*

Tang, C. L., Q. Gui, and B. M. DeTracey, 1999: A modeling study of upper ocean winter processes in the Labrador Sea. *J. Geophys. Res.*, **104 (C10)**, 23 411–23 425.

Timofeev, V., 1960: Water Masses of the Arctic Basin (in Russian. *Gydrometeoizdat*, Leningrad, Russia.

UNESCO, 1983: Algorithms for computation of fundamental properties of seawater. *UNESCO Tech. Pap. Mar. Sci.*, **44**, 58.

Valle-Levinson, A., 2008: Density-driven exchange flow in terms of the Kelvin and Ekman numbers. *J. Geophys. Res.*, **113 (C5)**, doi:10.1029/ 2008JC004853.

Wadley, M. R. and G. R. Bigg, 2002: Impact of flow through the Canadian Archipelago and Bering Strait on the North Atlantic and Arctic circulation: An ocean modelling study. *Quart. J. R. Met. Soc.*, **128 (585)**, 2187–2203.

White, D., L. Hinzman, L. Alessa, J. Cassano, M. Chambers, K. Falkner, J. Francis, W. J. Gutowski, M. Holland, R. M. Holmes, H. Huntington, D. Kane, A. Kliskey, C. Lee, J. McClelland, B. Peterson, T. S. Rupp, F. Straneo, M. Steele, R. Woodgate, D. Yang, K. Yoshikawa, and T. Zhang, 2007: The Arctic freshwater system: Changes and impacts. *J. Geophys. Res.*, **112 (G4)**, G04S54.

Wilkinson, J. P., P. Gudmandsen, S. Hanson, R. Saldo, and R. M. Samelson, 2009: Hans Island: meteorological data from an international borderline. *EOS Trans. Amer. Geophys. Union*, **90**, 190-191.

Woodgate, R. A. and K. Aagaard, 2005: Revising the Bering Strait freshwater flux into the Arctic Ocean. *Geophys. Res. Let.*, **32 (2)**, L02 602.

Wu, P., H. Haak, R. Wood, J. Jungclaus, and T. Furevik, 2008: Simulating the terms in the Arctic hydrological budget. *Arctic-Subarctic Ocean Fluxes*, **R. R. Dickson, J. Meincke and P. Rhines (Eds.)**, Springer, 363–384.

Yankovsky, A. E., R. W. Garvine, and A. Münchow, 2000: Mesoscale currents on the inner New Jersey shelf driven by the interaction of buoyancy and wind forcing. *J. Phys. Oceanogr.*, **30 (9)**, 2214–2230.